THE UNIVERSITY OF CHICAGO

DESIGN, CONTROL, AND CHARACTERIZATION OF SOLUTION-PROCESSED SEMICONDUCTORS FOR OPTOELECTRONIC APPLICATIONS

A DISSERTATION SUBMITTED TO

THE FACULTY OF THE DIVISION OF THE PHYSICAL SCIENCES

IN CANDIDACY FOR THE DEGREE OF

DOCTOR OF PHILOSOPHY

DEPARTMENT OF CHEMISTRY

BY

MARGARET HERVEY HUDSON

CHICAGO, ILLINOIS

DECEMBER 2019

Table of Contents

List of Figures v

List of Tables x

Acknowledgements xi

Abstract xiv

1. Introduction to solution-processed inorganic semiconductors. 1

1.1. Solution-processed semiconductors. 1

1.2. Molecular semiconductor precursors. 2

1.3. Solution synthesis of colloidal nanocrystals. 3

1.4. Quantum dots overview. 5

1.5. Quantum dots for photodetection. 7

1.6. Quantum dots for visible light emission. 9

1.7. Thesis motivation. 10

1.8. Chapter 1 bibliography. 11

2. Synthesis and structural characterization of $A_2Cd_2Se_3$ (A: Na^+, NEt_4^+, or DDA^+) and its use as a composition-matched ligand for colloidal nanocrystals 17

2.1. Introduction to chalcogenidometallates. 17

2.2. $Na_2Cd_2Se_3$ synthesis and crystal structure. 19

2.3. Extension of selenocadmate stability to non-hydrazine solvents. 22

2.4. EXAFS analysis of the solution structure of $Na_2Cd_2Se_3$ and $(NEt_4)_2Cd_2Se_3$ 24

2.5. Molecular selenocadmates as capping ligands for colloidal nanocrystals. 28

2.6. Conclusions. 31

2.7. Materials and methods. 32

2.8. Chapter 2 bibliography. 36

3. New forms of CdSe and CdTe: mesostructures and gels 41

3.1. Introduction to mesostructured semiconductors and chalcogels. 41

3.2. Templated synthesis of mesostructured II-VI semiconductors. 43

3.3. Synthesis and characterization of gel-like stoichiometric $CdSe \cdot xN_2H_4$ 48

3.4. Applications of polycrystalline CdSe films prepared from CdSe gel. 57

3.5. Conclusions. 62

3.6. Materials and methods. 63

3.7. Chapter 3 bibliography. 70

4. Spectroscopic evidence of conduction band fine structure in colloidal HgTe quantum dots with well-defined intraband transitions 73

4.1. Introduction to HgTe QDs and QD doping. 73

4.2. HgTe QD synthesis and characterization. 75

4.3. Optical characterization of electron-doped HgTe QDs: appearance of multiple intraband transitions. 83

4.4. Trends in the excitonic and intraband absorbance peak energies for HgTe QDs. 86

4.5. HgTe QD spectroelectrochemistry. 90

4.6. Tight binding calculations for HgTe QDs. 93

4.7. Conclusions. 95

4.8. Materials and methods. 96

4.9. Chapter 4 bibliography. 101

5. Progress in the molten salt synthesis of $In_{1-x}Ga_xP$ quantum dots. 106

5.1. Introduction to InP QDs and molten salt chemistry. 106

5.2. Ligand exchange and molten salt dispersal of InP QDs..... 108

5.3. Impact of the InP QD surface chemistry during 400 °C molten salt annealing. 114

5.4. Impact of the InP QD surface chemistry on indium-to-gallium cation exchange: composition and structure. 121

5.5. Impact of the InP QD surface chemistry on indium-to-gallium cation exchange: optical properties. 130

5.6. Effects of time and temperature on indium-to-gallium cation exchange. 136

5.7. Extension of cation exchange methods to large InP QDs with different morphologies. 147

5.8. Conclusions. 151

5.9. Materials and methods. 152

5.10. Chapter 5 bibliography. 159

List of Figures

Figure 1.1. Deposition versatility of solution processing. 2

Figure 1.2. Illustration of a hot injection synthesis of CdSe nanocrystals. 4

Figure 1.3. Classes of inorganic ligands for colloidal nanocrystals. 5

Figure 1.4. Illustration of quantum confinement. 6

Figure 1.5. Effect of size on quantum dot absorbance. 7

Figure 2.1. $Na_4Cd_4Se_6 \cdot 9.5\ N_2H_4$ crystal structure. 20

Figure 2.2. Asymmetric unit of the $Na_4Cd_4Se_6 \cdot 9.5\ N_2H_4$ crystal structure. 20

Figure 2.3. Schematic for $[Cd_2Se_3]_n^{2n-}$ cation exchange. 23

Figure 2.4. UV-vis spectra of cation-exchanged $[Cd_2Se_3]_n^{2n-}$ 23

Figure 2.5. Raw EXAFS data for selenocadmate solutions. 24

Figure 2.6. R-space plots for selenocadmate EXAFS data. 25

Figure 2.7. Fits to selenocadmate EXAFS data at the Cd K-edge. 26

Figure 2.8. Fits to selenocadmate EXAFS data at the Se K-edge 26

Figure 2.9. EXAFS comparison of selenocadmate and $(CdSe)_{13}$ clusters. 28

Figure 2.10. Characterization of selenocadmate-capped CdSe nanoparticles. 30

Figure 3.1. Schematic for the synthesis of mesostructured II-VI materials. 43

Figure 3.2. Structural characterization of mesostructured CdSe. 44

Figure 3.3. Powder XRD patterns for mesostructured CdSe before and after mild annealing. 46

Figure 3.4. Raman spectra for mesostructured CdSe and $Na_2Cd_2Se_3$ 46

Figure 3.5. TGA data for mesostructured CdSe. 47

Figure 3.6. Optical characterization of mesostructured CdSe. 47

Figure 3.7. Characterization of mesostructured CdTe. 48

Figure 3.8. CdSe gel synthesis. 49
Figure 3.9. Raman spectrum of CdSe gel. 50
Figure 3.10. Time evolution of CdSe gel XRD pattern. 51
Figure 3.11. Description of CdSe gel formation and evolution with time. 53
Figure 3.12. Characterization of dried CdSe gel. 54
Figure 3.13. EXAFS data for CdSe gel. 54
Figure 3.14. Fits to EXAFS data for CdSe gel. 55
Figure 3.15. Characterization of annealed CdSe gel. 57
Figure 3.16. Photoconductivity of annealed CdSe gel. 58
Figure 3.17. Fabrication of an FET device with CdSe gel. 59
Figure 3.18. FET characteristics for a CdSe gel film annealed at 250 °C. 60
Figure 3.19. FET characteristics for a CdSe gel film annealed at 350 °C. 60
Figure 3.20. FET characteristics for annealed films of $(N_2H_5)_2Cd_2Se_3$. 61
Figure 4.1. HgTe QD absorbance spectra and TEM images. 76
Figure 4.2. HgTe QD XRD pattern. 77
Figure 4.3. Chemical control of HgTe QD doping. 78
Figure 4.4. Raw HgTe QD absorbance spectra. 79
Figure 4.5. Absorbance spectra for intrinsic HgTe QDs. 79
Figure 4.6. Characterization of large HgTe QDs. 80
Figure 4.7. Excitonic peak trends for intrinsic HgTe QDs. 81
Figure 4.8. SAXS data and fits for colloidal solutions of HgTe QDs. 82
Figure 4.9. HgTe QD superlattices. 83
Figure 4.10. Characterization of optical absorbance for n-doped HgTe QDs. 84

Figure 4.11. Intraband peak trends for n-doped HgTe QDs. 85
Figure 4.12. HgTe QD sizing curve for excitonic and intraband transitions. 87
Figure 4.13. Spectroelectrochemistry diagram for HgTe QDs. 90
Figure 4.14. HgTe QD spectroelectrochemistry results..... 91
Figure 4.15. HgTe QD spectroelectrochemistry analysis. 93
Figure 4.16. HgTe QD cyclic voltammetry. 93
Figure 4.17. Results of HgTe QD tight binding calculations. 94
Figure 4.18. High resolution TEM images of HgTe QDs..... 95
Figure 4.19. Role of HgTe QD polydispersity in intraband peak splitting. 96
Figure 5.1. Stabilization mechanisms for QDs in various media. 109
Figure 5.2. Absorbance spectra for ligand-exchanged InP QDs. 111
Figure 5.3. Photographs of InP QDs dispersed in molten bromide eutectic. 112
Figure 5.4. Absorbance spectra for InP QDs recovered after 300 °C molten salt (MS) anneal. 114
Figure 5.5. XRD patterns for InP QDs before and after 300 °C MS anneal. 114
Figure 5.6. Comparison of InP QD absorbance after MS annealing at 300 and 400 °C. 116
Figure 5.7. Powder XRD patterns for InP QDs after 400 °C MS anneal. 117
Figure 5.8. Illustration of the improved temperature stability of chalcogenide-capped InP QDs. 119
Figure 5.9. Comparison of the temperature stability of $(NH_4)_2S$ and Li_2S passivated InP QDs. 120
Figure 5.10. Overview of indium-to-gallium cation exchange. 121
Figure 5.11. $In_{1-x}Ga_xP$ characterization for QDs with different initial surface passivation. 123
Figure 5.12. Comparison of XRD patterns for InP QDs with different surface passivations after various MS treatments. 124

Figure 5.13. TEM images of small InP and $In_{1-x}Ga_xP$ QDs. 125

Figure 5.14. Small-angle x-ray scattering (SAXS) data for small InP QDs. 125

Figure 5.15. SAXS data for $In_{1-x}Ga_xP$ QDs with different surface passivations. 126

Figure 5.16. Comparison of the $In_{1-x}Ga_xP$ QD compositions estimated by XRD and elemental analysis. 128

Figure 5.17. Raw photoluminescence (PL) data for small InP QDs and $In_{1-x}Ga_xP$ QDs with different surface passivation. 131

Figure 5.18. $In_{1-x}Ga_xP$ QD PL improves with HF treatment. 131

Figure 5.19. Optical characterization of $In_{1-x}Ga_xP$ QDs treated with mild HF 132

Figure 5.20. Optical characterization of $In_{1-x}Ga_xP$ QDs following harsh HF treatment 133

Figure 5.21. Photoluminescence excitation (PLE) spectra for $In_{1-x}Ga_xP$ QDs with different surface passivation. 134

Figure 5.22. Comparison of absorbance and emission for chalcogenide and metal halide passivated $In_{1-x}Ga_xP$ QDs. 135

Figure 5.23. Steps of indium-to-gallium cation exchange. 137

Figure 5.24. Progression of the band gap change with cation exchange reaction time. 139

Figure 5.25. Optical characterization of small $In_{1-x}Ga_xP$ QDs under different reaction conditions. 140

Figure 5.26. PLE spectra for small $In_{1-x}Ga_xP$ QDs under different reaction conditions. 140

Figure 5.27. SAXS data and corresponding size distributions for $In_{1-x}Ga_xP$ QDs following 380 °C cation exchange. 142

Figure 5.28. SAXS data and corresponding size distributions for $In_{1-x}Ga_xP$ QDs following 400 °C cation exchange. 143

Figure 5.29. Time and temperature dependence of $In_{1-x}Ga_xP$ QD composition. 144

Figure 5.30. Time dependence of cation exchange for large InP QDs. 146

Figure 5.31. Time dependence of cation exchange for small InP QDs in an iodide molten salt. 146

Figure 5.32. TEM images of as-synthesized large InP QDs. 148

Figure 5.33. Characterization of large InP QDs before and after cation exchange. 149

Figure 5.34. Effects of cation exchange on particle shape. 150

Figure 5.35. TEM images of tetrahedral $In_{1-x}Ga_xP$ QDs from two syntheses. 151

List of Tables

Table 1.1. Common colloidal quantum dot materials. 7

Table 1.2. II-VI and III-V QD emitter performance. 10

Table 2.1. Crystal data and structure refinement for $Na_4Cd_4Se_6 \cdot 9.5N_2H_4$ 21

Table 2.2. EXAFS fitting parameters for bulk CdSe and selenocadmate. 27

Table 3.1. EXAFS fitting parameters for bulk CdSe and CdSe gel. 56

Table 4.1. HgTe QD sizing curve equations. 89

Table 4.2. Comparison of experimental and calculated peak broadening for HgTe QDs. 89

Table 5.1. Elemental chalcogen content of InP QDs after MS anneal. 119

Table 5.2. $In_{1-x}Ga_xP$ QD diameters for samples with different surface passivations. 127

Table 5.3. Elemental analysis for $In_{1-x}Ga_xP$ QDs with different surface passivations. 128

Table 5.4. XRD peak analysis for InP and $In_{1-x}Ga_xP$ QDs with different surface passivations. 130

Table 5.5. Elemental analysis of the chalcogen content for $In_{1-x}Ga_xP$ QDs. 136

Table 5.6. Sizes of small $In_{1-x}Ga_xP$ QDs prepared under different reaction conditions. 141

Acknowledgements

I have greatly benefitted from the advice and support of countless individuals during my graduate work. I would like to thank my research advisor Prof. Dmitri Talapin for his guidance during my graduate studies. His insight into what research directions we should pursue and advice for troubleshooting problems were invaluable. I also learned much from Dmitri about how to organize a research project and how to construct manuscripts to tell an engaging story. I would also like to thank my committee members Prof. Philippe Guyot-Sionnest and Prof. Bozhi Tian. Thank you both for reviewing my thesis and offering helpful comments and also for your advice at various points during my graduate career.

I was honored to collaborate with several excellent scientists during my graduate work. I would like to thank Menglu Chen and Prof. Christophe Deleure for their help and insight during our HgTe collaboration. I am very grateful for Dr. Chengjun Sun's assistance with EXAFS measurements at Argonne and his openness to work with us on several projects.

Within our department at the University of Chicago, I have been privileged to work in state-of-the-art facilities managed by wonderfully helpful scientists. I am grateful to Dr. Alex Filatov for his help with several different x-ray techniques. He was always very willing to discuss a problem in detail and work together to form a reasonable hypothesis. I would like to thank Dr. Justin Jureller for training me on several instruments in the MRSEC and helping me troubleshoot problems with the measurements. I am grateful to Dr. Qiti Guo for training me on the SEM and Prof. Jotham Austin for training me on the TEM. Additionally, I would like to thank Yimei Chen for her assistance with TEM measurements.

I was very fortunate to work with amazing colleagues in the Talapin lab. I really enjoyed mentoring two undergraduate students, Stephanie Diaz and Eleanor Dunietz, and talking with them about research, careers, and TV shows. Thank you to Aritrajit Gupta, Josh Portner, Vlad Kamysbayev, Dr. Vishwas Srivastava, Dr. Patrick Cunningham, and Dr. Eric Janke for your great friendship. I will miss our coffee walks and conversations about life and research. I learned so much from various mentors in the lab; I would like to thank Dr. Dmitriy Dolzhnikov, Dr. Mike Boles, Dr. Matt Kurley, Prof. Hao Zhang, and Dr. Igor Fedin for their advice and patience. I would also like to thank everyone in the Talapin lab for their helpful conversations and assistance in lab: Haoqi Wu, Dr. Yuanyuan Wang, Nivedina Sarma, Jia-Ahn Pan, Prof. Jong-Soo Lee, Huicheng Hu, Alex Hinkle, Thomas Habte, Dr. Igor Coropceanu, Wooje Cho, Dr. Himchan Cho, Prof. Xinzheng Lan, Kavan Mulloy, Dr. Abhijit Hazarika, Jake Russell, Dr. Danny Haubold, Prof. Jianwei Nai, Dr. Chunxing She, Prof. Tae Kyu An, Hannah Muir, Dr. João Batista Souza, Jr., Prof. Jaeyoung Jang, and Leo Amaral. I will miss our informal conversations in lab, our yearly soccer rivalry with the He group, and our group outings. Finally, I would like to thank Tanya Shpigel for all that she does to make our lives easier.

In addition to research, I had the opportunity to pursue teaching opportunities during my graduate career. I very much enjoyed serving as an organic chemistry teaching assistant during my first year under the guidance of Dr. Valerie Keller and later collaborating with Val to create curriculum materials for CLOC. I am very thankful to Dr. Britni Ratliff for working around my schedule to help me find opportunities to grow as an educator during my time at UChicago; Britni was a great friend and teaching mentor.

I am certain that my success in graduate school would not have been possible without the abundant love and support of my family and friends. I am incredibly grateful to my parents,

James and Lorri, and my sisters, Mary Joe and Annie Kate, for supporting me and encouraging me to do my best. My family has always been just a phone call away and ready to help me with any problem that comes up or celebrate with me when things are going well. I am also thankful to my brothers-in-law, Jared and Philip, for their encouragement during graduate school. My biggest supporters are my nieces and nephew, Azalea Jayne, Annie Elise, and Hudson, whose love and general fascination with the world offer me great encouragement and inspiration.

Finally, I am so grateful for the amazing friends I have made at the University of Chicago. I have had so much fun hanging out, cooking, and exploring Chicago with you all! Thank you for listening to my complaints and lending your help over the past five years.

Abstract

The deposition of functional semiconducting materials from solution and processing under mild conditions can lower manufacturing costs and expand device versatility. In this document, we examine three classes of solution-processable inorganic semiconductors to gain a better understanding of these materials and plan a route for their optimization. Chapters 2 and 3 focus on the characterization and applications of chalcogenidocadmates, soluble precursors for II-VI semiconductors. Single crystal x-ray diffraction and extended x-ray absorption fine structure (EXAFS) measurements allow us to elucidate the molecular structure of $Na_2Cd_2Se_3$ in its solid state and in hydrazine solution. We explore cation exchange of this species to expand its solubility from hydrazine to more benign solvents and use the cation exchanged selenocadmate to stabilize CdSe nanocrystals in NMF. In Chapter 3, we modify the chalcogenidocadmate structure through interaction with micelle-forming organic cations to create templated mesostructures of CdSe and CdTe. We also show that the reaction of selenocadmate with Cd^{2+} creates a stoichiometric CdSe gel which can be annealed under mild conditions to form photoconductors or field effect transistors.

In the final chapters of the document, we shift our focus away from molecular semiconductor precursors and instead explore colloidal semiconductor nanocrystals, or quantum dots (QDs). HgTe QDs have tunable absorbance across the infrared and can be used as the active layer in mid-infrared photodetectors. In Chapter 4, we use precise synthesis, chemical control of ensemble doping, optical characterization, and electrochemical studies to show that the intraband absorbance of electron-doped HgTe QDs has three peaks, which correspond to transitions between the $1S_e$ state and three nondegenerate P_e states.

In Chapter 5, we study several parameters in the molten salt synthesis of $In_{1-x}Ga_xP$ QDs. The emission energy of these QDs can be tuned by both QD size and alloy composition. We show that the QD surface chemistry can be designed to improve the QD phase stability at elevated temperature. Additionally, we explore a variety of reaction conditions to show that indium-to-gallium cation exchange is diffusion controlled and is accompanied by surface recrystallization. These insights will be useful in designing cation exchange conditions to achieve a desired alloy composition.

1. Introduction to solution-processed inorganic semiconductors.

1.1. Solution-processed semiconductors.

Electronic devices with semiconducting active layers are ubiquitous in modern technology. Transistors, photodetectors, solid state lighting, photovoltaics, and many other technologies rely on the manufacture and manipulation of high quality semiconducting layers. The majority of these semiconducting layers are manufactured through single crystal growth from a melt, which requires very high purity materials and elevated processing temperatures, or vapor deposition techniques, which require high vacuum.[1] The development of solution-based semiconductor inks is of interest for lower cost and higher versatility deposition of semiconducting layers.

Soluble semiconductor precursors can be deposited onto a substrate and processed under mild conditions to yield a functional semiconductor film. These semiconductor inks are typically deposited under ambient conditions, reducing costs when compared with high temperature or vacuum techniques.[2] Moreover, soluble precursors can be deposited using a variety of high-throughput processes, including spin coating, spray coating, inkjet printing, dip coating, slot-die coating, and doctor blading (Figure 1.1).[3] These deposition techniques can be used to uniformly cover large area substrates and some (*e.g.* spray coating and dip coating) can be extended to irregular substrate morphologies. Much effort has been devoted to the exploration of organic semiconductors as solution-processable semiconductor inks, but the development of convenient inks for a variety of inorganic semiconductors should extend the range of achievable electronic performance (*e.g.* carrier mobility) and bandgap.[2-3] Several classes of soluble inorganic semiconductors and semiconductor precursors have been developed in recent years, including lead halide perovskites,[4] chalcogenidometallates,[5-6] and colloidal nanocrystals.[7] Devices made

with these semiconductor inks have shown remarkable performance as transistors,[8] photovoltaics,[4, 9] light emitting diodes,[10] and photodetectors.[11-12]

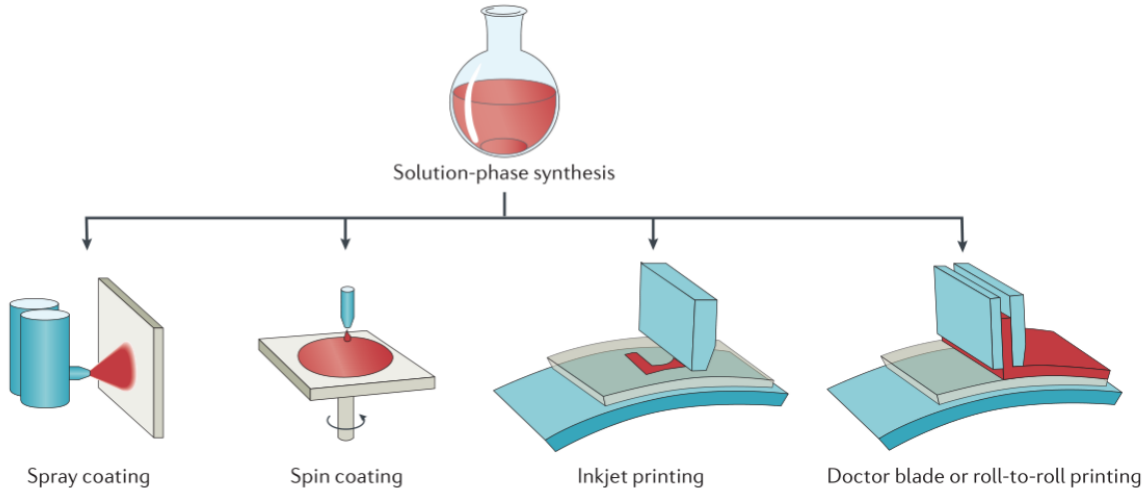

Figure 1.1. Deposition versatility of solution processing.
Schematic demonstrating the variety of techniques that can be used for the deposition of solution-processed semiconductor inks, including spray coating, spin coating, inkjet printing, and doctor blading. Reproduced with permission from García de Arquer *et. al.*, copyright Springer Nature 2017.[3]

1.2. Molecular semiconductor precursors.

Syntheses have been developed for solutions of molecular metal chalcogenide precursors that decompose upon heating to form semiconducting films. These molecular precursors are produced by reacting a metal chalcogenide and excess chalcogen with hydrazine to form a soluble hydrazinium chalcogenidometallate complex. This procedure has produced chalcogenidometallate precursors for tin ($(N_2H_5)_4Sn_2S_6$, $(N_2H_5)_4Sn_2Se_6$), germanium ($(N_2H_5)_4Ge_2S_6$, $(N_2H_5)_4Ge_2Se_6$), indium ($(N_2H_5)_2In_2Se_4$), copper ($N_4H_9Cu_7S_4$), and other metal chalcogenide semiconductors.[13-14] Annealing at 300-350 °C initiates the decomposition of the chalcogenidometallate to form a crystalline metal chalcogenide film, and the residual hydrazine and chalcogenide leave as gaseous byproducts. These precursors have been used to fabricate

$SnSe_{2-x}S_x$ thin film transistors with electron mobilities greater than 10 $cm^2V^{-1}s^{-1}$ and $Cu_{1-y}In_{1-x}Ga_xSe_{2-z}S_z$ solar cells with 12% power conversion efficiency.[5, 13]

A synthetic method was recently developed for the preparation of soluble precursors for cadmium, lead, and bismuth chalcogenides.[8, 15] These bulk chalcogenides do not dissolve in the presence of excess chalcogen in hydrazine, but they react in the presence of alkali chalcogenide salts to form hydrazine-soluble chalcogenidometallates, $Na_2Cd_2Se_3$, Na_2CdTe_2, K_2PbTe_2, and $Na_4Bi_2Te_5$, among others. These chalcogenidometallates decompose below 500 °C to form a crystalline metal chalcogenide semiconducting phase. When combined with nano- or microcrystallites of the metal chalcogenide phase and annealed, these chalcogenidometallates serve as a composition-matched semiconductor solder which binds the crystallites into a robust film with remarkable electronic properties.

1.3. Solution synthesis of colloidal nanocrystals.

The achievable compositions of solution-processable inks for functional materials can be greatly expanded by using colloidal nanocrystals. These nanocrystals are synthesized from reactive precursors under conditions which lead to the nucleation and growth of small crystallites (Figure 1.2). A coordinating surfactant serves to control the crystallite size and provide colloidal stabilization in nonpolar solvents through steric repulsion. Synthetic methods have been developed which yield high quality semiconducting,[16] metallic,[17] and insulating[18] nanocrystals with precise control over their shape and size. Such synthetic advances have enabled the construction of devices where all functional layers are composed of solution-deposited nanocrystals.[19]

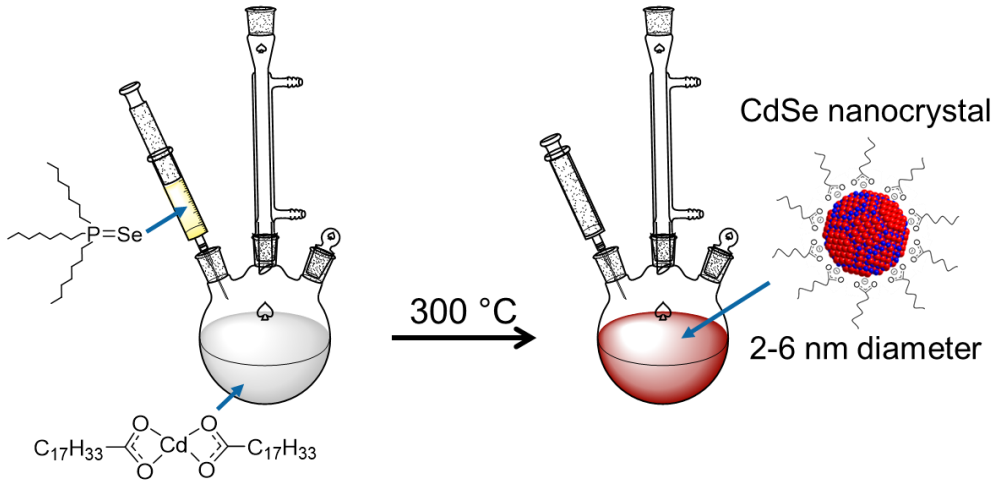

Figure 1.2. Illustration of a hot injection synthesis of CdSe nanocrystals.
Injection of trioctylphosphine selenide into a solution of cadmium oleate at elevated temperatures induces the nucleation and growth of CdSe nanocrystallites passivated by oleate surface ligands.

As synthesized, colloidal nanocrystals are passivated by long-chain organic ligands which provide stabilization in nonpolar solvents. When deposited as a film, the organic ligands surround the nanocrystals with an electrically insulating layer and prevent close contact between nanocrystal cores. Orders-of-magnitude improvements in the electronic performance of a nanocrystal film can be achieved by replacing the insulating native ligands with small inorganic ligands.[20] Solution-phase ligand exchange methods have been developed for the passivation of colloidal nanocrystals with chalcogenides,[21] chalcogenidometallates,[20] halides,[22] pseudohalides, halometallates,[23] and polyoxometallates[24] as well as the preparation of bare nanocrystal surfaces[25] (Figure 1.3). These inorganic-capped nanocrystals are stabilized in polar solvent through electrostatic repulsion and can be deposited from solution to create a film. The strong coupling between inorganic-capped nanocrystals in thin films has led to the realization of high performance solution-processed field effect transistors[26] and photovoltaics.[27]

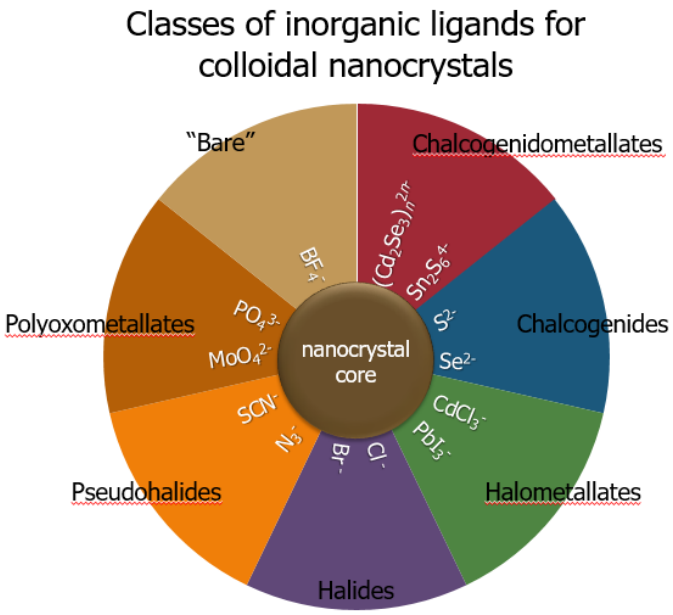

Figure 1.3. Classes of inorganic ligands for colloidal nanocrystals.
The organic ligands on as-synthesized colloidal nanocrystals can be exchanged for a variety of small inorganic ligands that provide colloidal stabilization in polar solvents through electrostatic repulsion.

1.4. Quantum dots overview.

In addition to their ease of solution processing, colloidal semiconductor nanocrystals exhibit different optical and electronic properties than their bulk counterparts.[28] A semiconductor crystallite with dimensions smaller than its Bohr exciton radius experiences quantum confinement, resulting in quantization of its electronic states. The energy difference between these states is size dependent; decreasing the nanocrystallite size, and thus increasing the quantum confinement, increases the energy spacing between the states in the conduction and valence bands (Figure 1.4). Depending on the nanocrystallite morphology, the exciton can experience quantum confinement in one, two, or three dimensions. Isotropic semiconductor nanocrystals with diameters of a few to tens of nanometers confine the exciton in three dimensions and are known as quantum dots.

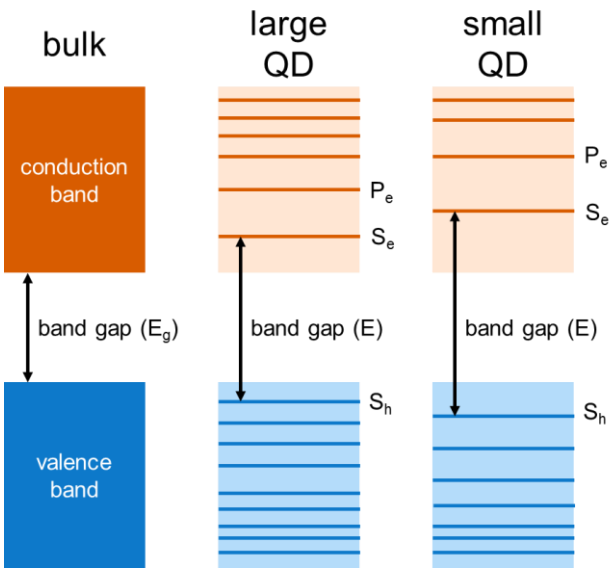

Figure 1.4. Illustration of quantum confinement.
Decreasing the crystallite size increases the band gap of quantum confined semiconductors.

Quantum dots (QDs) exhibit tunable absorption and emission which depend on the material composition and QD size. Materials specific properties, including the bulk bandgap (E_g) and the effective masses of electrons (m_e) and holes (m_h), for a given semiconductor in combination with the nanocrystallite size (R) dictate the energy of the QD band gap (E) based on the Brus equation:[29]

$$E = E_g + \frac{\hbar^2 \pi^2}{2R^2}\left(\frac{1}{m_e} + \frac{1}{m_h}\right) - \frac{1.8e^2}{\epsilon R}$$

We can observe this change in bandgap as a function of crystallite size for a size series of InP QDs (Figure 1.5). As the QD diameter increases from 3.5 nm to 6 nm, the absorbance edge shifts to lower energy (redder). Syntheses have been developed for a wide variety of colloidal QD compositions with precise control over nanocrystallite size and size distribution, creating QD ensembles with absorbance and emission tunable across the UV, visible, and infrared.[16, 30-34] A selection of common QD materials and their spectral range is given in Table 1.1.

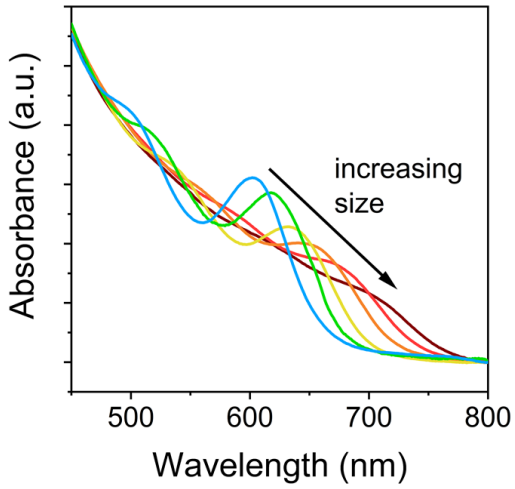

Figure 1.5. Effect of size on quantum dot absorbance.
Absorbance spectra for a size series of InP QDs. As the QD size increases, quantum confinement is relaxed and the bandgap shifts to lower energy.

Table 1.1. Common colloidal quantum dot materials.
List of the semiconductor family and spectral range for common colloidal QD compositions.

Material	Semiconductor family	Spectral range
CdSe	II-VI	visible
CdTe	II-VI	visible
ZnSe	II-VI	UV-visible
PbS	IV-VI	near-IR/SWIR
PbSe	IV-VI	near-IR/SWIR
InP	III-V	visible
InAs	III-V	near-IR

1.5. Quantum dots for photodetection.

Colloidal quantum dots can be used as high performance, tunable active layers in photodetectors. Typical photodetectors use crystalline semiconductors (silicon, InGaAs, HgCdTe) prepared through bulk crystal growth or epitaxial techniques and have a broadband photoresponse.[35] The use of QD active layers both reduces the photodetector cost by relying on

ambient solution processing for semiconductor deposition and also introduces spectral tunability of the photoresponse based on the QD size. Moreover, QD inks can be directly deposited onto read-out integrated circuitry, producing high resolution photodetectors with good fidelity.[3]

Photodetectors with QD active layers can be optimized by tuning the QD composition and size, surface passivation, electronic doping, and device structure. Depending on the composition and crystallite size, QD films can be prepared which respond to visible (CdSe[36]), near- and short-wave infrared (PbS,[37] PbSe[38]), or mid-wave infrared (HgSe,[39] HgTe[40]) radiation. The interaction between QDs in this film is mediated by the QD surface, which is typically passivated by inorganic or short-chain organic ligands to facilitate electronic coupling of the QDs. The QD surface passivation can also be designed to tune the electronic properties of the active layer, such as electronic doping and band alignment.[41] In a photoconductor device structure, the surface chemistry is chosen to minimize electronic doping and thus minimize the dark current, while in a photovoltaic device structure, surface chemistry may be used to design p- and n-type layers of the same QD with different surface passivation.

The use of HgTe QDs for short-wave and mid-wave infrared photodetectors has shown significant progress in recent years.[40, 42] By changing the nanocrystallite size, the HgTe QD absorbance can be tuned throughout the infrared spectrum due to the semimetallic character of bulk HgTe. Through optimization of the QD synthesis, surface treatment, doping strategies, and device architecture, mid-wave infrared photovoltaic devices with a HgTe QD active layer have been designed which exhibit background-limited performance.[12, 43] Further device engineering has enabled improved absorbance through coupling to plasmonic structures[44] and multispectral imaging with layers of different sizes of QDs.[45] Additional improvements may be achieved

through synthetic modifications to minimize the QD size distribution and through improved control over the electronic doping of QD layers.

1.6. Quantum dots for visible light emission.

Many types of colloidal QDs exhibit bright, tunable emission and have been explored for applications as luminescent biolabels,[46] down-converting phosphors,[47] and lasing media,[48] among others. Much research has recently been devoted to the optimization of red, green, and blue QD emitters for display applications.[47, 49] Ideal emitters for display applications have high photoluminescence (PL) quantum yield to optimize the efficiency, narrow emission linewidth and precise spectral tunability to maximize the achievable color gamut, and stable luminescence under harsh conditions to improve device longevity. Synthetic methods to improve these properties of colloidal QDs are widely explored. Improvements in the PL quantum yield of colloidal QD ensembles are largely focused on methods to shell the QD cores with wide band gap semiconductors.[28] The formation of a type-I heterostructure confines the electrons and holes within the core, separating the charge carriers from surface states which could quench the emission. Synthetic methods for the growth of highly emissive QD heterostructures involve growing successive layers of shelling materials[50-51] or shell structures with a graded alloy composition[52-53] to modulate the band alignment and lattice mismatch between the core and shell materials. Additionally, well-developed colloidal QD syntheses allow precise control over the QD size with very low polydispersity, thus achieving narrow emission at a desired wavelength.[54]

Two classes of QDs have been heavily optimized for applications as phosphors in electronic displays, CdSe and InP. As shown in Table 1.1, state-of-the-art CdSe QDs have achieved higher quantum yields and sharper emission linewidths than InP QDs. However,

concerns about heavy metals in consumer electronics have encouraged display manufacturers to prioritize the optimization of InP QD emitters.[55] The poorer performance of InP QD ensembles can be attributed to a variety of factors including the more covalent lattice, which complicates the synthesis of monodisperse, defect-free particles;[56] the rapid oxidation of P^{3-} under synthetic conditions;[57] and the lack of wide band bap III-V shelling methods.[58] The development of methods which expand the synthetic parameter space and allow access to higher temperatures and new synthetic precursors in an oxygen-free environment may provide a way to overcome these challenges for InP QD emitters.

Table 1.2. II-VI and III-V QD emitter performance.
Emission quantum yield (QY) and full-width at half maximum (FWHM) for well-developed syntheses of CdSe and InP QD emitters.

	CdSe QDs	InP QDs
Typical QY	80%	40-60%
Best QY	~100%[59]	90%[51, 60]
Typical FWHM	25-35 nm 100 meV	40-50 nm 150-200 meV
Best FWHM	~20 nm 55-70 meV[54, 59]	36 nm[50-51, 60] 120-130 meV

1.7. Thesis motivation.

In this thesis, I detail the synthesis, structure, and properties of three classes of solution-processable semiconductors and seek to interpret these results for the optimized design of optoelectronic materials. Sodium selenocadmate has been previously used as a composition-matched solder for CdSe nanocrystals. Here, I show that this structure crystallizes as a one-dimensional polyanion of $[Cd_2Se_3]_n^{2n-}$ charge-balanced by sodium. By replacing sodium with

several different inorganic and organic cations, I extend the solubility of selenocadmate to a variety of solvents and show that selenocadmate can interact with cations to form new functional materials, including mesostructured CdSe and CdSe gel. In the next section of the thesis, I explore HgTe QDs which are of interest for their size-dependent electronic doping and their use as the active layer in infrared photodetectors. Through careful synthesis of monodisperse populations of many sizes of HgTe QDs and analysis of their absorbance spectra and spectroelectrochemical response, I show that electron-doped HgTe demonstrates three peaks in its intraband absorbance which correspond to transitions from the $1S_e$ state to three nondegenerate P_e states. This improved understanding of HgTe electronic structure points to the roles of spin-orbit coupling and particle morphology in the optoelectronic properties of HgTe QDs. In the final section of the thesis, I explore the molten salt synthesis of $In_{1-x}Ga_xP$ QDs, which have visible emission that can be tuned by both QD size and alloy composition. Through variations in the molten salt indium-to-gallium cation exchange reaction conditions, I show that the QD surface passivation plays a role in the high temperature phase stability and suggest that the cation exchange is limited by the slow diffusion of gallium into the bulk of the nanocrystallite. These results may be used to design an ideal surface chemistry and alloy composition to achieve high performance $In_{1-x}Ga_xP$ QD emitters.

1.8. Chapter 1 bibliography.

1. Pech-Canul, M. I.; Ravindra, N., *Semiconductors - Synthesis, Properties, and Applications*. 2018.

2. Mitzi, D. B., Solution-processed inorganic semiconductors. *J. Mater. Chem.* **2004,** *14*, 2355-2365.

3. García de Arquer, F. P.; Armin, A.; Meredith, P.; Sargent, E. H., Solution-processed semiconductors for next-generation photodetectors. *Nat Rev Mater* **2017,** *2*, 16100.

4. Zhao, Y.; Zhu, K., Organic–inorganic hybrid lead halide perovskites for optoelectronic and electronic applications. *Chem. Soc. Rev.* **2016,** *45*, 655-689.

5. Mitzi, D. B.; Kosbar, L. L.; Murray, C. E.; Copel, M.; Afzali, A., High-mobility ultrathin semiconducting films prepared by spin coating. *Nature* **2004,** *428*, 299-303.

6. Mitzi, D. B.; Yuan, M.; Liu, W.; Kellock, A. J.; Chey, S. J.; Deline, V.; Schrott, A. G., A High-Efficiency Solution-Deposited Thin-Film Photovoltaic Device. *Adv. Mater.* **2008,** *20*, 3657.

7. Kagan, C. R.; Lifshitz, E.; Sargent, E. H.; Talapin, D. V., Building devices from colloidal quantum dots. *Science* **2016,** *353*, 5523.

8. Dolzhnikov, D. S.; Zhang, H.; Jang, J.; Son, J. S.; Panthani, M. G.; Shibata, T.; Chattopadhyay, S.; Talapin, D. V., Composition-matched molecular "solders" for semiconductors. *Science* **2015,** *347*, 425-428.

9. McDonald, S. A.; Konstantatos, G.; Zhang, S.; Cyr, P. W.; Klem, E. J. D.; Levina, L.; Sargent, E. H., Solution-processed PbS quantum dot infrared photodetectors and photovoltaics. *Nat. Mater.* **2005,** *4*, 138.

10. Shirasaki, Y.; Supran, G. J.; Bawendi, M. G.; Bulović, V., Emergence of colloidal quantum-dot light-emitting technologies. *Nat. Photonics* **2012,** *7*, 13.

11. Zhang, M.; Zhang, F.; Wang, Y.; Zhu, L.; Hu, Y.; Lou, Z.; Hou, Y.; Teng, F., High-Performance Photodiode-Type Photodetectors Based on Polycrystalline Formamidinium Lead Iodide Perovskite Thin Films. *Scientific Reports* **2018,** *8*, 11157.

12. Ackerman, M. M.; Tang, X.; Guyot-Sionnest, P., Fast and Sensitive Colloidal Quantum Dot Mid-Wave Infrared Photodetectors. *ACS Nano* **2018,** *12*, 7264-7271.

13. Mitzi, D. B., Solution Processing of Chalcogenide Semiconductors via Dimensional Reduction. *Adv. Mater.* **2009,** *21*, 3141-3158.

14. Mitzi, D. B., N4H9Cu7S4: A Hydrazinium-Based Salt with a Layered Cu7S4-Framework. *Inorg. Chem.* **2007,** *46*, 926-931.

15. Zhang, H.; Son, J. S.; Dolzhnikov, D. S.; Filatov, A. S.; Hazarika, A.; Wang, Y.; Hudson, M. H.; Sun, C.-J.; Chattopadhyay, S.; Talapin, D. V., Soluble Lead and Bismuth Chalcogenidometallates: Versatile Solders for Thermoelectric Materials. *Chem. Mater.* **2017,** *29*, 6396-6404.

16. Yang, Y. A.; Wu, H.; Williams, K. R.; Cao, Y. C., Synthesis of CdSe and CdTe Nanocrystals without Precursor Injection. *Angew. Chem., Int. Ed.* **2005,** *44*, 6712-6715.

17. Hiramatsu, H.; Osterloh, F. E., A Simple Large-Scale Synthesis of Nearly Monodisperse Gold and Silver Nanoparticles with Adjustable Sizes and with Exchangeable Surfactants. *Chem. Mater.* **2004,** *16*, 2509-2511.

18. Joo, J.; Yu, T.; Kim, Y. W.; Park, H. M.; Wu, F.; Zhang, J. Z.; Hyeon, T., Multigram Scale Synthesis and Characterization of Monodisperse Tetragonal Zirconia Nanocrystals. *J. Am. Chem. Soc.* **2003,** *125*, 6553-6557.

19. Choi, J.-H.; Wang, H.; Oh, S. J.; Paik, T.; Sung, P.; Sung, J.; Ye, X.; Zhao, T.; Diroll, B. T.; Murray, C. B.; Kagan, C. R., Exploiting the colloidal nanocrystal library to construct electronic devices. *Science* **2016,** *352*, 205.

20. Kovalenko, M. V.; Scheele, M.; Talapin, D. V., Colloidal Nanocrystals with Molecular Metal Chalcogenide Surface Ligands. *Science* **2009,** *324*, 1417-1420.

21. Nag, A.; Kovalenko, M. V.; Lee, J.-S.; Liu, W.; Spokoyny, B.; Talapin, D. V., Metal-free Inorganic Ligands for Colloidal Nanocrystals: S2–, HS–, Se2–, HSe–, Te2–, HTe–, TeS32–, OH–, and NH2– as Surface Ligands. *J. Am. Chem. Soc.* **2011,** *133*, 10612-10620.

22. Zhang, H.; Jang, J.; Liu, W.; Talapin, D. V., Colloidal Nanocrystals with Inorganic Halide, Pseudohalide, and Halometallate Ligands. *ACS Nano* **2014,** *8*, 7359-7369.

23. Dirin, D. N.; Dreyfuss, S.; Bodnarchuk, M. I.; Nedelcu, G.; Papagiorgis, P.; Itskos, G.; Kovalenko, M. V., Lead Halide Perovskites and Other Metal Halide Complexes As Inorganic Capping Ligands for Colloidal Nanocrystals. *J. Am. Chem. Soc.* **2014,** *136*, 6550-6553.

24. Huang, J.; Liu, W.; Dolzhnikov, D. S.; Protesescu, L.; Kovalenko, M. V.; Koo, B.; Chattopadhyay, S.; Shenchenko, E. V.; Talapin, D. V., Surface Functionalization of Semiconductor and Oxide Nanocrystals with Small Inorganic Oxoanions (PO43–, MoO42–) and Polyoxometalate Ligands. *ACS Nano* **2014,** *8*, 9388-9402.

25. Rosen, E. L.; Buonsanti, R.; Llordes, A.; Sawvel, A. M.; Milliron, D. J.; Helms, B. A., Exceptionally Mild Reactive Stripping of Native Ligands from Nanocrystal Surfaces by Using Meerwein's Salt. *Angew. Chem., Int. Ed.* **2012,** *51*, 684-689.

26. Choi, J. H.; Fafarman, A. T.; Oh, S. J.; Ko, D. K.; Kim, D. K.; Diroll, B. T.; Muramoto, S.; Gillen, J. G.; Murray, C. B.; Kagan, C. R., Bandlike Transport in Strongly Coupled and Doped Quantum Dot Solids: A Route to High-Performance Thin-Film Electronics. *Nano Letters* **2012,** *12*, 2631-2638.

27. Jo, J. W.; Kim, Y.; Choi, J.; de Arquer, F. P. G.; Walters, G.; Sun, B.; Ouellette, O.; Kim, J.; Proppe, A. H.; Quintero-Bermudez, R.; Fan, J.; Xu, J.; Tan, C. S.; Voznyy, O.; Sargent, E. H., Enhanced Open-Circuit Voltage in Colloidal Quantum Dot Photovoltaics via Reactivity-Controlled Solution-Phase Ligand Exchange. *Adv. Mater.* **2017,** *29*, 1703627.

28. Pietryga, J. M.; Park, Y.-S.; Lim, J.; Fidler, A. F.; Bae, W. K.; Brovelli, S.; Klimov, V. I., Spectroscopic and Device Aspects of Nanocrystal Quantum Dots. *Chem. Rev.* **2016,** *116*, 10513-10622.

29. Brus, L., Electronic wave functions in semiconductor clusters: experiment and theory. *J. Phys. Chem.* **1986,** *90*, 2555-2560.

30. Chen, H.-S.; Lo, B.; Hwang, J.-Y.; Chang, G.-Y.; Chen, C.-M.; Tasi, S.-J.; Wang, S.-J. J., Colloidal ZnSe, ZnSe/ZnS, and ZnSe/ZnSeS Quantum Dots Synthesized from ZnO. *J. Phys. Chem. B* **2004,** *108*, 17119-17123.

31. Hines, M. A.; Scholes, G. D., Colloidal PbS Nanocrystals with Size-Tunable Near-Infrared Emission: Observation of Post-Synthesis Self-Narrowing of the Particle Size Distribution. *Adv. Mater.* **2003,** *15*, 1844-1849.

32. Micic, O. I.; Curtis, C. J.; Jones, K. M.; Sprague, J. R.; Nozik, A. J., Synthesis and Characterization of InP Quantum Dots. *J. Phys. Chem.* **1994,** *98*, 4966-4969.

33. Guzelian, A. A.; Banin, U.; Kadavanich, A. V.; Peng, X.; Alivisatos, A. P., Colloidal chemical synthesis and characterization of InAs nanocrystal quantum dots. *Appl. Phys. Lett.* **1996,** *69*, 1432-1434.

34. Houtepen, A. J.; Koole, R.; Vanmaekelbergh, D.; Meeldijk, J.; Hickey, S. G., The Hidden Role of Acetate in the PbSe Nanocrystal Synthesis. *J. Am. Chem. Soc.* **2006,** *128*, 6792-6793.

35. Guyot-Sionnest, P.; Ackerman, M. M.; Tang, X., Colloidal quantum dots for infrared detection beyond silicon. *J. Chem. Phys.* **2019,** *151*, 060901.

36. Oertel, D. C.; Bawendi, M. G.; Arango, A. C.; Bulović, V., Photodetectors based on treated CdSe quantum-dot films. *Appl. Phys. Lett.* **2005,** *87*, 213505.

37. Hu, C.; Gassenq, A.; Justo, Y.; Devloo-Casier, K.; Chen, H.; Detavernier, C.; Hens, Z.; Roelkens, G., Air-stable short-wave infrared PbS colloidal quantum dot photoconductors passivated with Al2O3 atomic layer deposition. *Appl. Phys. Lett.* **2014,** *105*, 171110.

38. Sarasqueta, G.; Choudhury, K. R.; Subbiah, J.; So, F., Organic and Inorganic Blocking Layers for Solution-Processed Colloidal PbSe Nanocrystal Infrared Photodetectors. *Adv. Funct. Mater.* **2011,** *21*, 167-171.

39. Deng, Z.; Jeong, K. S.; Guyot-Sionnest, P., Colloidal Quantum Dots Intraband Photodetectors. *ACS Nano* **2014,** *8*, 11707-11714.

40. Keuleyan, S.; Lhuillier, E.; Brajuskovic, V.; Guyot-Sionnest, P., Mid-Infrared HgTe Colloidal Quantum Dot Photodetectors. *Nat. Photonics* **2011,** *5*, 489.

41. Brown, P. R.; Kim, D.; Lunt, R. R.; Zhao, N.; Bawendi, M. G.; Grossman, J. C.; Bulović, V., Energy Level Modification in Lead Sulfide Quantum Dot Thin Films through Ligand Exchange. *ACS Nano* **2014,** *8*, 5863-5872.

42. Keuleyan, S. E.; Guyot-Sionnest, P.; Delerue, C.; Allan, G., Mercury Telluride Colloidal Quantum Dots: Electronic Structure, Size-Dependent Spectra, and Photocurrent Detection up to 12 μm. *ACS Nano* **2014,** *8*, 8676-8682.

43. Guyot-Sionnest, P.; Roberts, J. A., Background Limited Mid-Infrared Photodetection with Photovoltaic HgTe Colloidal Quantum Dots. *Appl. Phys. Lett.* **2015,** *107*, 253104.

44. Tang, X.; Ackerman, M. M.; Guyot-Sionnest, P., Thermal Imaging with Plasmon Resonance Enhanced HgTe Colloidal Quantum Dot Photovoltaic Devices. *ACS Nano* **2018,** *12*, 7362-7370.

45. Tang, X.; Ackerman, M. M.; Chen, M.; Guyot-Sionnest, P., Dual-band infrared imaging using stacked colloidal quantum dot photodiodes. *Nat. Photonics* **2019,** *13*, 277-282.

46. Rizvi, S. B.; Ghaderi, S.; Keshtgar, M.; Seifalian, A. M., Semiconductor quantum dots as fluorescent probes for in vitro and in vivo bio-molecular and cellular imaging. *Nano Reviews* **2010,** *1*, 5161.

47. Coe-Sullivan, S.; Liu, W.; Allen, P.; S. Steckel, J., Quantum Dots for LED Downconversion in Display Applications. *ECS J. Solid State Sci. Technol.* **2013,** *2*, R3026-R3030.

48. le Feber, B.; Prins, F.; De Leo, E.; Rabouw, F. T.; Norris, D. J., Colloidal-Quantum-Dot Ring Lasers with Active Color Control. *Nano Lett.* **2018,** *18*, 1028-1034.

49. Dai, X.; Deng, Y.; Peng, X.; Jin, Y., Quantum-Dot Light-Emitting Diodes for Large-Area Displays: Towards the Dawn of Commercialization. *Adv. Mater.* **2017,** *29*, 1607022.

50. Ramasamy, P.; Ko, K.-J.; Kang, J.-W.; Lee, J.-S., Two-Step "Seed-Mediated" Synthetic Approach to Colloidal Indium Phosphide Quantum Dots with High-Purity Photo- and Electroluminescence. *Chem. Mater.* **2018,** *30*, 3643-3647.

51. Li, Y.; Hou, X.; Dai, X.; Yao, Z.; Lv, L.; Jin, Y.; Peng, X., Stoichiometry-Controlled InP-Based Quantum Dots: Synthesis, Photoluminescence, and Electroluminescence. *J. Am. Chem. Soc.* **2019,** *141*, 6448-6452.

52. Boldt, K.; Kirkwood, N.; Beane, G. A.; Mulvaney, P., Synthesis of Highly Luminescent and Photo-Stable, Graded Shell CdSe/CdxZn1–xS Nanoparticles by In Situ Alloying. *Chem. Mater.* **2013,** *25*, 4731-4738.

53. Lim, J.; Park, M.; Bae, W. K.; Lee, D.; Lee, S.; Lee, C.; Char, K., Highly Efficient Cadmium-Free Quantum Dot Light-Emitting Diodes Enabled by the Direct Formation of Excitons within InP@ZnSeS Quantum Dots. *ACS Nano* **2013,** *7*, 9019-9026.

54. Zhou, J.; Pu, C.; Jiao, T.; Hou, X.; Peng, X., A Two-Step Synthetic Strategy toward Monodisperse Colloidal CdSe and CdSe/CdS Core/Shell Nanocrystals. *J. Am. Chem. Soc.* **2016,** *138*, 6475-6483.

55. Horn, D. A. In *EU RoHS Recast — New requirements and impacts for the Information and Communications Technology industry*, 2012 IEEE International Symposium on Sustainable Systems and Technology (ISSST), 16-18 May 2012; 2012; pp 1-5.

56. R. Heath, J., Covalency in semiconductor quantum dots. *Chem. Soc. Rev.* **1998,** *27*, 65-71.

57. Gary, D. C.; Glassy, B. A.; Cossairt, B. M., Investigation of Indium Phosphide Quantum Dot Nucleation and Growth Utilizing Triarylsilylphosphine Precursors. *Chem. Mater.* **2014,** *26*, 1734-1744.

58. Janke, E. M.; Williams, N. E.; She, C.; Zherebetskyy, D.; Hudson, M. H.; Wang, L.; Gosztola, D. J.; Schaller, R. D.; Lee, B.; Sun, C.; Engel, G. S.; Talapin, D. V., Origin of Broad Emission Spectra in InP Quantum Dots: Contributions from Structural and Electronic Disorder. *J. Am. Chem. Soc.* **2018,** *140*, 15791-15803.

59. Chen, O.; Zhao, J.; Chauhan, V. P.; Cui, J.; Wong, C.; Harris, D. K.; Wei, H.; Han, H.-S.; Fukumura, D.; Jain, R. K.; Bawendi, M. G., Compact high-quality CdSe–CdS core–shell nanocrystals with narrow emission linewidths and suppressed blinking. *Nat. Mater.* **2013,** *12*, 445.

60. Kim, Y.; Ham, S.; Jang, H.; Min, J. H.; Chung, H.; Lee, J.; Kim, D.; Jang, E., Bright and Uniform Green Light Emitting InP/ZnSe/ZnS Quantum Dots for Wide Color Gamut Displays. *ACS Applied Nano Materials* **2019,** *2*, 1496-1504.

2. Synthesis and structural characterization of $A_2Cd_2Se_3$ (A: Na^+, NEt_4^+, or DDA^+) and its use as a composition-matched ligand for colloidal nanocrystals

Adapted with permission from M. H. Hudson *et al. J. Am. Chem. Soc.* **2017**, *139*, 9, 3368-3377.

2.1. Introduction to chalcogenidometallates.

II-VI semiconductors, the materials combining Zn, Cd, or Hg with chalcogens (O, S, Se, or Te), represent one of the most important semiconductor families and are widely utilized in solar cells,[2-3] photocatalysts,[4-5] IR detectors,[6-7] and other technologies. In recent years, significant progress has been achieved in the development of low-dimensional II-VI semiconductors in the form of quantum dots,[8-9] quantum rods,[10-12] and quantum wells (nanoplatelets)[13-14] that exhibit excellent light emission properties and are commercially used for biotags and display technologies.[15-16] Among low-dimensional semiconductors, CdSe has emerged as the most studied material and has been used as a model system in many optical[17-18] and electronic studies.[19-20]

Several synthetic methods have been developed that yield novel II-VI frameworks. Various solvothermal methods with metal salts and elemental chalcogens have been used to create species with one, two, and three-dimensional metal chalcogenide bonding frameworks with interesting morphologies and properties.[21-27] These approaches typically build up segments of metal chalcogenide lattice from molecular precursors. Interestingly, low-dimensional metal chalcogenides can also be accessed through disassembly of the bulk crystalline lattice. For example, Mitzi and coworkers utilized the reducing power of hydrazine to dissolve bulk metal chalcogenides in an excess of chalcogen at room temperature to generate soluble

chalcogenidometallates.[28-35] Mitzi's approach produced chalcogenidometallates of Sn (S, Se, Te), Cu (S, Se), Ge (S, Se), In (Se, Te), and Zn (Te), but soluble products for many technologically important metal chalcogenides could not be obtained with this approach.

We recently reported the synthesis of soluble chalcogenidometallate species for Cd, Pb, and Bi chalcogenides by combining strongly reducing chalcogenide salts (Na_2Ch, K_2Ch) with a bulk metal chalcogenide in hydrazine.[36] These complexes were explored for their utility as "solders" for II-VI semiconductors. For example, a solution of the chalcogenidometallate could be mixed with ball-milled semiconductor powder and heated to 300 °C to form a polycrystalline film with good mechanical stability and electrical properties. These chalcogenidometallates also showed remarkable success as inorganic capping ligands for quantum dots; nanocrystals could be capped with composition-matched ligands and annealed at 300 °C to form polycrystalline metal chalcogenide films. Electron mobilities above 300 $cm^2V^{-1}s^{-1}$ were obtained for annealed films of CdSe nanocrystals capped with sodium selenocadmate, achieving half the mobility of single crystalline CdSe and far surpassing previously obtained mobilities for solution-processed films.[36-37]

In this study we report the structure of a polymeric form of $[Cd_2Se_3]_n^{2n-}$ which represents, to the best of our knowledge, the first molecular motif with a one-dimensional CdSe bonding framework. The negative charge of the $[Cd_2Se_3]_n^{2n-}$ chain can be balanced with various inorganic or organic cations. The choice of cation can be used to tune the solubility of $[Cd_2Se_3]_n^{2n-}$ wires in polar and non-polar solvents. Moreover, we show that $[Cd_2Se_3]_n^{2n-}$ can act as a stabilizing ligand for CdSe nanocrystals in solvents other than hydrazine, creating a more versatile composition-matched nanocrystal ink.

2.2. $Na_2Cd_2Se_3$ synthesis and crystal structure.

Bulk CdSe powder completely dissolves in liquid hydrazine at room temperature in the presence of 0.5 molar equivalents of Na_2Se. After several days of stirring, the solution becomes colorless, and the chalcogenidometallate product can be isolated by addition of acetonitrile followed by centrifugation to yield a white powder. Inductively coupled plasma optical emission spectroscopy (ICP-OES) indicates that the product has the empirical formula $Na_2Cd_2Se_3$. This sodium selenocadmate is soluble up to ~0.05 M (25 mg/mL) in hydrazine.

To characterize this new chalcogenidometallate compound, colorless, platelike crystals were grown by slow evaporation of hydrazine from a ~0.025 M $Na_2Cd_2Se_3$ solution over the course of two weeks, and the structure was revealed by single crystal x-ray diffraction. The diffraction results show that this complex crystallizes in the $P\bar{1}$ space group with an asymmetric unit of $Na_4Cd_4Se_6 \cdot 9.5\ N_2H_4$ (Figures 2.1-2.2). The selenocadmate anionic framework has a one-dimensional structure of double chains of distorted edge-sharing [$CdSe_4$] tetrahedra running along the *c*-axis. The structure contains bridging Se^{2-} anions coordinated by four Cd^{2+} cations with bond distances ranging from 2.7210(7) to 2.7981(7) Å and terminal Se^{2-} anions bound to two Cd^{2+} cations through shorter bonds from 2.6075(7) to 2.6280(7) Å. These $(Cd_2Se_3)_n^{2n-}$ chains are charge balanced by Na^+ cations. The Na^+ either bridges two Se^{2-} or is bound to a single Se^{2-} with average Na-Se bond lengths of ~3 Å; the coordination sphere around Na^+ is filled with hydrazine in either an octahedral or trigonal bipyramidal configuration. Adjacent $(Cd_2Se_3)_n^{2n-}$ chains are connected by Na^+-hydrazine-Na^+ bridges, facilitating mutual alignment of the chains along the *c*-axis. Further details on the diffraction data are provided in Table 2.1.

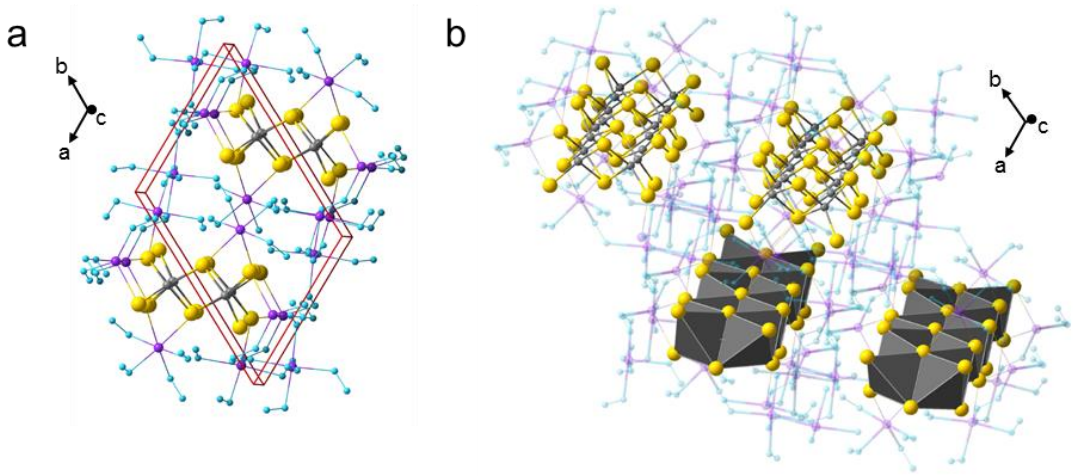

Figure 2.1. $Na_4Cd_4Se_6 \cdot 9.5\ N_2H_4$ crystal structure.
Single crystal structure for $Na_4Cd_4Se_6 \cdot 9.5\ N_2H_4$, where grey spheres represent Cd, yellow is Se, purple is Na, and blue is N: *(a)* viewed down the *c*-axis with hydrogen atoms omitted for clarity with the unit cell outlined in red ($P\bar{1}$, a = 10.5623(10) Å, b = 13.5662(12) Å, c = 13.6038(11) Å, α = 104.728(3)°, β = 108.183(3)°, γ = 111.179(3)°, Z = 2); *(b)* a view highlighting Cd and Se chalcogenidometallate framework to demonstrate its wire-like morphology.

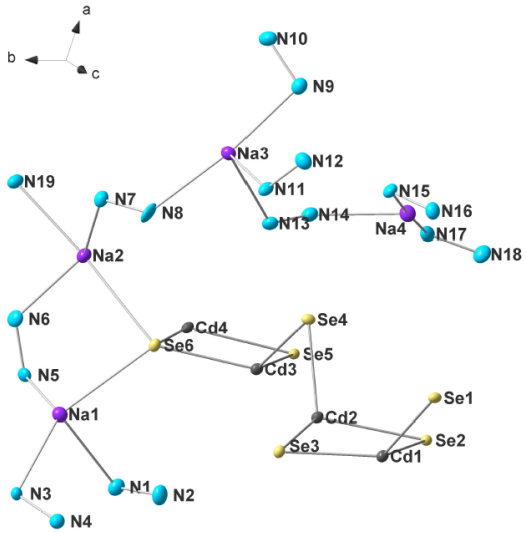

Figure 2.2. Asymmetric unit of the $Na_4Cd_4Se_6 \cdot 9.5\ N_2H_4$ crystal structure.
Asymmetric unit with labeled atoms for the crystal structure $Na_4Cd_4Se_6 \cdot 9.5\ N_2H_4$, with hydrogen removed for clarity.

Table 2.1. Crystal data and structure refinement for $Na_4Cd_4Se_6 \cdot 9.5N_2H_4$.

Empirical formula	$Cd_4H_{38}N_{19}Na_4Se_6$
Formula weight	1319.81
Temperature/K	100(2)
Crystal system	triclinic
Space group	*P*-1
a/Å	10.5623(10)
b/Å	13.5662(12)
c/Å	13.6038(11)
α/°	104.728(3)
β/°	108.183(3)
γ/°	111.179(3)
Volume/$Å^3$	1571.7(2)
Z	2
$\rho_{calc}g/cm^3$	2.789
μ/mm^{-1}	9.701
F(000)	1222.0
Crystal size/mm^3	0.2 × 0.04 × 0.01
Radiation	MoKα (λ = 0.71073)
2Θ range for data collection/°	4.364 to 57.736
Index ranges	$-13 \leq h \leq 14$, $-17 \leq k \leq 18$, $-18 \leq l \leq 17$
Reflections collected	42225
Independent reflections	7134 [R_{int}* = 0.0452, R_{sigma} = 0.0444]
Data/restraints/parameters	7134/6/320
Goodness-of-fit† on F^2	1.076
Final R indexes [I>=2σ (I)]	R_1‡ = 0.0368, wR_2‖ = 0.0732
Final R indexes [all data]	R_1 = 0.0591, wR_2 = 0.0796
Largest diff. peak/hole / e $Å^{-3}$	2.61/-0.97

*$R_{int} = \Sigma \mid F_o^2 - \langle F_o^2 \rangle \mid / \Sigma \mid F_o^2 \mid$

†Goodness-of-fit = $[\Sigma [w (F_o^2 - F_c^2)^2] / (n-p)]^{1/2}$

n: number of independent reflections; p: number of refined parameters

‡$R_1 = \Sigma \mid \mid F_o \mid - \mid F_c \mid \mid / \Sigma \mid F_o \mid$

‖$wR_2 = [\Sigma [w (F_o^2 - F_c^2)^2] / \Sigma [w (F_o^2)^2]]^{1/2}$

The structure of sodium selenocadmate shares aspects of both neutral low-dimensional metal chalcogenides and anionic chalcogenidometallates. Low-dimensional metal chalcogenides have been synthesized solvothermally from a metal salt and elemental chalcogen, and the

resulting structures are one, two, or three-dimensional segments of the bulk lattice.[21-23, 25, 38-39] The extended one-dimensional framework of $Na_2Cd_2Se_3$ is similar to that of the solids $SnS_4Mn_2(N_2H_4)_6$ and ZnTe(1,3-propanediamine) or the hydrazine-soluble species $(N_2H_4)ZnTe$.[23, 31, 39] However, $(Cd_2Se_3)_n^{2n-}$ deviates from the bulk structure of corner-sharing $[CdSe_4]$ tetrahedra and demonstrates the bonding motif of edge-sharing tetrahedra. Edge-sharing brings the cations into closer proximity, yielding a Cd-Cd distance of ~3.34 Å in $Na_2Cd_2Se_3$ compared to a Cd-Cd distance of 4.3 Å in wurtzite CdSe. This suggests greater covalent character that limits the repulsion of the Cd cationic centers. The divergence from the bulk structure in favor of edge-sharing tetrahedra is seen in many small molecular chalcogenidometallates (*e.g.* $Sn_2S_6^{4-}$, $Sn_2Se_6^{4-}$, and $Ge_2Se_6^{4-}$)[28, 30] and is exhibited by the extended one-dimensional tellurocadmate polyanion $(CdTe_2)_n^{2n-}$.[36]

2.3. Extension of selenocadmate stability to non-hydrazine solvents.

The toxicity and instability of hydrazine make the use of other solvents desirable for solution processing; however, sodium selenocadmate has not been appreciably soluble in other solvents tested (DMF, NMF, FA, DMSO, and en). We found that the solubility and versatility of selenocadmate can be expanded by exchanging the charge-balancing cation as schematically shown in Figure 2.3. Sodium ions can be replaced with tetraethylammonium by stirring a $Na_2Cd_2Se_3$ solution with an excess of NEt_4^+-loaded Amberlyst-15 cation exchange resin, and the resulting $(NEt_4)_2Cd_2Se_3$ is soluble in hydrazine, 85:15 acetonitrile:hydrazine, *N*-methylformamide (NMF), and dimethyl sulfoxide (DMSO). The solubility can be extended to nonpolar solvents by replacing sodium with didodecyldimethylammonium (DDA^+). This cation exchange takes place in a two-phase system where solutions of didodecyldimethylammonium

bromide (DDAB) in toluene or hexane and $Na_2Cd_2Se_3$ in hydrazine are stirred, and the selenocadmate transfers to the nonpolar phase. UV-vis spectra for cation-exchanged selenocadmate in a variety of polar and nonpolar solvents are given in Figure 2.4.

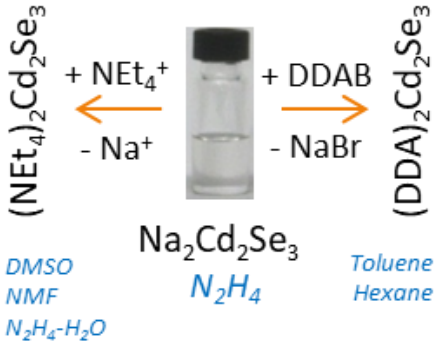

Figure 2.3. Schematic for $[Cd_2Se_3]_n^{2n-}$ cation exchange.
Cation exchange with tetraethylammonium (NEt_4^+) or didodecyldimethylammonium (DDA^+) enables the solubility of selenocadmate in various polar and non-polar solvents.

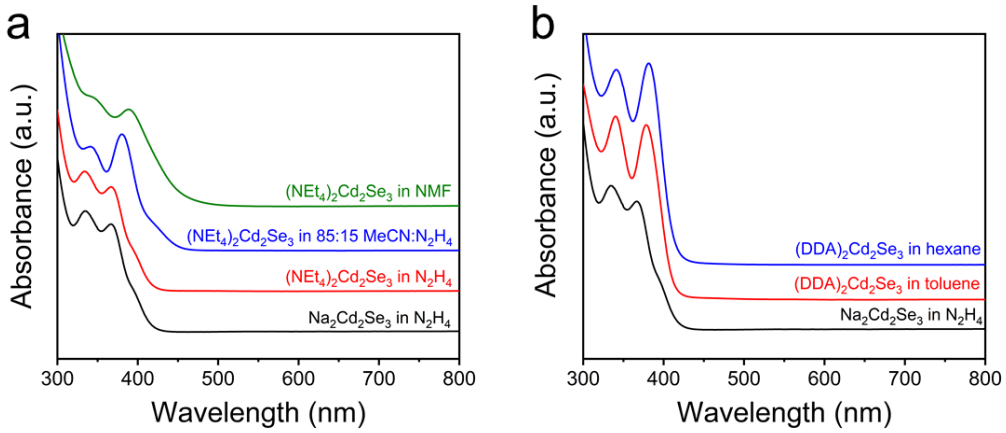

Figure 2.4. UV-vis spectra of cation-exchanged $[Cd_2Se_3]_n^{2n-}$.
UV-vis absorbance spectra suggest that cation exchange does not change the anion and subtle changes are seen with changing solvent. These spectra show *(a)* $(NEt_4)_2Cd_2Se_3$ in various polar solvents and *(b)* $(DDA)_2Cd_2Se_3$ in nonpolar solvents with comparison to $Na_2Cd_2Se_3$ in hydrazine.

2.4. EXAFS analysis of the solution structure of $Na_2Cd_2Se_3$ and $(NEt_4)_2Cd_2Se_3$.

The solution structure of the selenocadmate species in hydrazine was further evaluated with extended x-ray absorption fine structure (EXAFS) at the Cd and Se K-edges. EXAFS allows one to probe the coordination environment around a specific atom for a powder, film, or solution sample. The oscillations in the x-ray absorbance above the energy necessary to eject a core electron from the atom of interest can be modelled to determine the identity, number, and distance to atoms surrounding the probed atom.[40] We measured EXAFS at the Cd (26.711 keV) and Se (12.658 keV) K-edges for CdSe powder and solutions of $Na_2Cd_2Se_3$ and $(NEt_4)_2Cd_2Se_3$ in hydrazine (Figure 2.5).

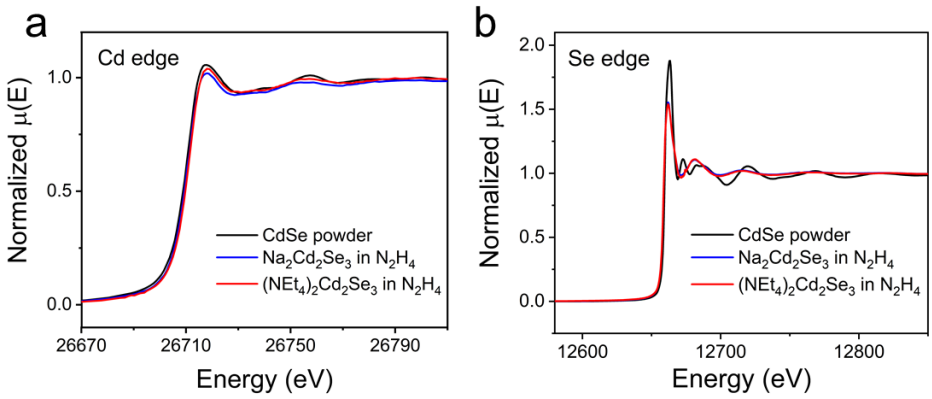

Figure 2.5. Raw EXAFS data for selenocadmate solutions.
Raw EXAFS data for CdSe powder and solutions of $Na_2Cd_2Se_3$ and $(NEt_4)_2Cd_2Se_3$ in hydrazine at the Cd (26.711 keV) and Se (12.658 keV) K-edges.

EXAFS data reduction and analysis were conducted with the Demeter suite of x-ray absorption spectroscopy software.[41] Athena was used for background removal, deglitching, and data reduction. Artemis was used to fit the data to determine the amplitude reduction factor (S_0^2), bond length (R), number of nearest neighbors (N), edge energy (E_0), and the Debye-Waller factor. The amplitude reduction factor was obtained from fitting known standards at each energy,

Cd foil, Se foil, and CdSe powder, where appropriate. This value was then set for the other fits such that the number of nearest neighbors could be a free parameter in the fit.

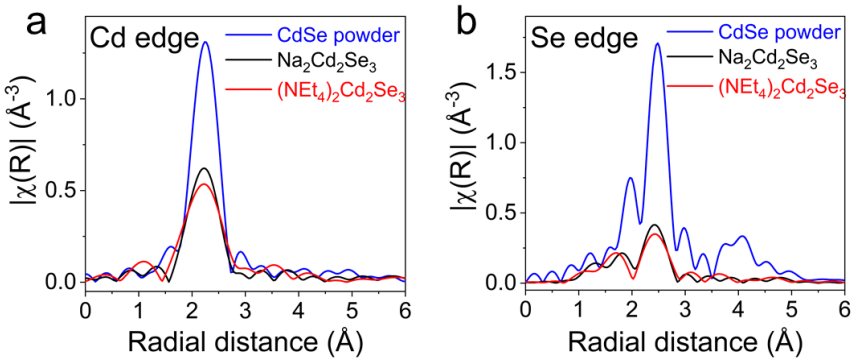

Figure 2.6. R-space plots for selenocadmate EXAFS data.
Plots of the Fourier-transformed absorption probability (R-space plots) from the *(a)* Cd and *(b)* Se K-edges demonstrate the reduced coordination number and increased disorder for $Na_2Cd_2Se_3$ and $(NEt_4)_2Cd_2Se_3$ species in solution as compared to bulk CdSe.

Plots of the Fourier-transformed absorption probability (R-space plots) can be examined both qualitatively and through quantitative fitting to provide insight into the structure of selenocadmate in hydrazine solution. Qualitatively, the plots of the Fourier-transformed absorption probability suggest that the selenocadmate structure differs significantly from that of bulk CdSe but does not change dramatically with cation exchange (Figure 2.6). The reduced amplitude of the Fourier-transformed x-ray absorption for selenocadmate compared to that of bulk CdSe suggests that these species have fewer nearest neighbor contacts between Cd and Se; though the similar shape of the curves indicates that the distance between Cd and Se in selenocadmate is consistent with bulk bond lengths. A more quantitative understanding of the solution structure of selenocadmate can be obtained from fitting the Fourier-transformed absorption probability at each absorption edge. The details of a first-shell fit for bulk CdSe powder and $Na_2Cd_2Se_3$ and $(NEt_4)_2Cd_2Se_3$ solutions in hydrazine at the Cd and Se edges are given in Figures 2.7-2.8 and Table 2.2 and agree with the qualitative conclusions above. The

coordination numbers for Cd and Se based on the crystal structure of solid $Na_2Cd_2Se_3$ are higher than those predicted by fitting EXAFS data; this suggests that in solution the selenocadmate ions exist as smaller fragments that reorganize into long chains as hydrazine is removed. The signal-to-noise ratio of the EXAFS data was limited by the low solubility of selenocadmate, complicating further quantitative analysis of the EXAFS fits.

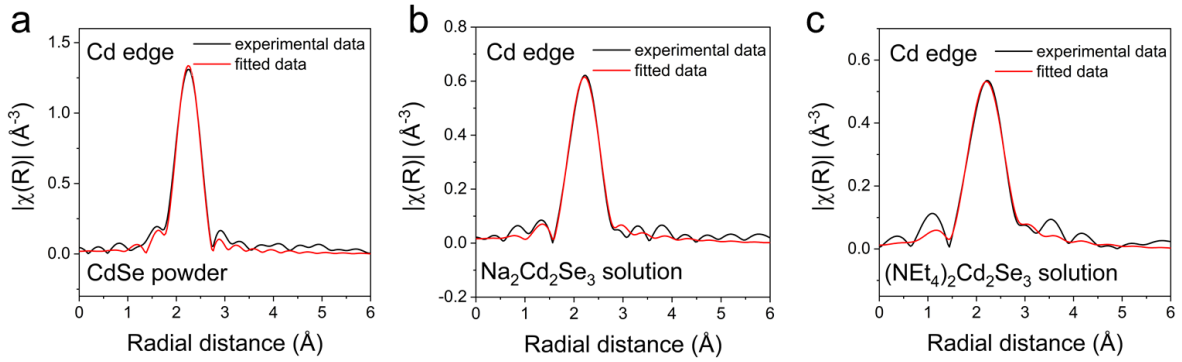

Figure 2.7. Fits to selenocadmate EXAFS data at the Cd K-edge.
Magnitude of the Fourier-transformed EXAFS experimental data and fitted data for *(a)* CdSe powder, *(b)* $Na_2Cd_2Se_3$ in N_2H_4, and *(c)* $(NEt_4)_2Cd_2Se_3$ in N_2H_4 at the Cd K-edge.

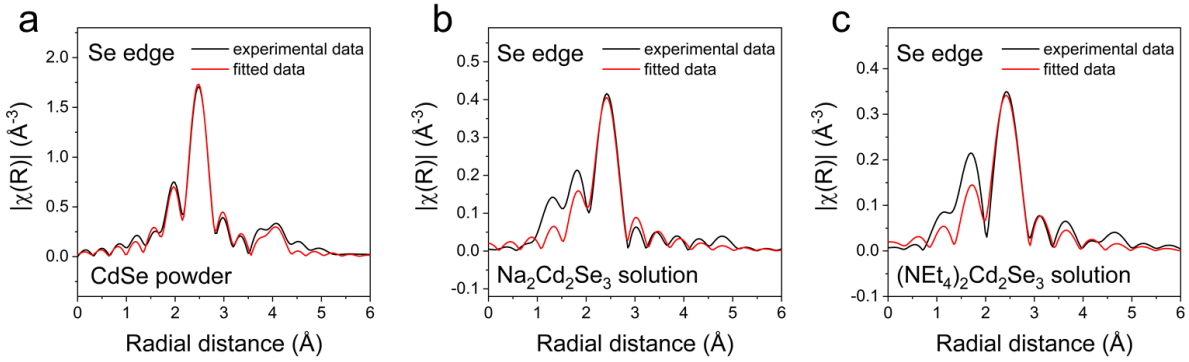

Figure 2.8. Fits to selenocadmate EXAFS data at the Se K-edge.
Magnitude of the Fourier-transformed EXAFS experimental data and fitted data for *(a)* CdSe powder, *(b)* $Na_2Cd_2Se_3$ in N_2H_4, and *(c)* $(NEt_4)_2Cd_2Se_3$ in N_2H_4 at the Se K-edge.

Table 2.2. EXAFS fitting parameters for bulk CdSe and selenocadmate.

		Path	Bond length (Å)	Coordination number	E_0	Debye-Waller factor	R
Cd K-edge (26.711 keV) S_0^2 = 1.05	**CdSe powder** R: 1.6 – 3.5 k: 4 – 12.5	Cd-Se_1	2.61 ± 0.02	3 (set)	5 ± 2	0.004 ± 0.002	0.006
		Cd-Se_2	2.75 ± 0.04	1 (set)		0.003 ± 0.006	
	$Na_2Cd_2Se_3$ in N_2H_4 R: 1.2 – 3.5 k: 3.5 – 10.5	Cd-Se	2.606 ± 0.007	2.4 ± 0.3	3 ± 1	0.0065 ± 0.0009	0.008
	$(NEt_4)_2Cd_2Se_3$ in N_2H_4 R: 1.5 – 4 k: 3.7 – 9.5	Cd-Se	2.605 ± 0.010	2.1 ± 0.3	4 ± 2	0.005 ± 0.001	0.010
Se K-edge (12.658 keV) S_0^2 = 1.00	**CdSe powder** R: 1.6 – 4.5 k: 3.2 – 11.9	Se-Cd_1	2.61 ± 0.02	3 (set)	1.4 ± 0.8	0.009 ± 0.004	0.010
		Se-Cd_2	2.63 ± 0.02	1 (set)		0.002 ± 0.001	
		Se-Se	4.31 ± 0.02	12 (set)		0.020 ± 0.003	
	$Na_2Cd_2Se_3$ in N_2H_4 R: 2 – 4 k: 3.8 – 11	Se-Cd	2.588 ± 0.007	1.0 ± 0.1	-2 ± 1	0.005 ± 0.001	0.016
	$(NEt_4)_2Cd_2Se_3$ in N_2H_4 R: 2 – 4.2 k: 3.7 – 9.8	Se-Cd	2.57 ± 0.01	1.0 ± 0.2	-3 ± 2	0.005 ± 0.002	0.028

We examined similarities between the selenocadmate species and previously reported CdSe clusters using absorbance spectroscopy and EXAFS. The electronic structure of selenocadmate in solution was explored with UV-vis spectroscopy. Both sodium and tetraethylammonium selenocadmate in hydrazine show similar absorption spectra with peaks at 332 nm and 363 nm and a shoulder around 390 nm (Figure 2.4). The close similarity of the spectra indicates that changing the cation does not significantly change the electronic structure of the selenocadmate anion. Interestingly, the absorbance frequencies in these spectra are similar to those seen for CdSe clusters.[42-45] However, comparison of EXAFS data for sodium selenocadmate and CdSe clusters clearly demonstrates that they are distinct species (Figure 2.9). This suggests that the UV absorption peaks may correspond to localized excitations of Cd-Se bonds and may be generic to all molecular CdSe species.

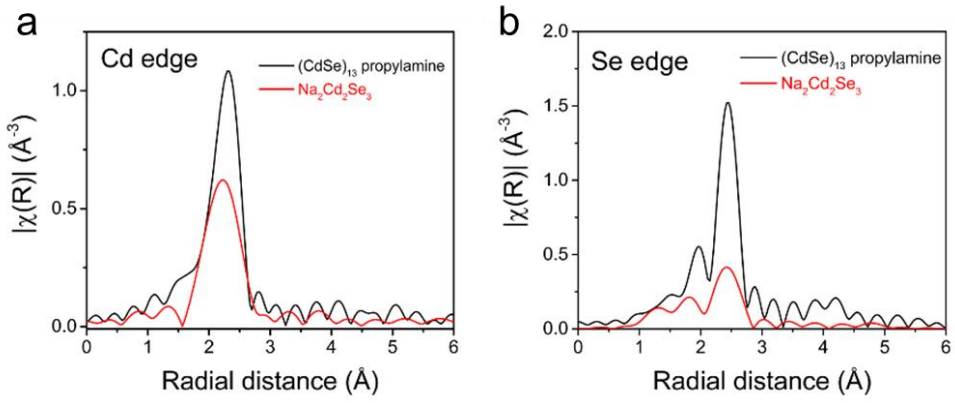

Figure 2.9. EXAFS comparison of selenocadmate and $(CdSe)_{13}$ clusters.
Magnitude of the Fourier-transformed absorption probability for $(CdSe)_{13}$ clusters with propylamine ligands and $Na_2Cd_2Se_3$ at the *(a)* Cd and *(b)* Se K-edges, demonstrating that the coordination environments are different for the two species.

2.5. Molecular selenocadmates as capping ligands for colloidal nanocrystals.

In previous studies we have shown that chalcogenidometallates can be effective capping ligands for colloidal nanoparticles.[36, 46] When a solution of $Na_2Cd_2Se_3$ in hydrazine is added to a

solution of CdSe nanoparticles capped with *n*-octadecylphosphonate (ODPA) ligands in toluene, the surface ligands exchange from ODPA to $(Cd_2Se_3)_n^{2n-}$ and the nanoparticles transfer to the hydrazine phase (Figure 2.10a). Washing the hydrazine phase with excess toluene removes organics and yields a solution of inorganic-capped CdSe. A transmission electron microscope (TEM) image shows that the CdSe nanoparticles retain their morphology upon ligand exchange (Figure 2.10b), and infrared (IR) spectroscopy indicates the organic ligands are completely removed (Figure 2.10c). Solutions of $Cd_2Se_3^{2-}$-capped CdSe in hydrazine can be spin-coated onto substrates and annealed at 300 °C to form large grains of polycrystalline CdSe, and field-effect transistors constructed from these films yield electron mobilities of ~300 $cm^2V^{-1}s^{-1}$.[36-37] This remarkable electron mobility suggests that the composition-matched ligands not only foster semiconductor grain growth during annealing but also improve electronic transport across the grain boundaries, serving as a solder that retains semiconductor performance.

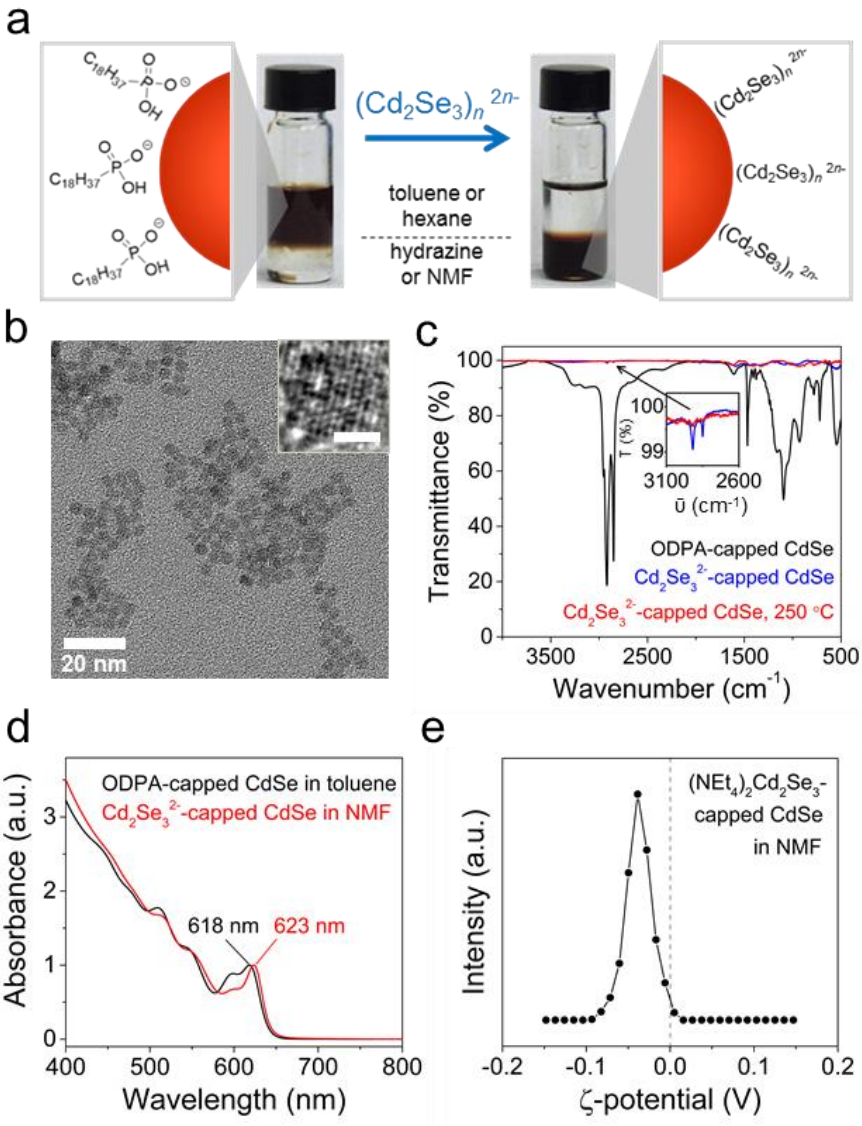

Figure 2.10. Characterization of selenocadmate-capped CdSe nanoparticles.
(a) Schematic showing the ligand exchange of CdSe nanoparticles from ODPA to $(Cd_2Se_3)_n^{2n-}$ and the corresponding phase transfer. *(b)* TEM image of $Na_2Cd_2Se_3$-capped CdSe nanoparticles with an inset showing lattice fringes, scale bar 2 nm. *(c)* IR spectra show that signals corresponding to organic ligands decrease dramatically after ligand exchange with $Na_2Cd_2Se_3$. *(d)* UV-vis spectra for solutions of ODPA-capped CdSe in toluene and $(NEt_4)_2Cd_2Se_3$-capped CdSe in NMF. *(e)* A zeta potential measurement of $(NEt_4)_2Cd_2Se_3$-capped CdSe in NMF with the peak centered at approximately -40 mV, indicating that the particles are electrostatically stabilized.

As described above, the use of hydrazine as a solvent limits the conditions under which the solution can be used. We found that performing ligand exchange with $(NEt_4)_2Cd_2Se_3$ rather

than $Na_2Cd_2Se_3$ yields $Cd_2Se_3^{2-}$-capped nanoparticles that can be dissolved in the more benign solvent *N*-methylformamide (NMF). Ligand exchange was performed as described above with a solution of $(NEt_4)_2Cd_2Se_3$ in hydrazine. The ligand-exchanged nanoparticles could be precipitated with an excess of acetonitrile and dissolved in NMF. UV-vis measurements of solution of CdSe nanoparticles before and after ligand exchange indicate that the nanoparticles have retained their size and transferred into the polar solvent (Figure 2.10d). The zeta potential of the $Cd_2Se_3^{2-}$-capped CdSe in NMF was approximately -40 mV, suggesting that $(Cd_2Se_3)_n^{2n-}$ is bound to the nanocrystals and stabilizes the nanocrystals in solution via charge repulsion (Figure 2.10e). Comparable zeta potentials have been measured for many chalcogenidometallate-capped nanoparticles.[46] The stable solution of $Cd_2Se_3^{2-}$-capped CdSe in NMF may serve as a useful ink for the deposition of solution-processed CdSe films where hydrazine cannot be used, for instance due to health concerns or chemical incompatibilities (*e.g.* Kapton polymer substrates).

2.6. Conclusions.

In this work, we have explored the structure and versatility of the low-dimensional semiconductor precursor $Na_2Cd_2Se_3$. Using single crystal x-ray diffraction, we showed that the crystal structure consists of infinite one-dimensional wires of edge-sharing [$CdSe_4$] units with sodium serving as a charge-balancing cation. EXAFS analysis of $Na_2Cd_2Se_3$ in solution revealed that this infinite one-dimensional structure is broken into smaller units in hydrazine. The $Na_2Cd_2Se_3$ moiety has demonstrated utility as a semiconductor solder when used from hydrazine solution,[36-37] but the toxicity and chemical incompatibility of hydrazine limit its applications. We demonstrated that cation exchange to form $(NEt_4)_2Cd_2Se_3$ or $(DDA)_2Cd_2Se_3$ extends the selenocadmate solubility to a variety of polar and nonpolar solvents without significant impacts

on $(Cd_2Se_3)_n^{2n-}$ structure and function. It was shown that $(NEt_4)_2Cd_2Se_3$ can serve as a ligand for CdSe nanoparticles and can be used to create a composition-matched nanocrystal ink in the more benign solvent NMF. Future work will explore the use of $Na_2Cd_2Se_3$ and $(NEt_4)_2Cd_2Se_3$, alone and in composites with CdSe nano- and microparticles, to make solution-processed CdSe devices.

2.7. Materials and methods.

All manipulations were performed in a nitrogen glove box with < 10 ppm oxygen and water levels, unless otherwise noted.

Materials. Selenium (pellet, 99.99%, Aldrich), cadmium selenide (99.99%, Aldrich), sodium hydride (dry, 95%, Aldrich), cadmium oxide (≥99.9%, Aldrich), tri-*n*-octylphosphine oxide (TOPO, 99%, Aldrich), tri-*n*-octylphosphine (TOP, 97%, Strem), 1-octadecene (ODE, 90%, Aldrich), tetraethylammonium hydroxide solution (~25% in methanol, Aldrich), Amberlyst 15 hydrogen form cation exchange resin (strongly acidic, dry, Aldrich), didodecyldimethylammonium bromide (DDAB, 98%, Aldrich), acetonitrile (MeCN, anhydrous, 99.8%, Aldrich), toluene (anhydrous, 99.8%, Aldrich), ethanol (anhydrous, 99.5%, Aldrich), and *N*-methylformamide (NMF, 99%, Alfa Aesar) were used as received. Hydrazine (N_2H_4, anhydrous, 98%, Aldrich) was distilled under nitrogen and used in a nitrogen glove box. Formamide (FA, 99+%, Acros) was dried and stored over molecular sieves. Octadecylphosphonic acid (ODPA, 99%, TCI) was recrystallized for CdSe nanoparticle synthesis.

Synthesis of Na_2Se. 0.25 mL of a 1 M Se solution in hydrazine (deep green color) was added to 12 mg (0.5 mmol) NaH powder dropwise over the course of approximately 30 minutes. The resulting Na_2Se suspension should be colorless/pale yellow or slightly pink; if the solution is very pink, small amounts of NaH are added until no longer pink.

Synthesis of $Na_2Cd_2Se_3$. 0.25 mmol Na_2Se was combined with 96 mg (0.5 mmol) CdSe powder in 10 mL hydrazine. This mixture was stirred at room temperature until colorless and the dark solid dissolved, about 5 days. The solution was filtered through a 0.45 μm PTFE syringe filter to remove any unreacted solids. The product was isolated by adding acetonitrile as nonsolvent and centrifuging to isolate a white solid. The solid was dissolved in hydrazine at concentrations up to ~0.05 M.

Growth of $Na_4Cd_4Se_6 \cdot 9.5\ N_2H_4$ crystals. Single crystals of $Na_2Cd_2Se_3$ were grown by slow evaporation of the hydrazine solvent. A solution of ~0.0125 M $Na_2Cd_2Se_3$ in hydrazine was loaded into a clean, dry glass tube in the glove box. The tube had a 100° bend in the midsection and solution was loaded to fill one side of the bend halfway (~0.5 mL). The tube was temporarily sealed under nitrogen, removed from the glove box, and flame sealed under mild vacuum. The side of the tube containing the solution was suspended over a warm hot plate (80 °C) and the other side was at room temperature. Over the course of about 2 weeks, the hydrazine evaporated from the warm side and collected in the cool side, leaving behind plate-like crystals.

NEt_4^+ cation exchange. To create $(NEt_4)_2Cd_2Se_3$, Amberlyst 15 highly acidic cation exchange resin was loaded with the desired cation and mixed in 10x excess with $Na_2Cd_2Se_3$. 1 mg resin

was rinsed with 3 mL ~1.5 M $(NEt_4)OH$ in methanol 3 times and then dried under vacuum at 60 °C for an hour. After cation exchange, any excess resin was removed by filtering the solution through a 0.45 μm PTFE syringe filter.

CdSe nanocrystal synthesis. TOPO (6 g), recrystallized ODPA (560 mg), and CdO (120 mg) were combined in a round bottom flask and degassed at 150 °C for 1.5 hours. The solution was then heated to 370 °C under nitrogen and TOP (3 g) was injected. When the temperature recovered to 370 °C, 840 mg of a 1.7 M solution of Se in TOP was injected. The reaction mixture was heated at 370 °C for 5 minutes and then naturally cooled to room temperature. The nanocrystals were dispersed in toluene and precipitated with ethanol nonsolvent; this washing procedure was repeated 3 times before storage in a nitrogen glove box. For ligand exchange experiments, nanocrystals were washed an additional 5 times with methanol and 4 times with ethanol in the glove box.

Using $Na_2Cd_2Se_3$ as ligands for colloidal CdSe nanocrystals. Ligand exchange from ODPA to $Na_2Cd_2Se_3$ or $(NEt_4)_2Cd_2Se_3$ was performed with slight modifications to a literature procedure.[36] 1.4 mL of a solution of ODPA-capped CdSe nanocrystals (~4 mg/mL) was layered atop 1.4 mL of a $Na_2Cd_2Se_3$ solution in hydrazine (~7 mM). The solution was briefly vortexed, and the nanocrystals transferred to the hydrazine layer. The toluene-rich phase was removed, and the hydrazine-rich phase was washed 3 times with 1.4 mL fresh toluene. Then the nanocrystal solution in hydrazine was filtered through a 0.2 μm PTFE syringe filter. This solution was then precipitated with the addition of acetonitrile nonsolvent (~1:1 hydrazine:acetonitrile), and the nanocrystals were redispersed in hydrazine. The above procedure was repeated for

$(NEt_4)_2Cd_2Se_3$-capped CdSe, but the final step required more nonsolvent to precipitate the nanocrystals.

Characterization.

Single crystal x-ray diffraction. All manipulations on the crystals including mounting were carried out under N_2 in a glove bag. Crystals tend to lose crystallinity and are air/moisture sensitive. A brown plate-like crystal ($0.01 \times 0.04 \times 0.20$ mm^3) was mounted on a Dual-Thickness MicroMount^{tm} (MiTeGen) with 20 μm sample aperture with Fluorolube™ oil. The diffraction data were measured at 100 K on a Bruker D8 VENTURE diffractometer equipped with a microfocus Mo-target X-ray tube (λ = 0.71073 Å) and PHOTON 100 CMOS detector. Data reduction and integration were performed with the Bruker APEX3 software package (Bruker AXS, version 2015.5-2, 2015). Data were scaled and corrected for absorption effects using the multi-scan procedure as implemented in SADABS (Bruker AXS, version 2014/5, 2015, part of Bruker APEX3 software package). The structure was solved by SHELXT (Version 2014/5)[47] and refined by a full-matrix least-squares procedure using OLEX2[48] (XL refinement program version 2014/7).[49] All atoms were refined with anisotropic thermal parameters. Some hydrogen atoms were found in the difference Fourier map and refined with distance restraints. Otherwise, they were included in idealized geometric positions for structure factor calculations.

Extended x-ray absorption fine structure (EXAFS). EXAFS measurements were conducted at the X-ray Science Division (XSD) beamlines 20-ID and 20-BM at the Advanced Photon Source, Argonne National Laboratory. Measurements were collected at the Se K edge (12,658 eV) and Cd K edge (26,711 eV) for solutions of $Na_2Cd_2Se_3$ and $(NEt_4)_2Cd_2Se_3$ in hydrazine and CdSe

powder. Solution samples were measured in plastic cuvettes sealed under nitrogen and CdSe powder was prepared as a pellet diluted with BN and sealed in Kapton tape. Reference spectra for the Cd and Se edges were measured on Cd foil and Se foil, respectively. Data reduction and analysis were conducted with the Demeter suite of x-ray absorption spectroscopy software.[41]

Optical absorption. UV-vis measurements were collected with a Cary 5000 UV-Vis-NIR spectrophotometer.

Transmission electron microscopy (TEM). TEM images were obtained on an FEI Technai F30 microscope at 300 kV.

Zeta potential. Zeta potential of a dilute filtered solution of $(NEt_4)_2Cd_2Se_3$-capped CdSe nanocrystals in NMF was measured with a Zetasizer Nano-ZS (Malvern Instruments). The sample was held in a glass cuvette with an immersed dip cell with palladium electrodes, and the applied bias was 5 V.

Infrared (IR) spectroscopy. Infrared spectra were collected with a Thermo Nexus 670 FTIR in transmission mode. Samples were prepared as drop cast films on KBr pellets.

2.8. Chapter 2 bibliography.

1. Hudson, M. H.; Dolzhnikov, D. S.; Filatov, A. S.; Janke, E. M.; Jang, J.; Lee, B.; Sun, C.; Talapin, D. V., New Forms of CdSe: Molecular Wires, Gels, and Ordered Mesoporous Assemblies. *J. Am. Chem. Soc.* **2017,** *139*, 3368-3377.

2. Burst, J. M.; Duenow, J. N.; Albin, D. S.; Colegrove, E.; Reese, M. O.; Aguiar, J. A.; Jiang, C. S.; Patel, M. K.; Al-Jassim, M. M.; Kuciauskas, D.; Swain, S.; Ablekim, T.; Lynn, K.

G.; Metzger, W. K., CdTe solar cells with open-circuit voltage breaking the 1 V barrier. *Nat. Energy* **2016,** *1*, 16015.

3. Zhang, H.; Kurley, J. M.; Russell, J. C.; Jang, J.; Talapin, D. V., Solution-Processed, Ultrathin Solar Cells from CdCl3–-Capped CdTe Nanocrystals: The Multiple Roles of CdCl3–Ligands. *J. Am. Chem. Soc.* **2016,** *138*, 7464-7467.

4. Amirav, L.; Alivisatos, A. P., Photocatalytic Hydrogen Production with Tunable Nanorod Heterostructures. *J. Phys. Chem. Lett.* **2010,** *1*, 1051-1054.

5. Kudo, A.; Miseki, Y., Heterogeneous photocatalyst materials for water splitting. *Chem. Soc. Rev.* **2009,** *38*, 253-278.

6. Keuleyan, S.; Lhuillier, E.; Brajuskovic, V.; Guyot-Sionnest, P., Mid-infrared HgTe colloidal quantum dot photodetectors. *Nat. Photon.* **2011,** *5*, 489-493.

7. Guyot-Sionnest, P.; Roberts, J. A., Background Limited Mid-Infrared Photodetection with Photovoltaic HgTe Colloidal Quantum Dots. *Appl. Phys. Lett.* **2015,** *107*, 253104.

8. Murray, C. B.; Kagan, C. R.; Bawendi, M. G., Synthesis and characterization of monodisperse nanocrystals and close-packed nanocrystal assemblies. *Annu. Rev. Mater. Sci.* **2000,** *30*, 545-610.

9. Murray, C. B.; Norris, D. J.; Bawendi, M. G., Synthesis and characterization of nearly monodisperse CdE (E = sulfur, selenium, tellurium) semiconductor nanocrystallites. *J. Am. Chem. Soc.* **1993,** *115*, 8706-8715.

10. Peng, X.; Manna, L.; Yang, W.; Wickham, J.; Scher, E.; Kadavanich, A.; Alivisatos, A. P., Shape control of CdSe nanocrystals. *Nature* **2000,** *404*, 59-61.

11. Milliron, D. J., Hughes, S.M., Cui, Y., Manna, L., Li, J., Wang, L.-W., Alivisatos, A.P., Colloidal nanocrystal heterostructures with linear and branched topology. *Nature* **2004,** *430*, 190-195.

12. Talapin, D. V., Nelson, J.H., Shevchenko, E.V., Aloni, S., Sadtler, B., Alivisatos, A.P., Seeded Growth of Highly Luminescent CdSe/CdS Nanoheterostructures with Rod and Tetrapod Morphologies. *Nano Lett.* **2007,** *7*, 2951-2959.

13. Nasilowski, M.; Mahler, B.; Lhuillier, E.; Ithurria, S.; Dubertret, B., Two-Dimensional Colloidal Nanocrystals. *Chem. Rev.* **2016,** *116*, 10934-10982.

14. Ithurria, S.; Talapin, D. V., Colloidal Atomic Layer Deposition (c-ALD) using Self-Limiting Reactions at Nanocrystal Surface Coupled to Phase Transfer between Polar and Nonpolar Media. *J. Am. Chem. Soc.* **2012,** *134*, 18585-18590.

15. Bruchez, J. M., Moronne, M., Gin, P., Weiss, S., Alivisatos, A.P., Semiconductor Nanocrystals as Fluorescent Biological Labels. *Science* **1998,** *281*, 2013-2016.

16. Talapin, D. V.; Steckel, J., Quantum dot light-emitting devices. *MRS Bull.* **2013,** *38*, 685-695.

17. Klimov, V. I., *Nanocrystal Quantum Dots*. CRC Press; 2 edition: 2010; p 485.

18. Sahu, A.; Kang, M. S.; Kompch, A.; Notthoff, C.; Wills, A. W.; Deng, D.; Winterer, M.; Frisbie, C. D.; Norris, D. J., Electronic Impurity Doping in CdSe Nanocrystals. *Nano Lett.* **2012,** *12*, 2587-2594.

19. Lee, J. S.; Kovalenko, M. V.; Huang, J.; Chung, D. S.; Talapin, D. V., Band-like transport, high electron mobility and high photoconductivity in all-inorganic nanocrystal arrays. *Nat. Nanotechnol.* **2011,** *6*, 348-352.

20. Choi, J. H.; Fafarman, A. T.; Oh, S. J.; Ko, D. K.; Kim, D. K.; Diroll, B. T.; Muramoto, S.; Gillen, J. G.; Murray, C. B.; Kagan, C. R., Bandlike Transport in Strongly Coupled and Doped Quantum Dot Solids: A Route to High-Performance Thin-Film Electronics. *Nano Lett.* **2012,** *12*, 2631-2638.

21. Deng, Z.-X.; Li, L.; Li, Y., Novel Inorganic−Organic-Layered Structures: Crystallographic Understanding of Both Phase and Morphology Formations of One-Dimensional CdE (E = S, Se, Te) Nanorods in Ethylenediamine. *Inorg. Chem.* **2003,** *42*, 2331-2341.

22. Yao, H.-B.; Gao, M.-R.; Yu, S.-H., Small organic molecule templating synthesis of organic-inorganic hybrid materials: their nanostructures and properties. *Nanoscale* **2010,** *2*, 322-334.

23. Yuan, M.; Dirmyer, M.; Badding, J.; Sen, A.; Dahlberg, M.; Schiffer, P., Controlled Assembly of Zero-, One-, Two-, and Three-Dimensional Metal Chalcogenide Structures. *Inorg. Chem.* **2007,** *46*, 7238-7240.

24. Bronger, W.; Muller, P., Framework Structures in Metal Chalcogenides and the Characterization of Their Bonding by Magnetic-Properties. *J Less-Common Met* **1984,** *100*, 241-247.

25. Sheldrick, W. S.; Wachhold, M., Solventothermal synthesis of solid-state chalcogenidometalates. *Angew. Chem., Int. Ed.* **1997,** *36*, 207-224.

26. Scott, R. W. J.; MacLachlan, M. J.; Ozin, G. A., Synthesis of metal sulfide materials with controlled architecture. *Curr Opin Solid St M* **1999,** *4*, 113-121.

27. Pell, M. A.; Ibers, J. A., Layered ternary and quaternary metal chalcogenides. *Chem Ber-Recl* **1997,** *130*, 1-8.

28. Mitzi, D. B.; Kosbar, L. L.; Murray, C. E.; Copel, M.; Afzali, A., High-mobility ultrathin semiconducting films prepared by spin coating. *Nature* **2004,** *428*, 299-303.

29. Mitzi, D. B.; Copel, M.; Chey, S. J., Low-voltage transistor employing a high-mobility spin-coated chalcogenide semiconductor. *Adv. Mater.* **2005,** *17*, 1285.

30. Mitzi, D. B., Synthesis, structure, and thermal properties of soluble hydrazinium germanium(IV) and tin(IV) selenide salts. *Inorg. Chem.* **2005,** *44*, 3755-3761.

31. Mitzi, D. B., Polymorphic one-dimensional (N2H4)(2)ZnTe: Soluble precursors for the formation of hexagonal or cubic zinc telluride. *Inorg. Chem.* **2005,** *44*, 7078-7086.

32. Mitzi, D. B.; Copel, M.; Murray, C. E., High-mobility p-type transistor based on a spin-coated metal telluride semiconductor. *Adv. Mater.* **2006,** *18*, 2448.

33. Mitzi, D. B.; Yuan, M.; Liu, W.; Kellock, A. J.; Chey, S. J.; Deline, V.; Schrott, A. G., A High-Efficiency Solution-Deposited Thin-Film Photovoltaic Device. *Adv. Mater.* **2008,** *20*, 3657.

34. Yuan, M.; Mitzi, D. B., Solvent properties of hydrazine in the preparation of metal chalcogenide bulk materials and films. *Dalton Trans.* **2009**, 6078-6088.

35. Mitzi, D. B., Solution Processing of Chalcogenide Semiconductors via Dimensional Reduction. *Adv. Mater.* **2009,** *21*, 3141-3158.

36. Dolzhnikov, D. S.; Zhang, H.; Jang, J.; Son, J. S.; Panthani, M. G.; Shibata, T.; Chattopadhyay, S.; Talapin, D. V., Composition-matched molecular "solders" for semiconductors. *Science* **2015,** *347*, 425-428.

37. Jang, J.; Dolzhnikov, D. S.; Liu, W.; Nam, S.; Shim, M.; Talapin, D. V., Solution-Processed Transistors Using Colloidal Nanocrystals with Composition-Matched Molecular “Solders”: Approaching Single Crystal Mobility. *Nano Lett.* **2015,** *15*, 6309-6317.

38. Huang, X.; Li, J., From Single to Multiple Atomic Layers: A Unique Approach to the Systematic Tuning of Structures and Properties of Inorganic−Organic Hybrid Nanostructured Semiconductors. *J. Am. Chem. Soc.* **2007,** *129*, 3157-3162.

39. Huang, X. Y.; Li, J.; Zhang, Y.; Mascarenhas, A., From 1D chain to 3D network: Tuning hybrid II-VI nanostructures and their optical properties. *J. Am. Chem. Soc.* **2003,** *125*, 7049-7055.

40. Calvin, S., *XAFS for Everyone*. Taylor & Francis: 2013.

41. Ravel, B.; Newville, M., ATHENA, ARTEMIS, HEPHAESTUS: data analysis for X-ray absorption spectroscopy using IFEFFIT. *J Synchrotron Radiat* **2005,** *12*, 537-541.

42. Beecher, A. N.; Yang, X. H.; Palmer, J. H.; LaGrassa, A. L.; Juhas, P.; Billinge, S. J. L.; Owen, J. S., Atomic Structures and Gram Scale Synthesis of Three Tetrahedral Quantum Dots. *J. Am. Chem. Soc.* **2014,** *136*, 10645-10653.

43. Wang, Y. Y.; Liu, Y. H.; Zhang, Y.; Kowalski, P. J.; Rohrs, H. W.; Buhro, W. E., Preparation of Primary Amine Derivatives of the Magic-Size Nanocluster (CdSe)(13). *Inorg. Chem.* **2013,** *52*, 2933-2938.

44. Evans, C. M.; Love, A. M.; Weiss, E. A., Surfactant-Controlled Polymerization of Semiconductor Clusters to Quantum Dots through Competing Step-Growth and Living Chain-Growth Mechanisms. *J. Am. Chem. Soc.* **2012,** *134*, 17298-17305.

45. Cossairt, B. M.; Owen, J. S., CdSe Clusters: At the Interface of Small Molecules and Quantum Dots. *Chem. Mater.* **2011,** *23*, 3114-3119.

46. Kovalenko, M. V.; Scheele, M.; Talapin, D. V., Colloidal Nanocrystals with Molecular Metal Chalcogenide Surface Ligands. *Science* **2009,** *324*, 1417-1420.

47. Sheldrick, G. M., Crystal structure refinement with SHELXL. *Acta Crystallogr C* **2015,** *71*, 3-8.

48. Dolomanov, O. V.; Bourhis, L. J.; Gildea, R. J.; Howard, J. A. K.; Puschmann, H., OLEX2: a complete structure solution, refinement and analysis program. *Journal of Applied Crystallography* **2009,** *42*, 339-341.

49. Sheldrick, G., A short history of SHELX. *Acta Crystallographica Section A* **2008,** *64*, 112-122.

3. New forms of CdSe and CdTe: mesostructures and gels

3.1. Introduction to mesostructured semiconductors and chalcogels.

Functional materials with micro- or nanoscale voids display improved performance for applications in sensing,[2] sorption,[3] and energy conversion and storage.[4-5] The increased surface area allows for more interfacial contact between the active material and an analyte of interest or electrolyte media. Functional porous materials can be formed either through decoration of a porous substrate with active species, such as sensors[2] or photoactive materials,[6] or manipulation of an active species (*e.g.* semiconductor[7]) to form a continuous porous structure. Decoration of a preformed substrate allows a greater range of structure design but a porous structure composed of only active material may improve the efficiency. Such functional porous structures can be formed through surfactant templating,[4] material gelation,[8] or other methods.

Surfactant-templated mesoporous oxides have been widely utilized for their high surface area and their ease of surface functionalization. In these materials, organic surfactants are used as a removable soft template for inorganic materials to produce solids with monodisperse mesoscale (2-50 nm) pores in an organized array.[9] Functionalized mesoporous oxides display high performance in many applications, including heterogeneous catalysts, solar cell absorber layers, and cathode and anode materials for Li ion batteries.[9-11] The extension of soft templating techniques to non-oxide II-VI semiconductors will yield novel functional materials. Previous reports have demonstrated the patterning of chalcogenidometallates (*e.g.* $Sn_2S_6^{4-}$, $SnTe_4^{4-}$, and $Ge_4S_{10}^{4-}$) around columnar micelles and crosslinking of the resulting structure with transition

metal ions (Pt^{2+}, Pt^{4+}, Cd^{2+}, Zn^{2+}, or Mn^{2+}).[12-14] These reports suggest that the oligomerization of chalcogenidometallate species through interaction with metal ions is necessary for the mesostructure formation to be entropically allowed. Here, we show that the extended chains of $(Cd_2Se_3)_n^{2n-}$ or $(CdTe_2)_n^{2n-}$ favorably self-assemble with positively charged micelles without the inclusion of a foreign metal ion.

Mesoporous materials with a disordered pore network can be formed by gelation of an active material to form an open structure. Several works have shown that chalcogenidometallates ($Sn_2S_6^{4-}$, $Sn_2Se_6^{4-}$, $Ge_4S_{10}^{4-}$, *etc.*) can be crosslinked with metal ions to create semiconducting mesoporous gel structures.[15-16] This gelation process creates a material with a network of thin walls with voids filled by solvent. The solvent can be removed while retaining the open structure by supercritical drying with CO_2. The resulting high surface area semiconducting aerogels have been used as heavy metal sorbents[16] and photochemical catalysts for various reactions.[17-20] The synthesis of chalcogels based on II-VI semiconductors has not previously been achieved.

Here, we demonstrate the use of chalcogenidocadmates, $Na_2Cd_2Se_3$ and Na_2CdTe_2, to form novel II-VI materials. By combining solutions of a chalcogenidocadmate and a templating surfactant, we create ordered mesostructures of CdSe and CdTe. To our knowledge, this is the first example of surfactant-templated CdSe and CdTe from molecular precursors. Additionally, we synthesize a viscous, gel-like form of stoichiometric CdSe by crosslinking $(Cd_2Se_3)_n^{2n-}$ molecular wires with Cd^{2+} in a hydrazine solution. This CdSe gel serves as a solution-processed precursor for polycrystalline CdSe. Annealed films of CdSe gel can be used as the active layer in visible photoconductors and field-effect transistors.

3.2. Templated synthesis of mesostructured II-VI semiconductors.

The facile interchange of charge-balancing cations in solution allows for templating of chalcogenidocadmate ions using long-chain alkylammonium surfactants to form unprecedented mesoporous CdSe and CdTe structures (Figure 3.1). An ordered CdSe mesostructure can be formed by coprecipitation of *N*-eicosane-*N*,*N*-di(2-hydroxyethyl)-*N*-methyl ammonium bromide (EDHEMAB) and $(Cd_2Se_3)_n^{2n-}$ from hydrazine. When a colorless solution of $Na_2Cd_2Se_3$ in hydrazine is added to an EDHEMAB solution in hydrazine at 80 °C, the mixture immediately turns cloudy. After stirring for three hours at 40 °C, the precipitate is collected by centrifugation and washed with excess ethanol and hexane to yield a yellow powder.

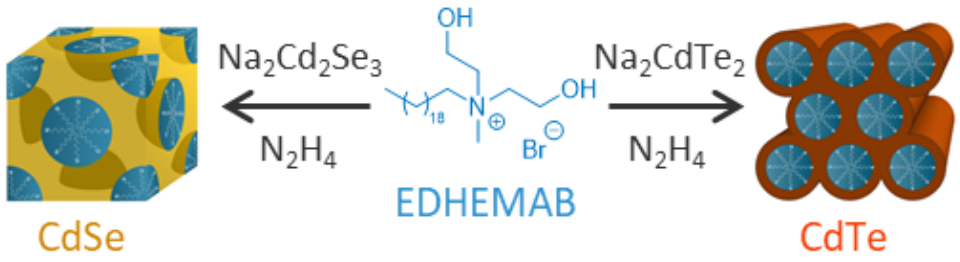

Figure 3.1. Schematic for the synthesis of mesostructured II-VI materials.
This schematic depicts the soft templating of chalcogenidocadmates ($Na_2Cd_2Se_3$ and Na_2CdTe_2) by a surfactant (EDHEMAB) to form a mesostructured organic-inorganic hybrid.

The organization of the resulting hybrid organic-inorganic mesostructure was explored with transmission electron microscopy (TEM) and small angle x-ray scattering (SAXS). TEM images show large areas of mesostructure with surfactant-filled pores of about 2 nm diameter (Figure 3.2a). It is difficult to determine the organization of the pores by TEM, likely due to layering of multiple domains of mesostructured CdSe. Moreover, TEM only allows for characterization of a small fraction of the products on the periphery of large templated domains. Small-angle x-ray scattering (SAXS) at the Advanced Photon Source at Argonne National Lab

was used to probe the mesoscale order of a large powder sample without selection bias. SAXS confirms a mesostructure with long-range order of the pores and indicates a face-centered cubic phase of spherical surfactant micelles surrounded by metal chalcogenide (Figure 3.2b). Although hexagonal phases of columnar micelles are most often achieved with surfactant templating, the formation of cubic phases has been seen for both metal oxides[21] and chalcogenides,[12, 14] and it has been suggested that cubic phases are more desirable because guest species can access the porous network from all directions. It is possible that the relatively low reaction temperature or the reaction of selenocadmate with the surfactant and resulting reduction of templating species yields spherical rather than columnar micelles.

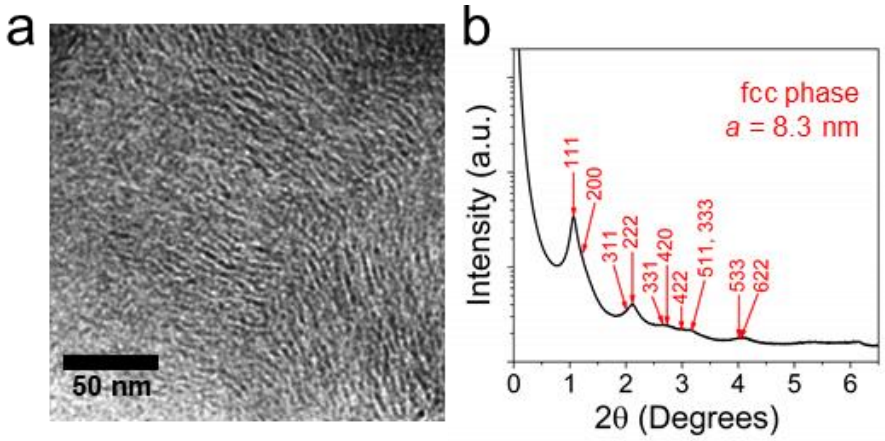

Figure 3.2. Structural characterization of mesostructured CdSe.
(a) A TEM image of mesostructured CdSe shows areas of metal chalcogenide (high contrast) separated by surfactant-filled pores (low contrast). *(b)* The SAXS pattern for mesostructured CdSe shows long-range order that can be indexed to an fcc lattice.

Inductively-coupled plasma optical emission spectroscopy (ICP-OES) of the mesostructured CdSe powder indicates that the material contains equimolar amounts of Cd and Se. The excess selenium in the $Na_2Cd_2Se_3$ precursor likely reacts with the surfactant to yield CdSe and soluble byproducts that are removed during washing. The dealkylation of alkylammonium salts by chalcogenides is well known and could easily occur at the elevated

temperature of the template solution to release a soluble organoselenium species.[58] Although ICP-OES indicates stoichiometric CdSe, powder x-ray diffraction shows only broad peaks at higher angles (Figure 3.3), suggesting that the pore walls are either amorphous or contain very small crystallites. This amorphous material crystallizes upon mild annealing to form wurtzite phase CdSe. The Raman spectrum of the mesoporous powder exhibits peaks at ~202 cm^{-1} and ~404 cm^{-1} corresponding to the longitudinal optical (LO) phonon mode of CdSe lattice and its first overtone (Figure 3.4a). For comparison, the Raman spectrum of $Na_2Cd_2Se_3$ is qualitatively different from that of CdSe (Figure 3.4b), further confirming that the mesostructured material contains a CdSe phase formed from templated $(Cd_2Se_3)_n^{2n-}$ ions under our reaction conditions. Thermogravimetric analysis (TGA) indicates that the pores are filled with surfactant which is removed at elevated temperature (Figure 3.5). The diffuse reflectance spectrum of a film of mesostructured CdSe was measured with an integrating sphere and converted to absorbance using the Kubelka-Munk equation (Figure 3.6). This measurement indicates a bandgap of ~2.5 eV, which is reasonable for strongly quantum-confined CdSe.[22] The photoluminescence of a film of mesostructured CdSe excited at 3.26 eV was measured, and it agrees with the bandgap measured by diffuse reflectance.

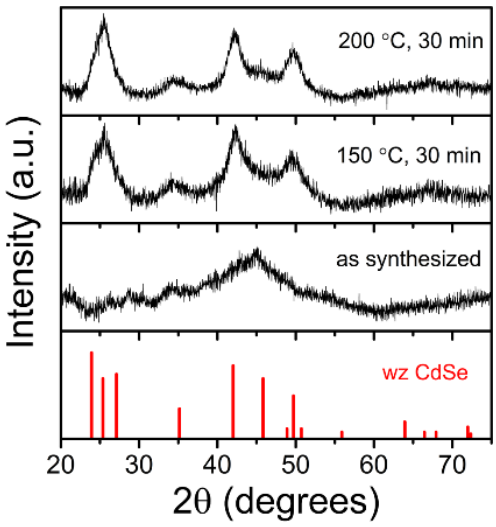

Figure 3.3. Powder XRD patterns for mesostructured CdSe before and after mild annealing. As synthesized, mesostructured CdSe is amorphous and shows no well-defined peaks in the XRD pattern. Upon annealing at 150 or 200 °C, the material crystallizes to form wurtzite phase nanocrystalline CdSe.

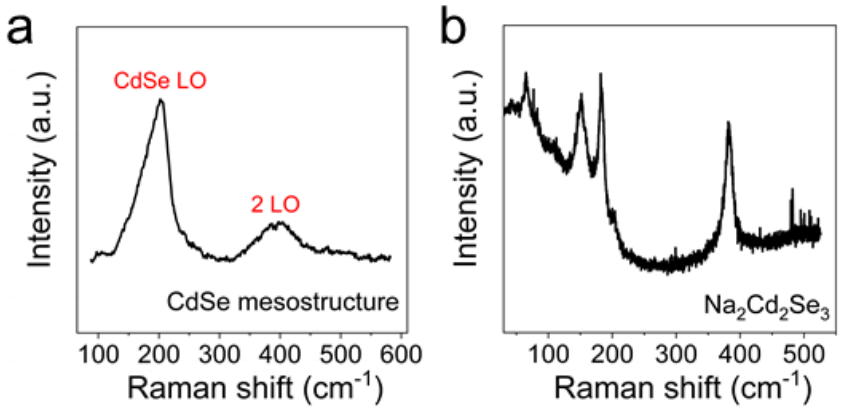

Figure 3.4. Raman spectra for mesostructured CdSe and $Na_2Cd_2Se_3$.
(a) The Raman spectrum for the CdSe mesostructure shows broad peaks corresponding to characteristic phonon modes for CdSe, *(b)* while the Raman spectrum for $Na_2Cd_2Se_3$ shows unique peaks, confirming that the material has transformed during the templating process.

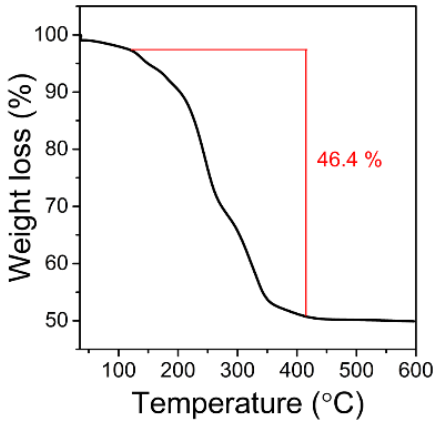

Figure 3.5. TGA data for mesostructured CdSe.
Thermogravimetric analysis (TGA) data for mesostructured CdSe shows dramatic weight loss above 150 °C, corresponding to loss of the templating surfactant.

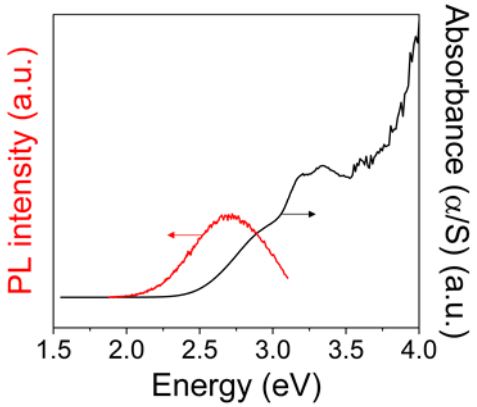

Figure 3.6. Optical characterization of mesostructured CdSe.
The absorbance (converted from diffuse reflectance using the Kubelka-Munk equation) and photoluminescence of a mesostructured CdSe film indicate a band gap of ~2.5 eV.

This technique for creating surfactant-templated metal chalcogenides can be extended to form mesostructured CdTe. When solutions of Na_2CdTe_2 in hydrazine and EDHEMAB in formamide are combined at 80 °C, a yellow-orange precipitate forms immediately and the solution turns green due to decomposition of tellurocadmate to yield polytelluride and CdTe. The resulting suspension is stirred at room temperature for an hour, and a deep red-orange powder is isolated by centrifugation and washed with ethanol and hexane to remove the excess surfactant and tellurium. TEM reveals a well-ordered CdTe mesostructure templated around columnar

micelles (Figure 3.7a,b). Though XRD shows no sharp peaks at high 2θ angles (Figure 3.7c), the identity of the metal chalcogenide was confirmed with Raman spectroscopy (Figure 3.7d). The lattice fringes of small crystallites can be seen in the high-resolution TEM image (Figure 3.7b), likely due to the crystallization of amorphous CdTe under the electron beam. A natural follow-up to these syntheses is the removal of the templating surfactant or the use of a semiconducting templating agent to create new functional materials.[59]

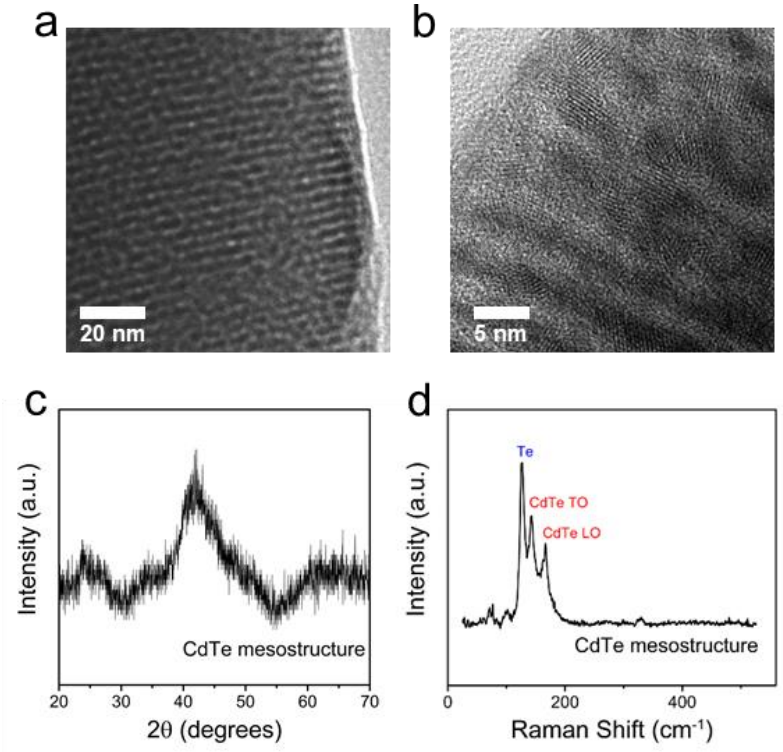

Figure 3.7. Characterization of mesostructured CdTe.
(a,b) TEM images of mesostructured CdTe show evidence of an ordered array of CdTe (high contrast) and surfactant-filled pores (low contrast). *(c)* Powder XRD pattern for mesostructured CdTe shows no well-defined peaks, suggesting the structure is amorphous. *(d)* Raman shows peaks corresponding to CdTe and Te. The extent of Te contamination is hard to discern with Raman due to the high scattering cross section of tellurium.

3.3. Synthesis and characterization of gel-like stoichiometric $CdSe \cdot xN_2H_4$.

Unlike the facile replacement of Na^+ by organic cations, the addition of Cd^{2+} to $(Cd_2Se_3)_n^{2n-}$ induces significant changes in the chalcogenidometallate structure and properties,

creating a novel gel-like form of CdSe. When $Na_2Cd_2Se_3$ is combined with $CdCl_2$ in hydrazine, an off-white suspension forms (Figure 3.8), based on the following equation:

$$Na_2Cd_2Se_3 + CdCl_2 \xrightarrow{N_2H_4} 3\ CdSe \cdot x\ N_2H_{4\ (gel)} + 2\ NaCl$$

Brief centrifugation yields a viscous gel-like material and the soluble NaCl byproduct is removed in the supernatant. Inductively-coupled plasma optical emission spectroscopy (ICP-OES) confirms that this gel-like species contains equimolar amounts of Cd and Se and negligible Na. This CdSe gel is related to a class of chalcogels created by crosslinking chalcogenidometallates (*e.g.* $[Sn_2S_6]^{4-}$ and $[Ge_4S_{10}]^{4-}$) with transition metal ions; however chalcogels typically use foreign metal ions (*e.g.* Pt^{2+}) to control the crosslinking metathesis and produce a stable gel.[15-16] Stoichiometric CdSe gel is attractive as a precursor for semiconductor materials because its only contaminant is hydrazine, which readily evaporates during annealing to leave a chemically pure CdSe phase, and its high viscosity may be convenient for doctor blading and other deposition techniques.

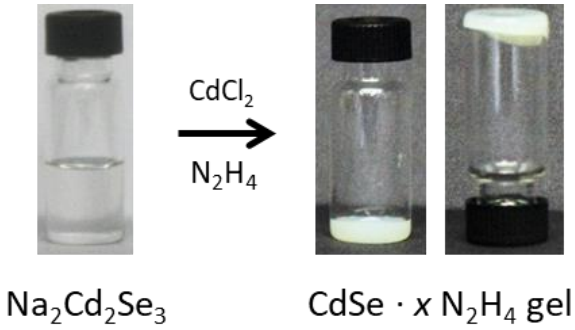

Figure 3.8. CdSe gel synthesis.
Photographs showing the synthesis of CdSe gel and its high viscosity**.**

Raman spectroscopy, powder x-ray diffraction (XRD), and extended x-ray absorption fine structure (EXAFS) were used to examine the structure of the CdSe gel. The Raman spectrum of the CdSe gel displays a peak at 140 cm^{-1} and a broad feature below 250 cm^{-1} (Figure

3.9); these features are distinct from those of both bulk CdSe and $Na_2Cd_2Se_3$, indicating different chemical bonding in these compounds. The appearance of peaks below the energy of the phonon modes of the parent compound has been observed for low-dimensional metal chalcogenides,[23] suggesting that the CdSe gel may have isolated fragments of a tetrahedrally coordinated CdSe lattice.

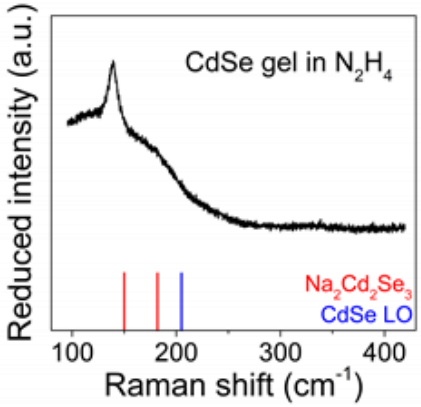

Figure 3.9. Raman spectrum of CdSe gel.
The Raman spectrum of CdSe gel has a sharp feature at 140 cm^{-1}, which does not correspond to the features of $Na_2Cd_2Se_3$ or CdSe.

The structure of this stoichiometric CdSe gel was explored with powder x-ray diffraction (XRD). Total removal of the hydrazine solvent leads to structural collapse of the gel material, yielding a yellow to orange powder that cannot be resuspended in hydrazine, so XRD measurements were taken on suspensions of the gel in hydrazine held in sealed glass capillaries. The suspension is largely amorphous and exhibits only weak scattering; however, rings can be observed in two-dimensional powder patterns (Figure 3.10). Immediately after synthesis, the diffraction pattern exhibits one peak at ~8° 2θ angle, but the structure evolves over time, developing peaks at higher angles as the initial peak wanes in intensity. The structure stabilizes after 24 hours, exhibiting two diffraction peaks at ~10.5° and ~27° 2θ, and this structure remains stable in a sealed nitrogen atmosphere (no observed changes up to 60 days).

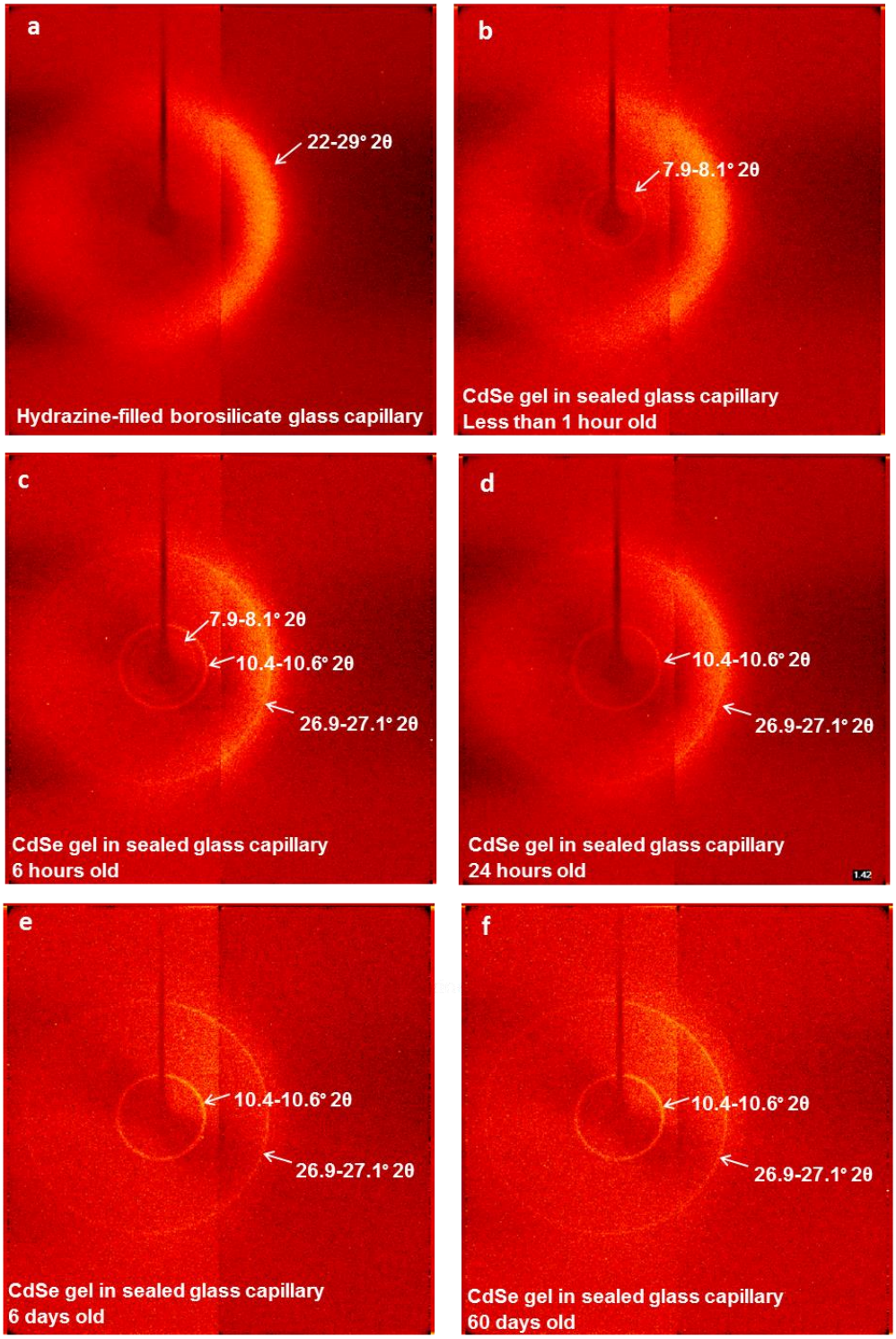

Figure 3.10. Time evolution of CdSe gel XRD pattern.

2-dimensional powder x-ray diffraction patterns of glass capillaries containing *(a)* hydrazine and *(b-e)* suspensions of CdSe gel in hydrazine at different time points, showing the structure evolution over time.

The poor crystallinity of the CdSe gel limits the quality of attainable powder data, so direct structure solution followed by Rietveld refinement is not possible. However, we noted that the peak positions and intensities are similar to those previously seen for layered metal chalcogenides with bridging diamines. Powder patterns for CdS, CdSe, and CdTe layered structures with linking amines have the most intense peak at a low angle; 10.6° 2θ is reported for layered CdSe slabs linked by ethylenediamine[24] and 8.6° 2θ is reported for CdSe slabs linked by 1,3-propanediamine.[23] These intense peaks correspond to the inter-slab spacing, with larger distances yielding diffraction at smaller angles. Thus, the observed peaks in CdSe gel at low angles may suggest that layered slabs of a 2-dimensional CdSe species have formed. The evolution of the diffraction peaks with time may represent the formation of different layered CdSe structures with variable distance between slabs; we expect that hydrazine fills the space between layers and is expelled as the structure evolves as schematically outlined in Figure 3.11.

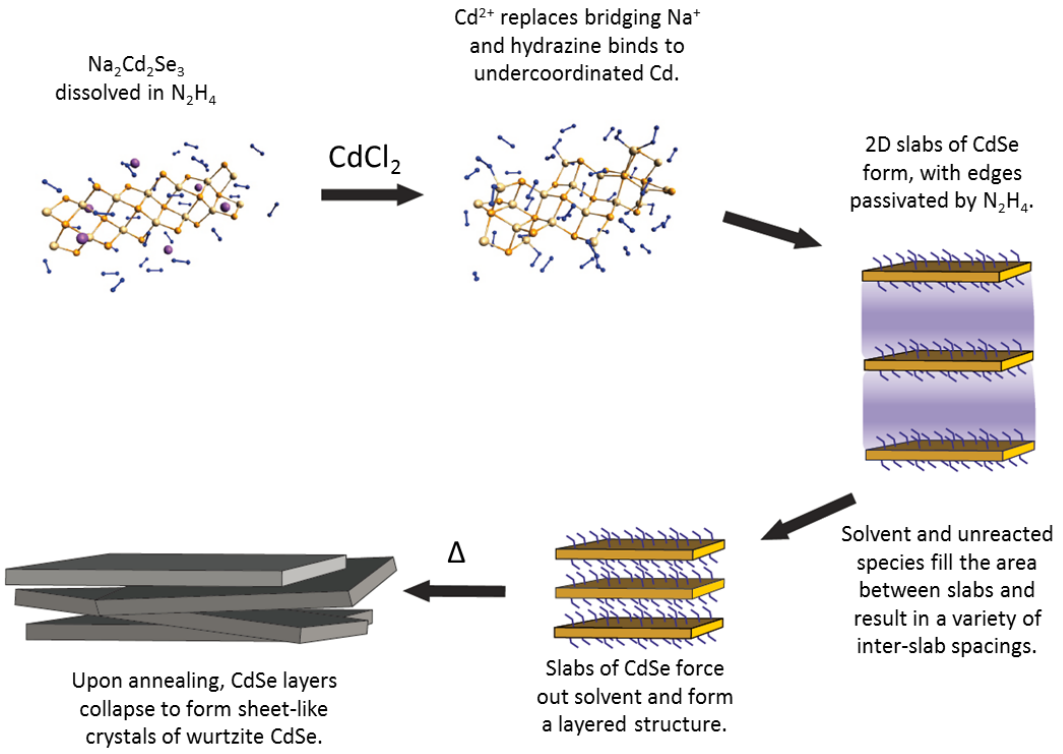

Figure 3.11. Description of CdSe gel formation and evolution with time.
Proposed scheme for the formation of CdSe gel and resulting sheets of crystalline CdSe upon annealing.

Experimental evidence supports the formation of sheet-like structures and hydrazine coordination in the CdSe gel. A scanning electron microscopy (SEM) image of dried CdSe gel shows micron-sized globules with an internal structure made of stacked layers (Figure 3.12a), supporting the above hypothesis. Additionally, thermogravimetric analysis suggests that the gel composition is approximately 4 CdSe · 3 N_2H_4; two loosely bound hydrazine molecules are lost at ~100 °C and a chemically bound hydrazine is lost at ~200 °C to yield pure CdSe (Figure 3.12b).

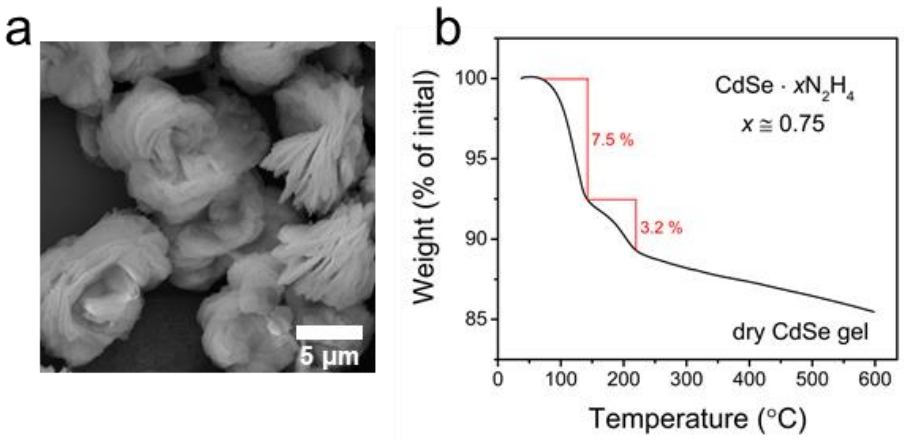

Figure 3.12. Characterization of dried CdSe gel.
(a) An SEM image of dried CdSe gel shows aggregations of thin sheets. *(b)* Thermogravimetric analysis of CdSe gel from 35 °C to 600 °C at 3 °C/min under flowing nitrogen indicates the loss of ~0.75 N_2H_4 molecules for each CdSe unit.

Extended x-ray absorption fine structure (EXAFS) measurements taken on the CdSe gel suspension in hydrazine further support the proposed structure model (see section 2.4 for a more detailed EXAFS discussion). The amplitude of the Fourier-transformed absorption probability of the gel is higher than that of the selenocadmate starting material and more closely mimics bulk CdSe, suggesting higher coordination numbers for Cd and Se (Figure 3.13).

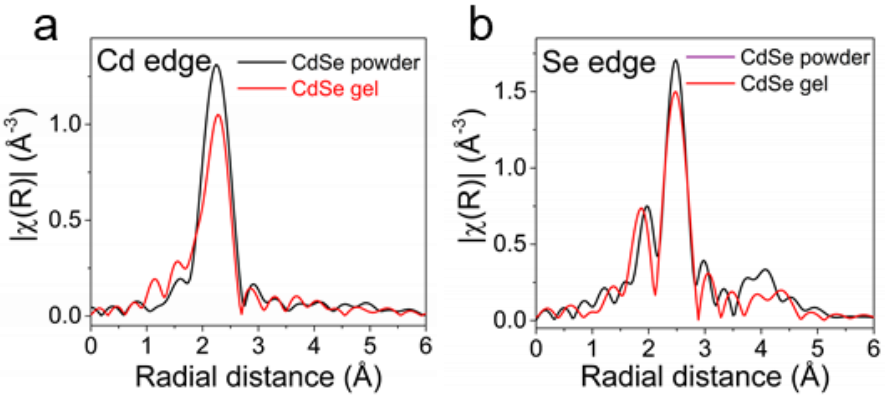

Figure 3.13. EXAFS data for CdSe gel.
The Fourier-transformed absorption probability of the EXAFS data from the *(a)* Cd and *(b)* Se K-edges suggests that the CdSe gel has a structure similar to that of bulk CdSe.

Fitting of the EXAFS data (Table 3.1, Figure 3.14) yields coordination numbers of about 3.5 ± 0.6 for both Cd and Se. The chains of $(Cd_2Se_3)_n^{2n-}$ have crosslinked through addition of Cd^{2+}, creating many new Cd-Se bonds and a structure that approaches that of bulk CdSe. Additionally, the Cd edge is well-modeled with the inclusion of a nitrogen shell, suggesting that cadmium is directly coordinated to hydrazine. It is likely that the edges of the slabs have under-coordinated cadmium that is bound to hydrazine. This direct coordination of amines to cadmium has been shown to stabilize a variety of low-dimensional metal chalcogenide species.[24-26] Hydrazine coordination supports the separation of the chains and formation of an open gel structure, and the replacement of these Cd-N bonds with Cd-Se likely leads to the gel collapse and the formation of sphalerite or wurtzite CdSe. Indeed, upon annealing the gel collapses to form flakes of a CdSe phase as shown schematically in Figure 3.11.

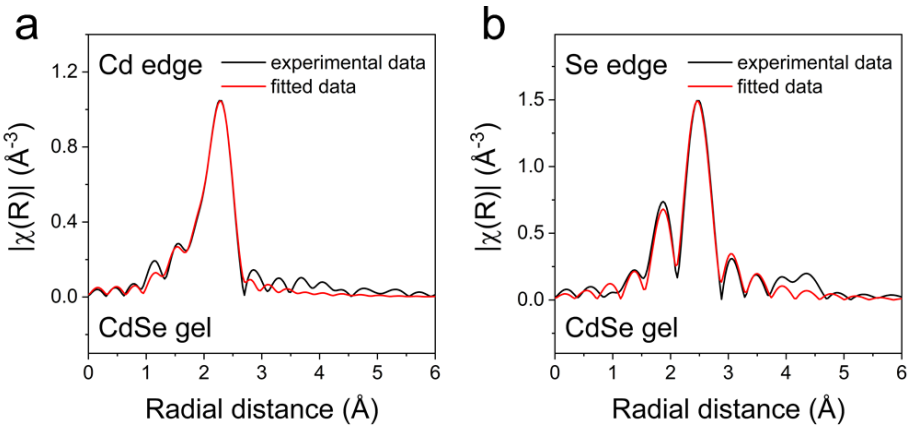

Figure 3.14. Fits to EXAFS data for CdSe gel.
Magnitude of the Fourier-transformed EXAFS experimental and fitted data for CdSe gel in N_2H_4 at the *(a)* Cd and *(b)* Se K-edges.

Table 3.1. EXAFS fitting parameters for bulk CdSe and CdSe gel.

		Path	Bond length (Å)	Coordination number	E_0	Debye-Waller factor	R
Cd K-edge (26.711 keV) S_0^2 = 1.05	**CdSe powder** R: 1.6 – 3.5 k: 4 – 12.5	Cd-Se_1	2.61 ± 0.02	3 (set)	5 ± 2	0.004 ± 0.002	0.006
		Cd-Se_2	2.75 ± 0.04	1 (set)		0.003 ± 0.006	
	CdSe gel in N_2H_4 R: 1 – 3.5 k: 2.4 – 12	Cd-Se	2.617 ± 0.006	3.5 ± 0.6	3 ± 1	0.006 ± 0.001	0.017
		Cd-N	2.36 ± 0.03	1.6 ± 0.7		0.01 ± 0.01	
Se K-edge (12.658 keV) S_0^2 = 1.00	**CdSe powder** R: 1.6 – 4.5 k: 3.2 – 11.9	Se-Cd_1	2.61 ± 0.02	3 (set)	1.4 ± 0.8	0.009 ± 0.004	0.010
		Se-Cd_2	2.63 ± 0.02	1 (set)		0.002 ± 0.001	
		Se-Se	4.31 ± 0.02	12 (set)		0.020 ± 0.003	
	CdSe gel in N_2H_4 R: 1.3 – 3.8 k: 3 – 10.5	Se-Cd	2.602 ± 0.006	3.6 ± 0.3	0.4 ± 0.7	0.0055 ± 0.0008	0.019

3.4. Applications of polycrystalline CdSe films prepared from CdSe gel.

Suspensions of CdSe gel in hydrazine can be drop-cast onto hydrophilic glass or silicon to form films. Upon annealing, the gel loses coordinated hydrazine and decomposes to wurtzite CdSe; XRD shows that wurtzite CdSe forms as low as 200 °C and grows into larger grains at elevated temperature (Figure 3.15a). The chemical and phase purity of the obtained CdSe is confirmed by Raman spectroscopy (Figure 3.15b). An SEM image of a film annealed at 350 °C reveals that rather than forming a continuous layer, the gel has formed into layered sheets of crystalline CdSe (Figure 3.15c). Previous works demonstrate that bound amines can template low-dimensional metal chalcogenide precursors to form rod- or sheet-like crystals,[24-25] and the bound hydrazine in the CdSe gel likely induces the formation of sheet-like crystals rather than three-dimensional grains. The porous nature of this film may allow for the intercalation of a second material to create composites with interesting properties.

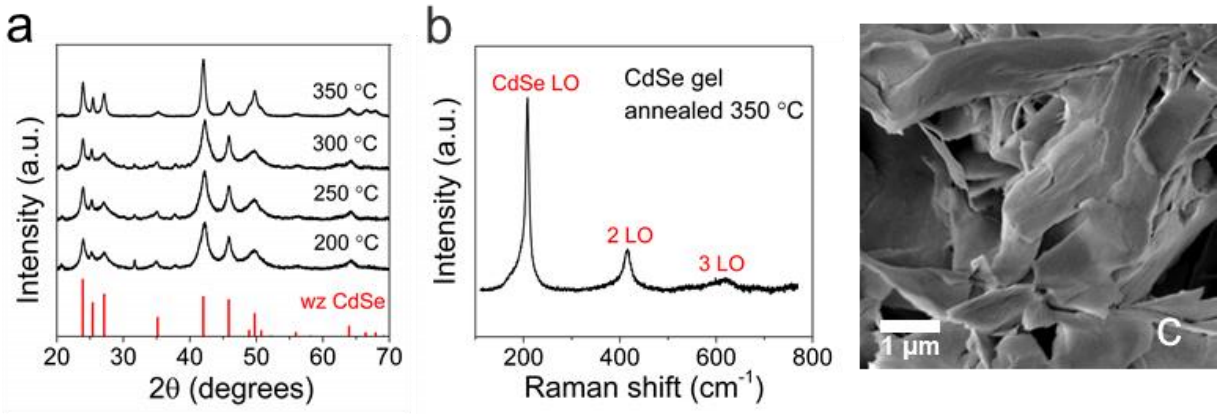

Figure 3.15. Characterization of annealed CdSe gel.
(a) XRD patterns for CdSe gel films annealed at various temperatures for 30 minutes under nitrogen with reference peaks shown for wurtzite CdSe. *(b)* Raman spectrum of annealed CdSe gel shows peaks characteristic of bulk CdSe. *(c)* An SEM image of CdSe gel annealed at 350 °C displays sheet-like grains of CdSe.

The photoconductivity of an annealed gel film was measured to determine the electronic performance of the material. Figure 3.16 shows the enhanced photocurrent through the gel film

when illuminated with a 405 nm laser. The ~60-fold increase in conductivity upon illumination suggests that the CdSe gel film is not degenerately doped (Figure 3.16a). Moreover, the measured conductivity across a large channel (~2 mm) suggests that there is a continuous path for electrons, although the film consists of two-dimensional sheets (Figure 3.15c). As prepared, the CdSe gel film shows a rather slow photoresponse (Figure 3.16c), which improves significantly with further washing of the CdSe gel material to remove byproducts (Figure 3.16d). This improvement is likely related to removing excess Na^+, Cd^{2+}, and Cl^- from the material. However, the magnitude of the conductivity change upon illumination decreases with this additional washing step, which can be attributed to the overall higher conductivity and increased doping of the film after washing.

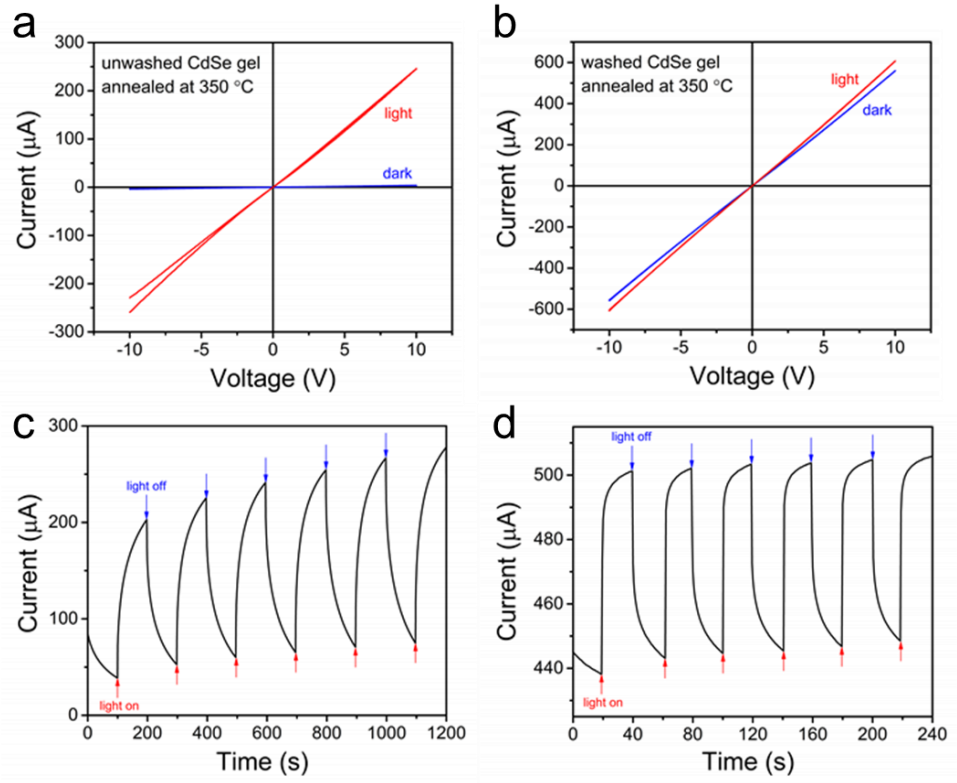

Figure 3.16. Photoconductivity of annealed CdSe gel.
Photoconductivity measurements for annealed films of *(a,c)* unwashed and *(b,d)* washed CdSe gel. *(a,b)* Current-voltage sweeps from -10 V to 10 V were measured in the dark and under the illumination of a 405 nm laser. *(c,d)* The current change as a function of time was measured at 5V as the 405 nm laser was turned on and off.

Further electronic characterization was performed by measuring a field-effect transistor (FET) with an annealed CdSe gel channel. The as-synthesized CdSe gel could not be used to make FETs because the drop-cast film is too thick to effectively gate, and the gel does not form a uniform layer when spin-coated. Instead, we spin-coated a thin layer of $Na_2Cd_2Se_3$ onto a heavily doped silicon substrate with a 300 nm SiO_2 gate layer and soaked the resulting film in a $CdCl_2$ solution in methanol. We thus formed a thin layer of CdSe gel on the substrate and annealed the film at 250 °C for 30 minutes to form polycrystalline CdSe. The electron mobility of the annealed gel film was measured with a standard top-contact bottom-gate FET geometry (Figure 3.17).

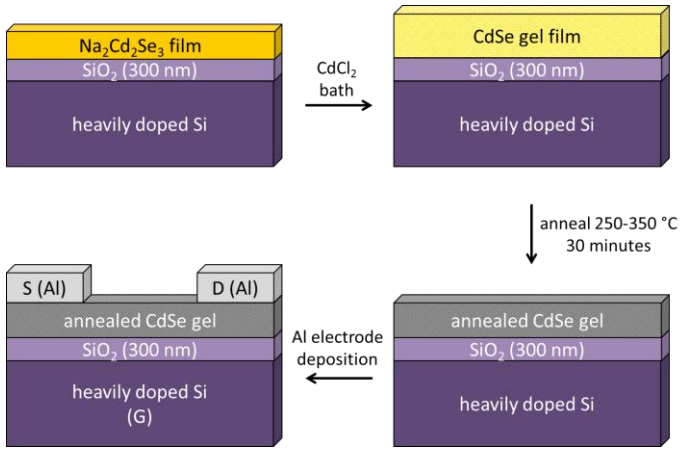

Figure 3.17. Fabrication of an FET device with CdSe gel.
A film of CdSe gel for FET characterization was formed by deposition of $Na_2Cd_2Se_3$ and on-film gel formation by treatment with $CdCl_2$. The film was then annealed at elevated temperature in an inert atmosphere for 30 minutes. Aluminum contacts (100 nm thick) were thermally evaporated onto the film through a shadow mask (channel length: 50 µm, channel width: 1500 µm).

The output and transfer characteristics of the CdSe gel FET (Figure 3.18) indicate a clear gating effect with n-type operation and an extracted linear range electron mobility of 2.6 $cm^2V^{-1}s^{-1}$. The large negative bias required to deplete the channel indicates n-type doping in the FET channel. Similar FET measurements for gel films annealed at higher temperature show increased

off-currents and a further increase in the zero-gate electron concentration in the channel (Figure 3.19).

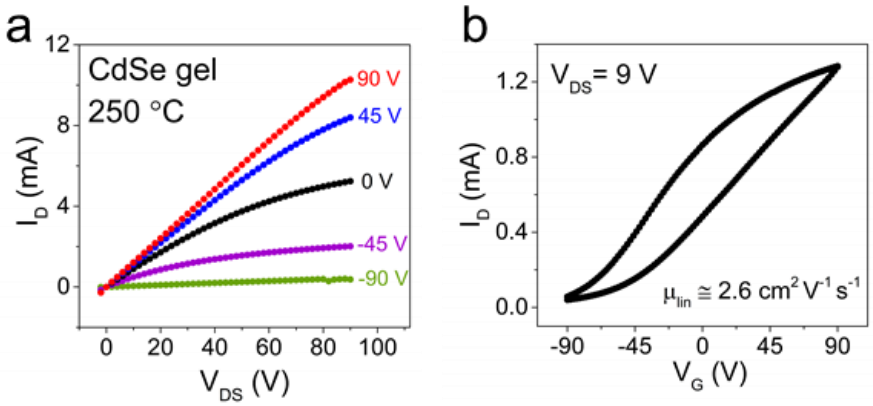

Figure 3.18. FET characteristics for a CdSe gel film annealed at 250 °C.
(a) Output and *(b)* transfer characteristics for an FET with a channel made of a CdSe gel layer annealed at 250 °C.

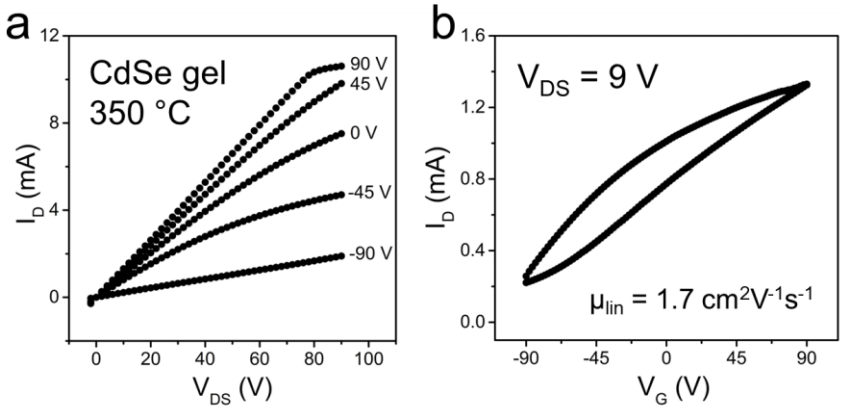

Figure 3.19. FET characteristics for a CdSe gel film annealed at 350 °C.
(a) Output and *(b)* transfer characteristics for an FET with a channel made of a CdSe gel layer annealed at 350 °C.

To explore the origin of the observed n-type doping, we fabricated FETs with channels made of hydrazinium selenocadmate that were not treated with the gel-forming $CdCl_2$ solution and thus not containing Cl^-. The FET transfer curves showed a substantially lower n-type doping level resulting in FET threshold voltages, V_{th}, shifted from about -60 V (FET operates in

depletion mode) in devices made of CdSe gel to about +40 V (FET operates in accumulation mode) in devices made of hydrazinium selenocadmate (Figure 3.20). Thus, the room-temperature cross-linking of selenocadmate by $CdCl_2$ seems to affect transport in annealed films primarily by altering the doping level, presumably by thermally activated diffusion of Cl^- ions to substitutional lattice sites where they act as the donor species. The use of other Cd^{2+} salts may provide a convenient way to control the doping level and carrier mobility in II-VI materials prepared from the gel precursors.

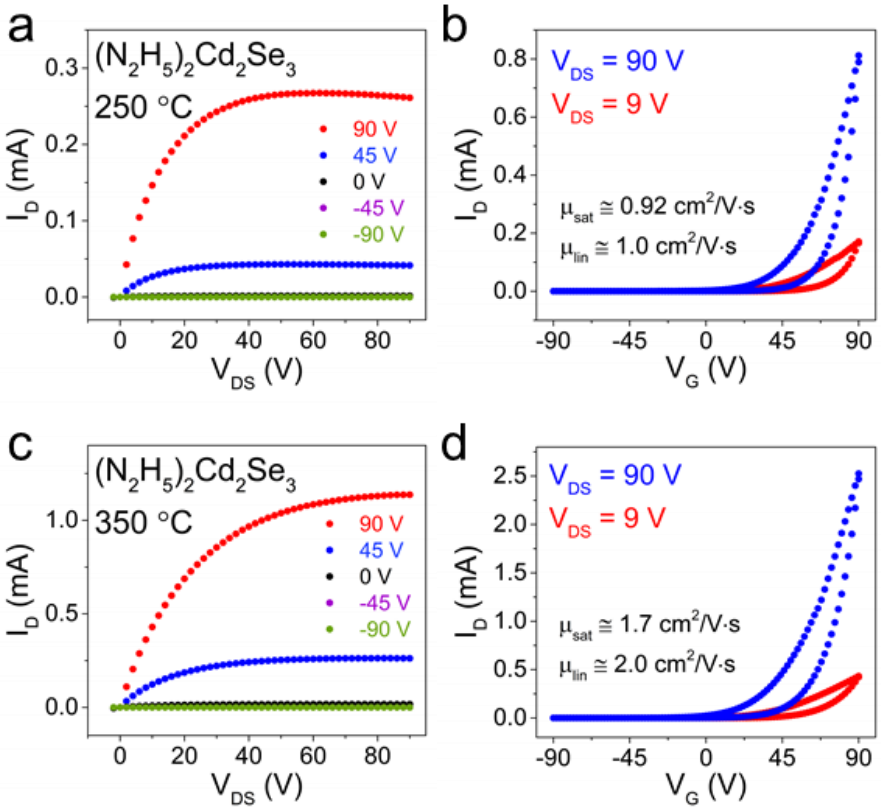

Figure 3.20. FET characteristics for annealed films of $(N_2H_5)_2Cd_2Se_3$.
(a,c) Output and *(b,d)* transfer characteristics for films of $(N_2H_5)_2Cd_2Se_3$ annealed at *(a,b)* 250 °C and *(c,d)* 350 °C.

The values of electron mobility measured for FETs with channels made of annealed CdSe gel are comparable to many other nanocrystalline solution-deposited semiconductors,[27-30] but

considerably lower than the mobilities observed for spin-coated layers of CdSe nanoparticles linked with selenocadmate ligands.[31-32] This difference can be explained by the fact that the field-effect mobility depends primarily on the quality of the interface between the semiconductor channel and the gate dielectric. Since all charge transport occurs within an accumulation layer only a few nanometers thick, high-mobility FETs use thin continuous semiconductor layers; however, the morphology of our "fluffy" CdSe gel is not optimal for high FET mobility. Instead, the open-framework CdSe chains, gels, and mesoporous structures are naturally suitable for building nanoscale composites, soldering semiconductor grains, and utilizing inorganic semiconductors in other unprecedented ways.

3.5. Conclusions.

We have presented a method to form mesostructured CdSe or CdTe using a surfactant template for one-dimensional chalcogenidocadmate polyanions. The polymeric nature of the chalcogenidocadmates allows for favorable coassembly in the presence of a cationic surfactant template. Further development of these materials could yield mesoporous II-VI materials with inherent optical and electronic properties that cannot be realized in unfunctionalized oxide materials. We also demonstrated that cross-linking selenocadmate polyanions with Cd^{2+} creates a viscous CdSe gel. This solution-processable precursor for polycrystalline CdSe is composed of stoichiometric CdSe and hydrazine. This precursor may be particularly useful for creating semiconducting materials, which demand high chemical purity. Moreover, the addition of nanocrystals or micropowders of other materials to the CdSe gel may create composites with interesting properties.

3.6. Materials and methods.

All manipulations were performed in a nitrogen glove box with < 10 ppm oxygen and water levels, unless otherwise noted.

Materials. Selenium (pellet, 99.99%, Aldrich), cadmium selenide (99.99%, Aldrich), sodium hydride (dry, 95%, Aldrich), 1-bromoeicosane (≥97%, Aldrich), *N*-methyldiethanolamine (≥99%, Aldrich), tellurium (shot, 99.999%, Aldrich), cadmium telluride (99.99%, Aldrich), cadmium chloride (ultra dry, 99.996%, Alfa Aesar), acetonitrile (MeCN, anhydrous, 99.8%, Aldrich), toluene (anhydrous, 99.8%, Aldrich), chloroform ($CHCl_3$, 99.8%, Aldrich), ethyl acetate (EtOAc, anhydrous, 99.8%, Aldrich), hexane (anhydrous, 95%, Aldrich), ethanol (anhydrous, 99.5%, Aldrich), and *N*-methylformamide (NMF, 99%, Alfa Aesar) were used as received. Hydrazine (N_2H_4, anhydrous, 98%, Aldrich) was distilled under nitrogen and used in a nitrogen glove box. Formamide (FA, 99+%, Acros) was dried and stored over molecular sieves.

Synthesis of Na_2Se. 0.25 mL of a 1 M Se solution in hydrazine (deep green color) was added to 12 mg (0.5 mmol) NaH powder dropwise over the course of approximately 30 minutes. The resulting Na_2Se suspension should be colorless/pale yellow or slightly pink; if the solution is very pink, small amounts of NaH are added until no longer pink.

Synthesis of $Na_2Cd_2Se_3$. 0.25 mmol Na_2Se was combined with 96 mg (0.5 mmol) CdSe powder in 10 mL hydrazine. This mixture was stirred at room temperature until colorless and the dark solid dissolved, about 5 days. The solution was filtered through a 0.45 μm PTFE syringe filter to remove any unreacted solids. The product was isolated by adding acetonitrile as nonsolvent and

centrifuging to isolate a white solid. The solid was dissolved in hydrazine at concentrations up to ~0.05 M.

Preparation of mesostructured CdSe. *N*-eicosane-*N*,*N*-dihydroxyethyl-*N*-methyl ammonium bromide (EDHEMAB) was synthesized according to a literature procedure, where 1-bromoeicosane (7.22 g, 20 mmol) and *N*-methyldiethanolamine (2.29 mL, 20 mmol) were refluxed in EtOH for 24 hours,[33] and the resulting white solid was washed with cold EtOH and recrystallized from 1:1 $CHCl_3$:EtOAc. EDHEMAB was dried under dynamic vacuum overnight and transferred into the glove box. 1g EDHEMAB was dissolved in 12 mL N_2H_4 at 80 °C to form a clear, colorless solution, and 10 mL of 0.025 M $Na_2Cd_2Se_3$ was added dropwise, turning the solution cloudy white. This mixture was stirred at 40 °C for three hours. A white solid was isolated by centrifugation, and washing with excess ethanol and hexane yielded a yellow powder. This yellow powder could be suspended in 1:1 hexane:ethanol and drop-cast for XRD or TEM analysis.

Synthesis of Na_2Te. 2 mL of 1 M Te solution in hydrazine (2 mmol) was slowly added to 96 mg NaH powder (4 mmol). The resulting Na_2Te formed a clear yellow solution in hydrazine.

Synthesis of Na_2CdTe_2. 2 mmol Na_2Te was added to 480 mg CdTe powder (2 mmol) in 4 mL hydrazine. After approximately 2 days of stirring, all the solid dissolved, leaving the solution clear yellow. The solution was filtered with a 0.2 µm PTFE syringe filter, and the product was isolated through precipitation with acetonitrile nonsolvent and centrifugation. The solid Na_2CdTe_2 could be dissolved in hydrazine or formamide up to concentrations of ~0.5 M.

Preparation of mesostructured CdTe. 100 mg EDHEMAB was dissolved in 2 mL formamide at 80 °C. 500 µL of a 0.1 M solution of Na_2CdTe_2 in hydrazine was added dropwise at 80 °C, and a yellow-orange precipitate formed immediately, suspended in a green solution. The temperature was decreased to room temperature, and the suspension was stirred for an hour. The solid was isolated by centrifugation and washed with excess NMF, ethanol, and hexane to yield a red-orange powder.

Preparation of gel-like CdSe. 50 µL of 0.5 M $CdCl_2$ in N_2H_4 was added to 1 mL of ~0.025 M $Na_2Cd_2Se_3$ in N_2H_4 and briefly vortexed to form a cloudy white suspension. After centrifugation for 10 seconds, a white or pale yellow gel-like material was collected, and the supernatant was discarded to remove excess reactant and NaCl. The gel can be resuspended in varying amounts of hydrazine to tune its viscosity. To form films, suspensions of the gel were drop-cast on piranha-treated glass or silicon substrates, dried at room temperature, and annealed at various temperatures for 30 minutes on a hot plate.

Hydrazinium selenocadmate films for FETs. Hydrazinium selenocadmate was prepared by cation exchange of $Na_2Cd_2Se_3$ with hydrazinium-loaded cation exchange resin. The resulting $(N_2H_5)_2Cd_2Se_3$ solution in hydrazine was spin-coated onto a silicon wafer with a 300 nm thick SiO_2 gate layer and annealed at 250 °C or 350 °C for 30 minutes. Hydrazine and H_2Se evaporate during annealing to yield a CdSe phase.

Characterization.

Wide angle powder x-ray diffraction (XRD). XRD patterns were collected with a Bruker D8 diffractometer with a Cu Kα X-ray source operating at 40 kV and 40 mA. Suspensions of mesostructured CdSe or CdTe were drop cast on glass substrates and dried in air. Diffraction measurements were conducted in air at room temperature. In situ gel measurements were measured on suspensions of CdSe gel in glass capillaries sealed under nitrogen. The diffraction data for gels was measured at 293 K on a Bruker D8 VENTURE diffractometer equipped with a microfocus Cu-target X-ray tube (λ = 1.54178 Å) and PHOTON 100 CMOS detector. Sealed glass capillaries were mounted on the goniometer head and X-ray diffraction data were measured in a transmission mode.

Extended x-ray absorption fine structure (EXAFS). EXAFS measurements were conducted at the X-ray Science Division (XSD) beamlines 20-ID and 20-BM at the Advanced Photon Source, Argonne National Laboratory. Measurements were collected at the Se K edge (12,658 eV) and Cd K edge (26,711 eV) for a solution of CdSe gel in hydrazine and CdSe powder. Solution samples were measured in plastic cuvettes sealed under nitrogen and CdSe powder was prepared as a pellet diluted with BN and sealed in Kapton tape. Reference spectra for the Cd and Se edges were measured on Cd foil and Se foil, respectively. Data reduction and analysis were conducted with the Demeter suite of x-ray absorption spectroscopy software.[34]

Optical absorption. UV-vis measurements were collected with a Cary 5000 UV-Vis-NIR spectrophotometer.

Photoluminescence. Photoluminescence was measured with a FluoroMax-4 spectrofluorimeter (HORIBA Jobin Yvon).

Transmission electron microscopy (TEM). TEM images were obtained on an FEI Technai F30 microscope at 300 kV.

Small-angle x-ray scattering (SAXS). SAXS measurements were conducted at the XSD-CMS 12-ID-B beamline at the Advanced Photon Source, Argonne National Laboratory.

Thermogravimetric analysis (TGA). TGA of dry mesostructured samples was measured with a TA Instruments Q600 from 35 °C to 600 °C at a ramp rate of 5 °C/min. under flowing nitrogen (100 mL/min). Dry powders of CdSe gel were measured under the same conditions with a slower ramp rate of 3 °C/min.

Inductively coupled plasma optical emission spectroscopy (ICP-OES). Samples for ICP-OES were dissolved in concentrated nitric acid (HNO_3, ≥69.0%, TraceSELECT, for trace analysis, Aldrich) and diluted to an appropriate concentration with deionized ultra-filtered water. Measurements were taken with an Agilent 700 Series spectrometer.

Raman spectroscopy. Mesostructured CdSe and CdTe and annealed CdSe gel were prepared for Raman as drop-cast films on glass or silicon. Suspensions of CdSe gel in hydrazine and $Na_2Cd_2Se_3$ powder in acetonitrile were measured in borosilicate glass capillaries. Raman scattering was measured with a Horiba LabRamHR Evolution in backscattering geometry

excited with 633 nm or 473 nm lasers. Gratings were calibrated to the Raman shift of silicon under excitation by the 632.8 nm line of a HeNe laser. The measured spectra were reduced to account for the thermal population factor.

Scanning electron microscopy (SEM). SEM images were obtained with a Zeiss Merlin microscope operating at 2 kV.

Photoconductivity. Photoconductivity was measured on a CdSe gel film annealed at 350 °C with silver contacts and a channel length ~2 mm and width ~1 cm. A 405 nm laser (5 mW power) was used as an illumination source. Current-voltage sweeps were run from -30 V to 30 V in the dark and under illumination. Time dependence was measured at a bias of 5 V with 100 second on-off cycles. Measurements were performed in air.

Field-effect transistor (FET) fabrication and measurements. FET fabrication and measurements were performed in a nitrogen glove box. Substrates were Si wafers with a 300 nm SiO_2 thermally grown gate dielectric layer, and they were cleaned by piranha treatment, rinsed with DI water, and dried with a stream of N_2 in air immediately before use. A ~0.025 M solution of $Na_2Cd_2Se_3$ or $(N_2H_5)_2Cd_2Se_3$ in hydrazine was spin coated on the substrates in the glove box. For gel measurements, this film was then soaked in a solution of $CdCl_2$ in methanol, but this step was skipped for measurements of the ligand itself. The film was dried at 100 °C for an hour and then annealed at various temperatures for 30 minutes. Aluminum contacts (100 nm) were thermally evaporated onto the film through a shadow mask (channel length: 50 μm, channel width: 1500 μm).

FET measurements were performed using a semiconductor analyzer (Agilent B1500A). All electron mobility values have been extracted from the forward gate voltage sweep that provides a conservative estimate for electron mobility.

Calculation of FET mobility. In the gradual channel approximation, current in the FET channel can be analytically described for two different regimes of operation.[35]

At low V_D, I_D increases linearly with V_D (linear regime):

$$I_D = \frac{WC_i\mu_{lin}}{L}\left(V_G - V_T - V_D/2\right)V_D$$

here L is the channel length, W is the channel width, C_i is the capacitance per unit area of the insulating layer, V_T is the threshold voltage, and μ_{lin} is the linear regime field-effect mobility.

μ_{lin} is calculated from the transconductance

$$g_m = \left.\frac{\partial I_D}{\partial V_G}\right|_{V_D=const} = \frac{WC_iV_D}{L}\mu_{lin}$$

by plotting I_D vs. V_G at a constant low V_D, with $V_D << (V_G - V_T)$. The slope of this plot is equal to g_m.

For $V_D > (V_G - V_T)$, I_D tends to saturate due to pinch-off of the accumulation layer (saturation regime). This case is approximately described by the equation

$$I_D = \frac{WC_i\mu_{sat}}{2L}(V_G - V_T)^2$$

μ_{sat} is calculated from the slope of $\sqrt{|I_D|}$ vs. V_G.

3.7. Chapter 3 bibliography.

1. Hudson, M. H.; Dolzhnikov, D. S.; Filatov, A. S.; Janke, E. M.; Jang, J.; Lee, B.; Sun, C.; Talapin, D. V., New Forms of CdSe: Molecular Wires, Gels, and Ordered Mesoporous Assemblies. *J. Am. Chem. Soc.* **2017,** *139*, 3368-3377.

2. Melde, J. B.; Johnson, J. B.; Charles, T. P., Mesoporous Silicate Materials in Sensing. *Sensors* **2008,** *8*, 5202-5228.

3. Zhu, W.; Wang, J.; Wu, D.; Li, X.; Luo, Y.; Han, C.; Ma, W.; He, S., Investigating the Heavy Metal Adsorption of Mesoporous Silica Materials Prepared by Microwave Synthesis. *Nanoscale Research Letters* **2017,** *12*, 323.

4. Ye, Y.; Jo, C.; Jeong, I.; Lee, J., Functional mesoporous materials for energy applications: solar cells, fuel cells, and batteries. *Nanoscale* **2013,** *5*, 4584-4605.

5. Li, W.; Liu, J.; Zhao, D., Mesoporous materials for energy conversion and storage devices. *Nat Rev Mater* **2016,** *1*, 16023.

6. Li, G.-S.; Zhang, D.-Q.; Yu, J. C., A New Visible-Light Photocatalyst: CdS Quantum Dots Embedded Mesoporous TiO2. *Environmental Science & Technology* **2009,** *43*, 7079-7085.

7. Cook, J. B.; Kim, H.-S.; Lin, T. C.; Robbennolt, S.; Detsi, E.; Dunn, B. S.; Tolbert, S. H., Tuning Porosity and Surface Area in Mesoporous Silicon for Application in Li-Ion Battery Electrodes. *ACS Appl. Mater. Interfaces* **2017,** *9*, 19063-19073.

8. Kim, J.-y.; Park, K.-W.; Kwon, O.-Y., Preparation of mesoporous silica by the rapid gelation of Na2SiO3 and H2SiF6 in aqueous surfactant solution. *Microporous and Mesoporous Materials* **2019,** *285*, 137-141.

9. Li, W.; Liu, J.; Zhao, D. Y., Mesoporous materials for energy conversion and storage devices. *Nat. Rev. Mater.* **2016**.

10. Bach, U.; Lupo, D.; Comte, P.; Moser, J. E.; Weissortel, F.; Salbeck, J.; Spreitzer, H.; Gratzel, M., Solid-state dye-sensitized mesoporous TiO2 solar cells with high photon-to-electron conversion efficiencies. *Nature* **1998,** *395*, 583-585.

11. Maschmeyer, T.; Rey, F.; Sankar, G.; Thomas, J. M., Heterogeneous catalysts obtained by grafting metallocene complexes onto mesoporous silica. *Nature* **1995,** *378*, 159-162.

12. Armatas, G. S.; Kanatzidis, M. G., Mesoporous germanium-rich chalcogenido frameworks with highly polarizable surfaces and relevance to gas separation. *Nat. Mater.* **2009,** *8*, 217-222.

13. Rangan, K. K.; Trikalitis, P. N.; Canlas, C.; Bakas, T.; Weliky, D. P.; Kanatzidis, M. G., Hexagonal pore organization in mesostructured metal tin Sulfides built with [Sn2S6](4-) cluster. *Nano Lett.* **2002,** *2*, 513-517.

14. Trikalitis, P. N.; Rangan, K. K.; Bakas, T.; Kanatzidis, M. G., Varied pore organization in mesostructured semiconductors based on the [SnSe4] (4-) anion. *Nature* **2001,** *410*, 671-675.

15. Bag, S.; Kanatzidis, M. G., Chalcogels: Porous Metal-Chalcogenide Networks from Main-Group Metal Ions. Effect of Surface Polarizability on Selectivity in Gas Separation. *J. Am. Chem. Soc.* **2010,** *132*, 14951-14959.

16. Bag, S.; Trikalitis, P. N.; Chupas, P. J.; Armatas, G. S.; Kanatzidis, M. G., Porous semiconducting gels and aerogels from chalcogenide clusters. *Science* **2007,** *317*, 490-493.

17. Staszak-Jirkovsky, J.; Malliakas, C. D.; Lopes, P. P.; Danilovic, N.; Kota, S. S.; Chang, K. C.; Genorio, B.; Strmcnik, D.; Stamenkovic, V. R.; Kanatzidis, M. G.; Markovic, N. M., Design of active and stable Co-Mo-Sx chalcogels as pH-universal catalysts for the hydrogen evolution reaction. *Nat. Mater.* **2016,** *15*, 197.

18. Bag, S.; Gaudette, A. F.; Bussell, M. E.; Kanatzidis, M. G., Spongy chalcogels of non-platinum metals act as effective hydrodesulfurization catalysts. *Nat. Chem.* **2009,** *1*, 217-224.

19. Shim, Y.; Yuhas, B. D.; Dyar, S. M.; Smeigh, A. L.; Douvalis, A. P.; Wasielewski, M. R.; Kanatzidis, M. G., Tunable Biomimetic Chalcogels with Fe4S4 Cores and [SnnS2n+2]4–(n = 1, 2, 4) Building Blocks for Solar Fuel Catalysis. *J. Am. Chem. Soc.* **2013,** *135*, 2330-2337.

20. Banerjee, A.; Yuhas, B. D.; Margulies, E. A.; Zhang, Y.; Shim, Y.; Wasielewski, M. R.; Kanatzidis, M. G., Photochemical Nitrogen Conversion to Ammonia in Ambient Conditions with FeMoS-Chalcogels. *J. Am. Chem. Soc.* **2015,** *137*, 2030-2034.

21. Schumacher, K.; Ravikovitch, P. I.; Du Chesne, A.; Neimark, A. V.; Unger, K. K., Characterization of MCM-48 materials. *Langmuir* **2000,** *16*, 4648-4654.

22. Murray, C. B.; Norris, D. J.; Bawendi, M. G., Synthesis and characterization of nearly monodisperse CdE (E = sulfur, selenium, tellurium) semiconductor nanocrystallites. *J. Am. Chem. Soc.* **1993,** *115*, 8706-8715.

23. Huang, X. Y.; Li, J.; Zhang, Y.; Mascarenhas, A., From 1D chain to 3D network: Tuning hybrid II-VI nanostructures and their optical properties. *J. Am. Chem. Soc.* **2003,** *125*, 7049-7055.

24. Deng, Z.-X.; Li, L.; Li, Y., Novel Inorganic−Organic-Layered Structures: Crystallographic Understanding of Both Phase and Morphology Formations of One-Dimensional CdE (E = S, Se, Te) Nanorods in Ethylenediamine. *Inorg. Chem.* **2003,** *42*, 2331-2341.

25. Yao, H.-B.; Gao, M.-R.; Yu, S.-H., Small organic molecule templating synthesis of organic-inorganic hybrid materials: their nanostructures and properties. *Nanoscale* **2010,** *2*, 322-334.

26. Yuan, M.; Dirmyer, M.; Badding, J.; Sen, A.; Dahlberg, M.; Schiffer, P., Controlled Assembly of Zero-, One-, Two-, and Three-Dimensional Metal Chalcogenide Structures. *Inorg. Chem.* **2007,** *46*, 7238-7240.

27. Ridley, B. A.; Nivi, B.; Jacobson, J. M., All-Inorganic Field Effect Transistors Fabricated by Printing. *Science* **1999,** *286*, 746-749.

28. Kagan, C. R.; Mitzi, D. B.; Dimitrakopoulos, C. D., Organic-Inorganic Hybrid Materials as Semiconducting Channels in Thin-Film Field-Effect Transistors. *Science* **1999,** *286*, 945-947.

29. Mitzi, D. B.; Kosbar, L. L.; Murray, C. E.; Copel, M.; Afzali, A., High-mobility ultrathin semiconducting films prepared by spin coating. *Nature* **2004,** *428*, 299-303.

30. Kagan, C. R.; Lifshitz, E.; Sargent, E. H.; Talapin, D. V., Building devices from colloidal quantum dots. *Science* **2016,** *353*.

31. Dolzhnikov, D. S.; Zhang, H.; Jang, J.; Son, J. S.; Panthani, M. G.; Shibata, T.; Chattopadhyay, S.; Talapin, D. V., Composition-matched molecular "solders" for semiconductors. *Science* **2015,** *347*, 425-428.

32. Jang, J.; Dolzhnikov, D. S.; Liu, W.; Nam, S.; Shim, M.; Talapin, D. V., Solution-Processed Transistors Using Colloidal Nanocrystals with Composition-Matched Molecular “Solders”: Approaching Single Crystal Mobility. *Nano Lett.* **2015,** *15*, 6309-6317.

33. Broxton, T. J.; Chung, R. P. T., Micellar catalysis of organic reactions. 27. Micellar bound Meisenheimer complexes. *The Journal of Organic Chemistry* **1990,** *55*, 3886-3890.

34. Ravel, B.; Newville, M., ATHENA, ARTEMIS, HEPHAESTUS: data analysis for X-ray absorption spectroscopy using IFEFFIT. *J Synchrotron Radiat* **2005,** *12*, 537-541.

35. Kagan, C. R.; Andry, P., *Thin-Film Transistors*. Taylor & Francis: 2003.

4. Spectroscopic evidence of conduction band fine structure in colloidal HgTe quantum dots with well-defined intraband transitions

4.1. Introduction to HgTe QDs and QD doping.

Colloidal semiconductor nanocrystals have outstanding optoelectronic properties that can be readily tuned through manipulation of nanocrystal size, shape, and surface passivation. Semiconductor nanocrystals smaller than the Bohr exciton radius, termed quantum dots (QDs), display size-dependent absorption and emission. Much work has focused on the development of colloidal QDs as spectrally narrow absorbers and emitters in the visible and near-infrared (IR) for use in light emission,[2-4] photovoltaics,[5-7] and solar concentrators.[8-9] To extend sensitivity into the mid- to far-IR, colloidal QD syntheses of narrow bandgap semiconductors (InSb,[10] PbSe[11]) and semimetals (HgSe,[12] HgTe,[13-14] Cd_3As_2[15-16]) have been established. Developments in the synthesis of HgTe QDs have yielded routes to size-uniform, narrow absorbers from the near- to far-IR.[14, 17-19] These HgTe QDs show remarkable performance as the active layer in solution-processed infrared photodetectors,[13, 20] reaching background-limited performance in photovoltaic devices.[21-23]

In addition to QD size control and corresponding spectral tuning, device applications of QDs require precise control over the electronic doping of a QD ensemble. Delocalized electrons can be introduced into the quantum confined states of a QD sample electrochemically[24-26] or chemically, through reaction with a reducing agent,[27] sometimes accompanied by photoexcitation.[28] However, such doping is often transient; the nanocrystals relax back to their

undoped state upon removal of the applied bias or over time. Stable nanocrystal doping can be achieved through incorporation of aliovalent impurities into the lattice (*e.g.* Al^{3+} in ZnO[29]) or by tuning the potential of the electronic states with respect to the environment through modification of the QD surface chemistry.[30-31] These additional electrons reside in discrete, quantum confined states derived from the conduction band of the bulk semiconductor (here referred to as conduction band states). The presence of electrons in the first conduction band state, the $1S_e$ state, of a QD sample can be identified spectroscopically by the suppression of band-edge absorption due to Pauli blocking and the emergence of intraband absorbance significantly below the QD bandgap due to excitations from the doped state to higher energy states.

Mercury chalcogenide (HgE, E = S, Se, Te) QDs are a rich system for the exploration of electronic doping. When synthesized with a mercury-rich surface, HgE QDs display robust n-type doping under ambient conditions, evidenced by band-edge bleaching and intraband absorbance in the mid- to far-IR.[12, 30, 32-34] Upon treatment with S^{2-}, the electron doping vanishes, yielding intrinsic QDs with no intraband absorbance and recovered interband transitions. The stable doping in mercury-rich HgSe QDs has been utilized to create intraband photodetectors with narrow spectral response in the mid-IR.[12] Recent progress in the synthesis of HgTe QDs has yielded improved colloidal stability and air-stable n-doping, expanding the versatility of these materials for further study.[33]

Here, we observe splitting of the intraband transition in the absorbance of electron-doped HgTe QDs into three peaks. The peak positions of the individual components follow a robust trend with changing nanocrystal size, independent of the QD doping level. We suggest that the intraband absorbance corresponds to transitions between the occupied $1S_e$ state and a series of nondegenerate $1P_e$ states. The strong spin-orbit coupling of HgTe, size uniformity of the

synthesized QDs, and deep work function of mercury-rich HgTe QDs allow us to observe this splitting in a colloidal QD solution.

4.2. HgTe QD synthesis and characterization.

Highly monodisperse HgTe QDs were synthesized using slight modifications to a reported procedure.[33] Briefly, QDs were made by injection of bis(trimethylsilyl)telluride (TMS_2Te) into a hot solution of $HgCl_2$ in oleylamine and growth at mild temperatures (70-120 °C) for 4 to 6 minutes. The QD growth was quenched by injection of anhydrous tetrachloroethylene (TCE), and the QDs were washed with toluene/methanol in a nitrogen glove box. The diameter can be controlled between 5 nm to 13 nm by tuning the injection and growth temperatures and the ratio of Hg to Te precursors. The synthesized QDs have a nearly spherical shape, uniform size, and zinc blende crystal structure, and their absorbance spectra show several clear excitonic transitions (Figures 4.1-4.2). We found that limiting the time that $HgCl_2$ is kept at elevated temperature in oleylamine and completing all post-synthetic processing in a nitrogen glovebox improved batch to batch reproducibility.

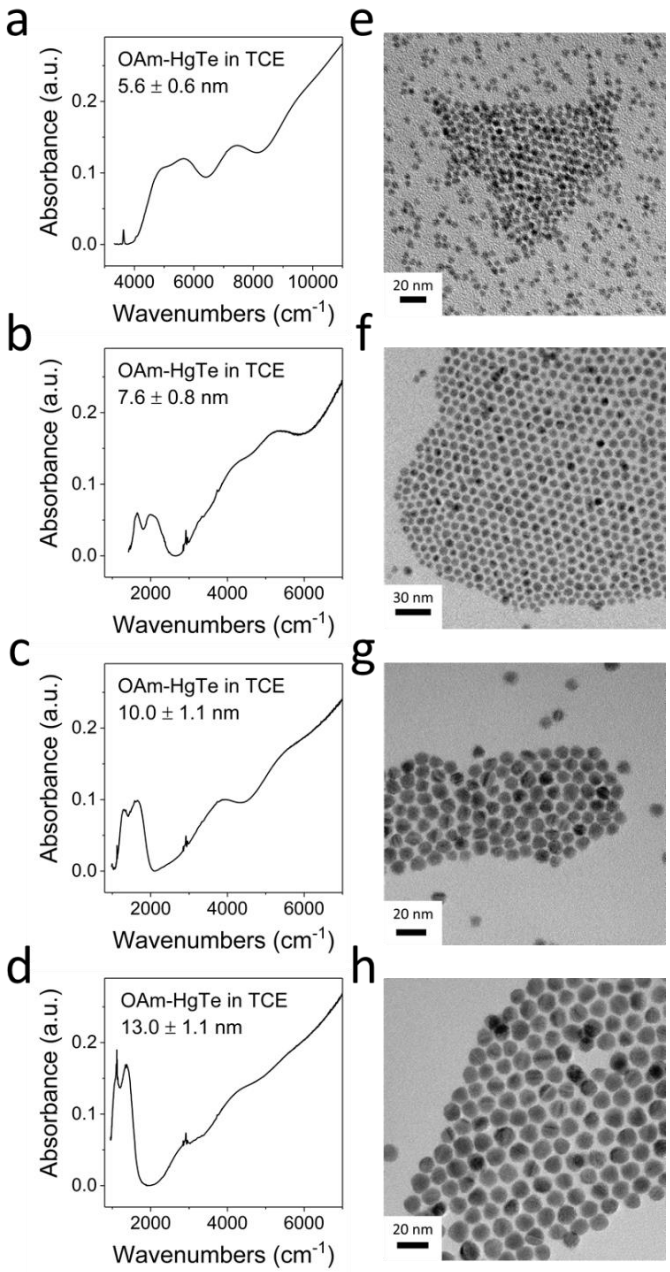

Figure 4.1. HgTe QD absorbance spectra and TEM images.
(a-d) Absorbance spectra for solutions of oleylamine-capped HgTe QDs in TCE show several well-defined excitonic features and intraband absorbance indicative of n-doping for large QDs. Peaks from the TCE solvent and oleylamine capping ligands have been subtracted. *(e-h)* Transmission electron microscope (TEM) images of the corresponding particles indicate that the particles are nearly spherical and uniform in size.

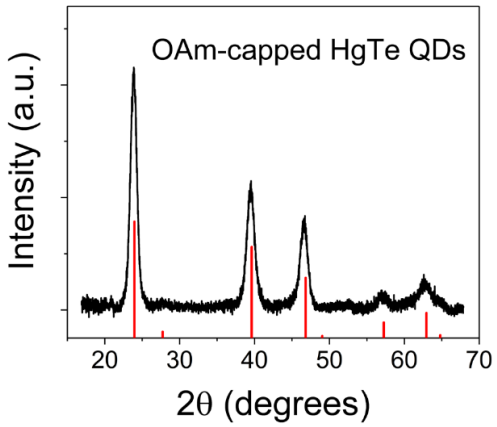

Figure 4.2. HgTe QD XRD pattern.
Representative powder x-ray diffraction (XRD) pattern for a film of HgTe QDs. Red bars indicate the standard peaks for zinc-blende HgTe.

Due to the deep conduction band energy, HgTe QDs are spontaneously electron-doped under ambient conditions.[33] To recover the intrinsic properties of our QDs, we use a mild iodine treatment in TCE to oxidize the doped QDs and yield particles without free electrons (Figure 4.3). This de-doping is not accompanied by an appreciable shift in exciton energies, indicating that the treatment has not changed the QD size.

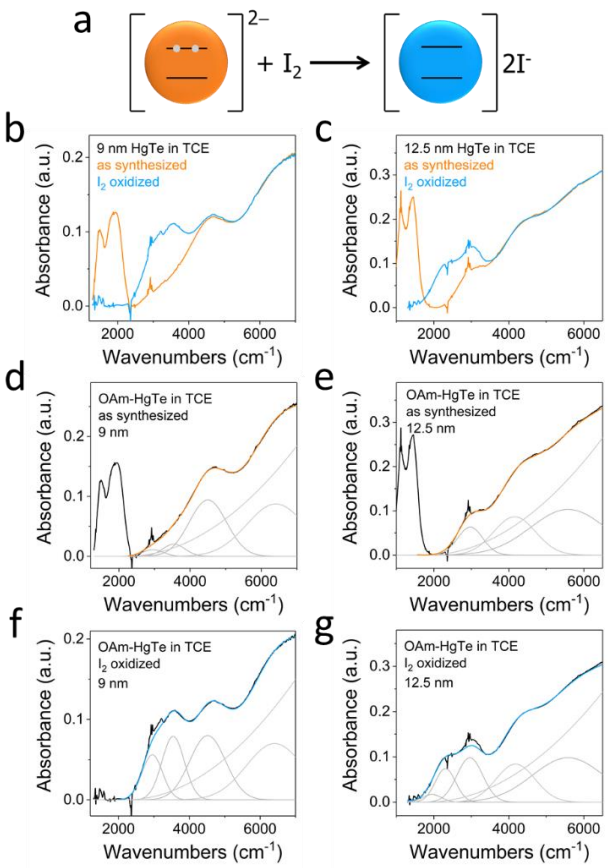

Figure 4.3. Chemical control of HgTe QD doping.
(a) Schematic of QD oxidation by iodine. *(b-c)* FTIR absorbance spectra of two samples of HgTe QDs in TCE before and after oxidation with I_2 and *(d-g)* the corresponding fits of these spectra using a sum of Gaussians and a parabolic background. Signals from oleylamine and TCE have been subtracted.

The absorbance of intrinsic HgTe QDs can be tuned throughout the infrared by controlling the QD size and thus the degree of quantum confinement. Sharp peaks corresponding to molecular vibrations of the solvent and surface-bound organic ligands overlay the characteristic QD absorbance in the solution spectra (Figure 4.4), but these peaks can be subtracted to yield spectra with representative QD absorbance. Under our synthetic conditions, the absorbance onset is around 4,000 cm^{-1} (0.5 eV, 2.5 μm) for small nanocrystals of 6 nm in diameter and can reach approximately 1,650 cm^{-1} (0.2 eV, 6.0 μm) at sizes up to 13 nm (Figure 4.5a). Absorbance further into the infrared can be achieved by particle regrowth upon

introduction of additional precursors (Figure 4.6).[35] Addition of a half equivalent of TMS_2Te to 13 nm QDs at 120 °C yielded 15 nm QDs with an absorbance onset at 1,200 cm^{-1} (0.15 eV, 8.3 μm). Given the large Bohr exciton radius of HgTe (40 nm),[36] size effects on absorbance should be seen up to large nanocrystal sizes, on the order of 100 nm, as recently demonstrated by Lhuillier and colleagues.[37]

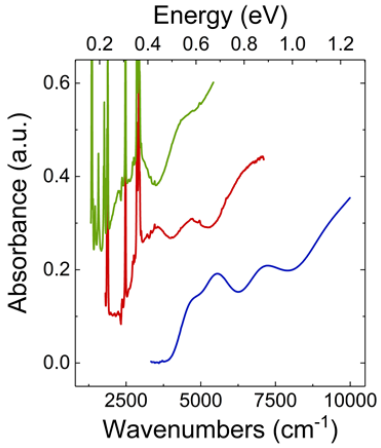

Figure 4.4. Raw HgTe QD absorbance spectra.
Raw spectra from *Figure 4.5* before subtraction of peaks from oleylamine and TCE.

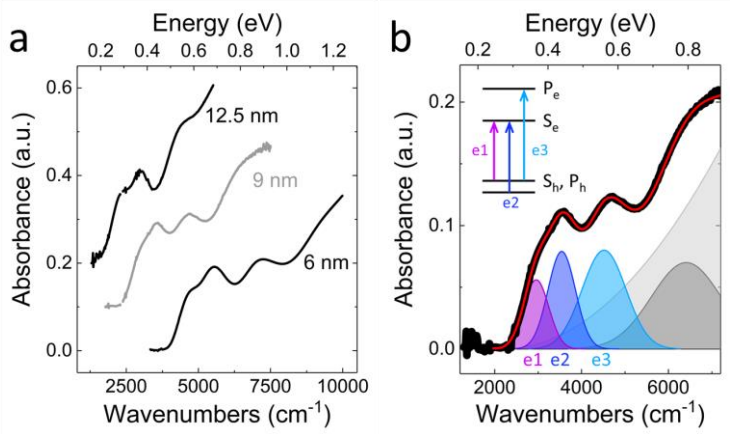

Figure 4.5. Absorbance spectra for intrinsic HgTe QDs.
(a) Solution absorbance spectra for three sizes of intrinsic HgTe QDs in TCE show several clear excitonic features and a strong blueshift in the absorption onset with increasing confinement. Infrared absorbance from the solvent (TCE) and ligands (oleylamine) has been subtracted. *(b)* The absorbance spectrum for 9 nm HgTe QDs can be fit with a sum of four Gaussians and a parabolic background. The data is shown as a bold black line, and the fit is shown in red. The inset demonstrates the corresponding electronic transitions for the first three excitonic peaks (e1, e2, and e3).

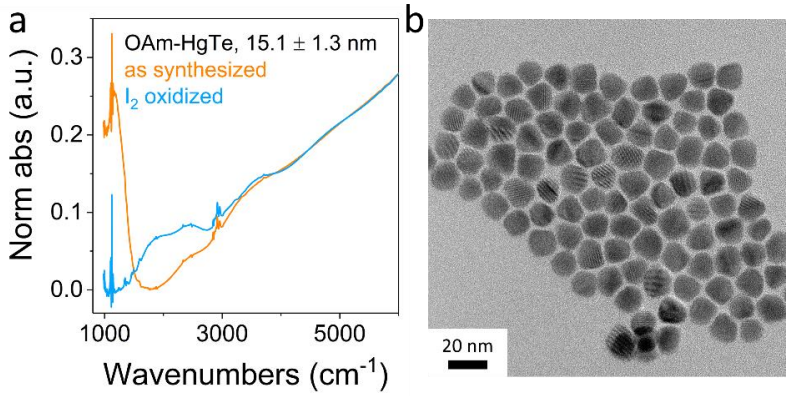

Figure 4.6. Characterization of large HgTe QDs.
(a) FTIR absorbance spectra of 15 nm HgTe QDs before and after iodine oxidation and *(b)* a TEM image of the corresponding particles.

Across a range of nanocrystal diameters, three to four clear excitonic features can be resolved in the infrared absorbance spectra of intrinsic HgTe QDs dispersed in TCE (Figure 4.5). The spectra can be fit using a sum of Gaussians and a parabolic background function (Figure 4.5b), and the three lowest energy peaks can be assigned to electronic transitions from valence band states to the $1S_e$ and $1P_e$ conduction band states, based on a previously reported tight-binding model.[35, 38] Comparison of the energy of the excitonic transitions for many sizes of intrinsic HgTe QDs reveals a robust trend for each transition with increasing quantum confinement (Figure 4.7). Notably, the first excitonic feature exhibits a decreased relative oscillator strength as compared to more common QD systems (*e.g.* CdSe[39]), and it gets suppressed as the QD diameter increases. For large QDs, the first absorbance feature nearly disappears into a seemingly broad absorption onset; however, this first excitonic feature can be resolved as a clearly defined shoulder in small HgTe (Figure 4.5a, 6 nm QDs) and becomes clear upon Gaussian fitting for larger nanocrystals (Figure 4.5b).

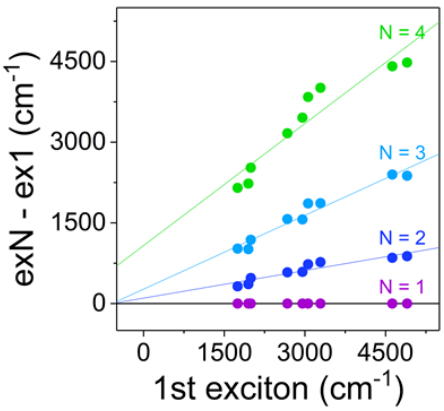

Figure 4.7. Excitonic peak trends for intrinsic HgTe QDs.
Plot of the difference of excitonic energies and the first excitonic energy versus the position of the first exciton for several solutions of intrinsic HgTe QDs. Peak positions are based on fits of IR absorbance spectra to a sum of Gaussians and a parabolic background. Linear fits are given as a guide to the eye.

The monodispersity of the HgTe QDs was assessed with small-angle x-ray scattering (SAXS) and self-assembly experiments. SAXS measurements in the 0.005 – 1 $Å^{-1}$ region of momentum transfer space (q-space) are routinely used to determine the size of colloidal nanoparticles.[40] Size determination from SAXS is preferable to transmission electron microscopy (TEM) size analysis because it is free of selection bias, offering size distribution statistics at the ensemble level. We measured SAXS on solutions of HgTe dispersed in hexane and found that the scattering curves exhibit a characteristic leveling off of the intensity at $q < 1/R_g$ (Guinier region), where R_g is the radius of gyration. This indicates that the particles form dilute-limit colloidal solutions and that the scattering intensity is determined solely by the particles' form factor. The data were further fit using a model-free Maximum Entropy approach to determine the average diameter and size distribution (Figure 4.8). The five HgTe samples each have a size polydispersity of approximately 10%, which is on par with well-developed nanocrystal syntheses (*e.g.* CdSe,[41] Pd[42]). For the small QDs (7.6 nm, 8.1 nm, and 8.9 nm), this size distribution was achieved directly from synthesis, but the larger QDs (10.0 nm and 13.0 nm) were size-selected

into 4 fractions to improve the monodispersity. Future work could improve the size distribution through more precise temperature modulation and controlled TMS_2Te injection rate or with extensive post-synthetic size selection.

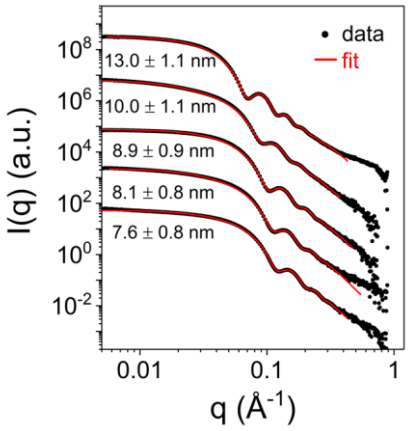

Figure 4.8. SAXS data and fits for colloidal solutions of HgTe QDs.
SAXS data and corresponding fits for colloidal solutions of HgTe QDs show good size control (~10% diameter distribution) across a range of samples.

The small size and shape variation of these particles is further demonstrated by their propensity to crystallize into well-ordered superlattices (Figure 4.9). Upon slow evaporation of a solution in TCE onto a tilted TEM grid, the QDs self-organize into face-centered cubic (fcc) arrays with ordered domains of several square microns. The diameter of the nanocrystals is directly correlated to the lattice spacing of this array, and we have shown that several sizes of HgTe QDs form fcc superlattices. Monodisperse spheres preferentially crystallize into fcc arrays to maximize their packing density,[43] and the adoption of this structure in our sample suggests that our QDs plus their bound ligand shell can be approximated as monodisperse spheres.

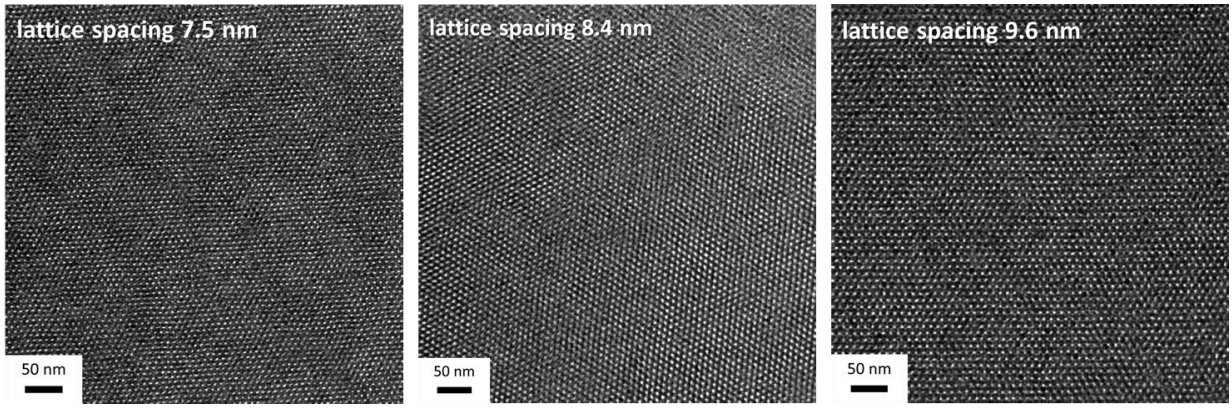

Figure 4.9. HgTe QD superlattices.
TEM images of superlattices made from three sizes of HgTe QDs, formed by slow evaporation from TCE.

4.3. Optical characterization of electron-doped HgTe QDs: appearance of multiple intraband transitions.

The high degree of size uniformity of these QDs allows us to observe multiple well-defined features in the intraband absorbance of many samples of n-doped HgTe. As mentioned above, large HgTe QDs synthesized in a mercury-rich solution are spontaneously electron-doped by the environment due to their deep conduction band.[33] With proper surface passivation, this n-doping is air-stable. By introducing electrons into the $1S_e$ state, doping suppresses the first two excitonic transitions and induces a low-energy intraband absorbance corresponding to excitation from the $1S_e$ state to higher conduction band states (Figure 4.10a-b). Figure 4.10a shows a direct comparison of the absorbance spectra for n-doped HgTe QDs under ambient conditions and the same sample after oxidation with molecular iodine. A Gaussian fit of the n-doped QDs demonstrates the strong suppression of the first two excitonic transitions (e1 and e2), corresponding to excitation from valence band states to the $1S_e$ state, and little change in the third excitonic transition (e3), corresponding to excitation from valence band states to the $1P_e$ state (Figure 4.10b). The intraband absorbance in the n-doped sample spans from 1200 to 2300

cm^{-1} and shows a pronounced dip in the absorbance at ~1550 cm^{-1}. Using a sum of Gaussians, the intraband absorbance can be well-modeled with a minimum of three peaks corresponding to three intraband transitions, i1-i3 (Figure 4.10b). The dip in the intraband absorbance and shoulder indicating three peaks can be observed at different energies in several sizes of HgTe QDs, confirming that we indeed observe three intraband transitions and not a measurement artifact (Figure 4.10c). The Gaussian fitting procedure was applied for many samples of QDs, and the energies of the three intraband transitions show a robust trend with confinement energy (Figure 4.11).

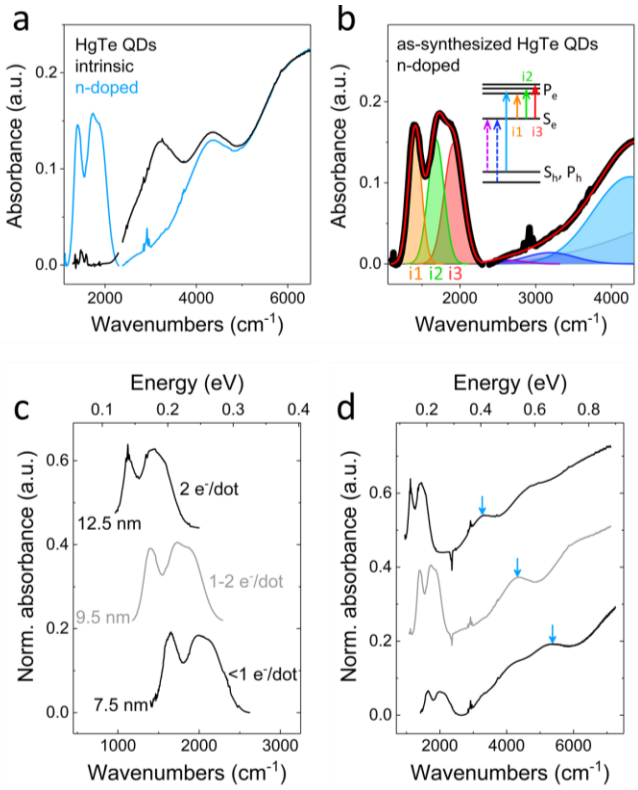

Figure 4.10. Characterization of optical absorbance for n-doped HgTe QDs.
(a) Solution absorbance spectra of HgTe QDs as-synthesized (n-doped) and after oxidation with molecular iodine (intrinsic). *(b)* A fit of the n-doped HgTe QDs' spectrum to a sum of Gaussians indicates that doping suppresses the first two excitonic transitions (e1, e2) and induces intraband absorbance (i1-i3). The data is a bold black line, and the fit is a red line. *(c)* The intraband absorbance for different sizes of QDs with different doping levels has similar spacing and relative intensity for the three peaks but the peak positions shift with size. *(d)* Comparison of the full absorbance spectra for the samples in *(c)* illustrates the difference in doping for the three samples, based on the difference in relative intensity of the intraband absorbance compared to the excitonic features. The blue arrows indicate the position of the third excitonic transition (e3).

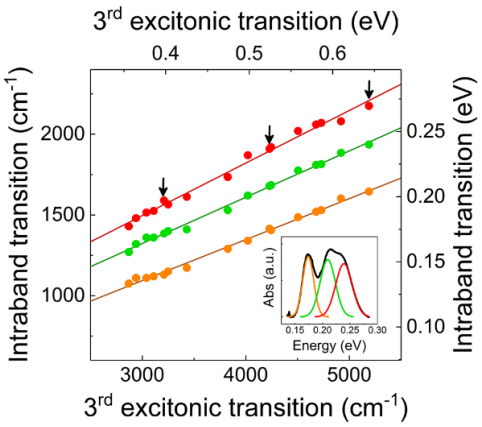

Figure 4.11. Intraband peak trends for n-doped HgTe QDs.
This shows the intraband peak positions, based on fits of solution absorbance spectra to a sum of three Gaussians, for 15 samples of n-doped HgTe QDs plotted against the energy of the third excitonic transition. Here, the third excitonic transition is used as a proxy for confinement energy because it does not bleach with electron doping. The inset shows a sample fit of the intraband portion of the spectrum, and the black arrows indicate the samples shows in Figure 4.10c-d.

Here, we observe robust, size-dependent splitting of the intraband features for colloidal QDs under ambient conditions. Studies of chemically n-doped CdSe have shown multiple intraband features in a few select samples and suggested that it may be due to lifting the degeneracy of the P_e state; however, the origin of these features was not studied extensively.[27-28] Electrochemically doped tetrahedral HgTe QDs prepared under different synthetic conditions show one intraband feature at doping levels up to two electrons per dot and an additional feature at higher doping densities.[44] In our QDs, the split intraband features could be interpreted either as excitations from the $1S_e$ state to a series of nondegenerate $1P_e$ states or as an excitation from $1S_e$ to $1P_e$ and, if the particles are heavily doped, an excitation from $1P_e$ to higher conduction band states. We can determine the influence of doping by comparing the intraband spectra for nanocrystals of different sizes. Larger HgTe QDs have deeper conduction band states because they are less quantum confined, so the as-synthesized QDs are more heavily doped at larger diameters.[33] Figure 4.10d shows that the relative intensity of the intraband absorbance to the

interband absorbance (third exciton, which remains unbleached, marked by a blue arrow) increases at larger sizes, confirming that the larger nanocrystals are more heavily doped.[12] Upon comparison of the normalized intraband spectra (Figure 4.10c), we see that the peak spacing and relative intensity of the three peaks remain nearly constant at different doping densities, though the absolute position of the peaks shifts with size. We would expect the relative intensity of the three peaks to change with doping density if the transitions did not originate from the same ground state. Therefore, we propose that the observed intraband features correspond to transitions from the $1S_e$ state to a series of nondegenerate $1P_e$ states.

4.4. Trends in the excitonic and intraband absorbance peak energies for HgTe QDs.

Compilation of the absorbance data for both doped and intrinsic HgTe QDs allows us to construct a more complete understanding of their electronic structure. The energies of the QD transitions (e1-e3, i1-i3) were plotted against the QD diameter determined from SAXS (Figure 4.12a). The diameters obtained from SAXS and the third excitonic position, present in both intrinsic and n-doped QDs, were used to construct a sizing curve for HgTe QDs (Figure 4.12b). The peak energies indicated by a filled circle or x-symbol were determined from fits of the solution absorbance spectra to a sum of Gaussians and a parabolic background function. Spectra for n-doped QDs were used for the intraband transitions (i1-i3), and spectra for I_2-treated, intrinsic QDs were used for the first and second excitonic transitions (e1, e2). The third excitonic position could be determined from either doped or intrinsic QDs because its position and intensity are largely independent of doping level. The open circles and filled triangles indicate estimated positions of the first and second excitonic transitions for doped QDs based on their linear relationship to the third excitonic energy. Both the excitonic and intraband transitions

exhibit a monotonic decrease in energy with increasing QD diameter. This confirms that the intraband absorbance correlates to electronic transitions between quantum-confined states.

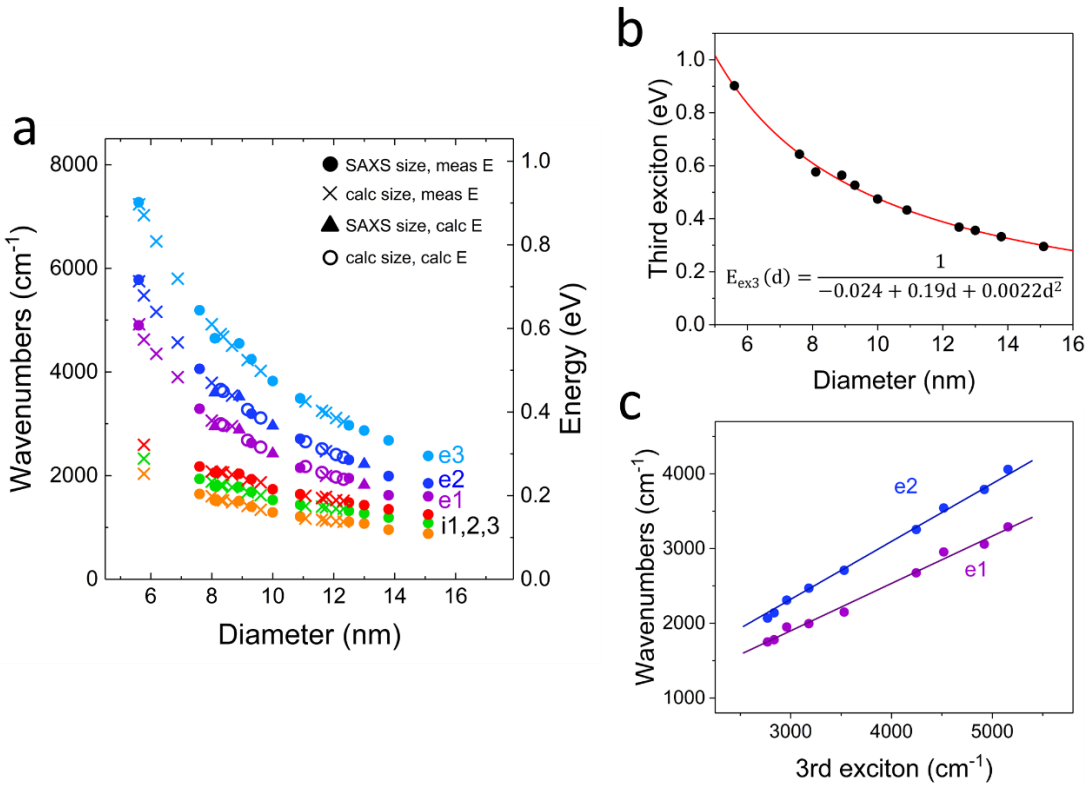

Figure 4.12. HgTe QD sizing curve for excitonic and intraband transitions.
(a) Shows the relationship of the peak position (e: excitonic; i: intraband) to the diameter for a number of HgTe QD samples. Filled circles indicate that the diameter was obtained from SAXS and the peak positions were obtained from Gaussian fits to the absorbance spectra. For the samples for which we do not have SAXS data, the diameter was determined by using *(b)* a sizing curve that relates the position of the third excitonic peak (in eV) to the SAXS diameter. For the sizing curve, we use a function previously used for modeling CdSe and PbSe with the form $E_g = E_{bulk} + (a + b*d + c*d^2)$, where the bulk bandgap is 0 eV and d is the diameter.[45-46] The samples for which the size was determined from the sizing curve are marked with an "X" in *(a)*. For several samples, we only have spectra for the n-doped QDs and thus cannot directly measure the positions of the first and second excitonic peaks. *(c)* We plotted the position of the first and second excitonic peaks versus the third excitonic peak for all of our intrinsic QD samples, and they can be fit to lines. Using these linear fits, we calculated the expected first and second excitonic peak positions for these samples, marked with a filled triangle for diameters obtained from SAXS and marked with an open circle for diameters calculated from the sizing curve.

The change in each transition with size is fit to a function of the form $(a + bd + cd^2)^{-1}$, where d is the diameter (Table 4.1).[45-46] Using these equations and the size distribution obtained from SAXS, we can predict the line broadening of each transition due to polydispersity and compare this with our experimental results (Table 4.2). The width of the first excitonic peak is comparable to other well-developed QD syntheses (~70 meV) and is well estimated by the calculated polydispersity-based peak broadening. Interestingly, the width of the intraband peaks is quite narrow, on the order of 30 meV, and is slightly narrower than our polydispersity-based broadening calculations, likely due to overestimation of the polydispersity by SAXS because of particle asphericity.[40] Hole-burning experiments on CdSe and InP have previously shown that the homogeneous intraband linewidth can be very narrow, approximately 10 meV at 200K and as low as 3 meV at 10K.[47] This suggests that the homogeneous intraband linewidth of HgTe QDs is likely much narrower than seen here in our ensemble measurement. The sharp linewidths of the HgTe intraband transitions can be explained as coming from two factors. First, the weak size dependence of the intraband transition energy mitigates polydispersity-related broadening. Second, there is a reduction in fine structure broadening that arises from the nondegeneracy of the P_e states. Each observed peak in the intraband region of the spectrum is related to a transition from $1S_e$ to a single $1P_e$ state.

Table 4.1. HgTe QD sizing curve equations.
Table of parameters for the fits to each of the excitonic (e1-e3) and intraband (i1-i3) transition energies as a function of QD diameter. The trends in the absorbance peak positions (in eV) with increasing diameter follow the equations given in the table.

	$E(d) = \frac{1}{a + bd + cd^2}$		
transition	***a***	***b***	***c***
e3	-0.024	0.19	0.0022
e2	-0.15	0.26	0.0022
e1	-0.57	0.40	-0.0014
i3	1.61	0.22	0.0069
i2	1.45	0.33	0.0042
i1	1.23	0.45	0.0039

Table 4.2. Comparison of experimental and calculated peak broadening for HgTe QDs.
Experimental (exp) data for the full width at half maximum (FWHM) of the absorbance peaks for three samples of HgTe QDs and the corresponding calculated (calc) peak broadening based on polydispersity using the size distribution from SAXS and energies from the equations in Table 4.1 (in eV).

HgTe diameter	method	e1 FWHM	e2 FWHM	e3 FWHM	i1 FWHM	i2 FWHM	i3 FWHM
9.32 nm FWHM: 1.98	exp	0.067	0.096	0.147	0.023	0.035	0.035
	calc	0.082	0.099	0.123	0.031	0.034	0.038
10.85 nm FWHM: 2.39	exp	0.070	0.093	0.131	0.025	0.031	0.032
	calc	0.069	0.087	0.109	0.030	0.033	0.038
12.49 nm FWHM: 2.37	exp	0.073	0.079	0.099	0.026	0.029	0.032
	calc	0.049	0.064	0.081	0.023	0.027	0.032

4.5. HgTe QD spectroelectrochemistry.

As-synthesized, the maximum doping density that is achieved for a HgTe QD sample is determined by its size and processing conditions and is difficult to precisely control. By using spectroelectrochemistry, we can observe changes in the absorbance of a QD sample at a range of controlled doping densities.[24-26, 30, 44, 48] In this technique, the absorbance of a QD film is measured under a series of potentials applied in an electrochemical cell. Thus, we can manipulate the Fermi level of a QD film and observe the intraband absorbance and excitonic bleach across a range of doping levels (Figure 4.13).

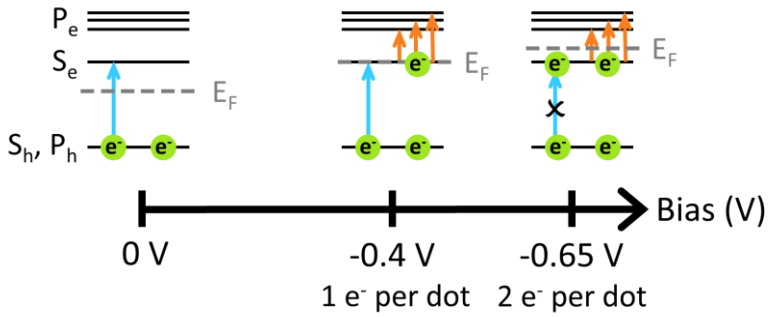

Figure 4.13. Spectroelectrochemistry diagram for HgTe QDs.
Illustration of the change in the Fermi level (E_F) with applied negative bias and its effect on the interband absorbance (blue arrow) and intraband absorbance (orange arrows) of a QD film.

We synthesized a batch of small HgTe QDs (~ 6 nm), such that the intraband absorbance fell in the transparency window of the solvent (propylene carbonate, PC) and electrolyte (tetrabutylammonium perchlorate, TBAP). A film was prepared by drop-casting a concentrated QD solution onto a glass substrate with interdigitated gold electrodes. To make the sample sufficiently conductive, the QDs were cross-linked with ethanedithiol through an on-film ligand exchange.[21] The resulting QD film was placed in a cell with electrolyte solution (PC/TBAP) and pressed against a KBr window to minimize solvent absorbance. A bias was applied to the film using a bipotentiostat with electrochemical potentials monitored with a silver wire

pseudoreference. This cell was placed in an FTIR spectrometer, and the absorbance of the film was measured in reflectance mode across a series of applied biases at room temperature. The spectrum of the intrinsic HgTe QD film at 0 V *vs* Ag/AgCl was taken as a background, and the change in absorbance at a given bias was measured (Figure 4.14a).

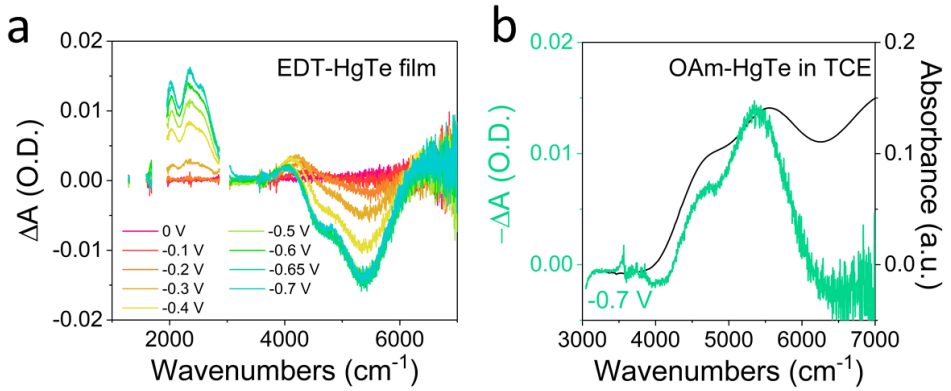

Figure 4.14. HgTe QD spectroelectrochemistry results.
(a) Differential absorbance spectra for a film of EDT-crosslinked HgTe QDs under a series of biases *vs* Ag/AgCl. As a negative bias is applied, intraband absorbance features appear and the first two excitonic features are bleached. *(b)* The bleach in spectroelectrochemistry matches the energy of the first two excitonic features in a solution absorbance measurement of the as-synthesized HgTe QDs.

Several features change in the absorbance of the HgTe QDs under negative bias. In the interband region of the spectrum, two bleach features appear which correspond closely to the position of the first two excitonic features in the absorbance spectrum of the as-synthesized QDs (Figure 4.14b). Additionally, an induced absorbance appears below the first excitonic bleach. At lower energies, we see an induced absorbance with three closely-spaced peaks that matches the intraband absorbance seen in chemically doped QDs. The peak spacing and relative oscillator strength of the three peaks do not change with increasing bias. This suggests that under our experimental conditions we only observe the effects of doping up to two electrons per QD because additional intraband absorbance features should emerge at high bias upon doping of the

$1P_e$ level.[44] This further confirms that the three intraband transitions observed in HgTe QDs occur from the first conduction band state ($1S_e$) to a series of closely-spaced excited states. Moreover, the consistent intraband lineshape across the applied bias indicates that electron-electron interactions in QDs doped with two electrons do not have a significant effect on the state energies or transition probability.

As the bias becomes more negative and the electron doping increases, the magnitude of the excitonic bleach and intraband absorbance increases and then plateaus when the $1S_e$ state is filled with two electrons. As shown previously with CdSe, the change in absorbance as a function of bias can be modeled to determine the QD band positions.[26, 48] When the Fermi level is aligned with the $1S_e$ state, the state has a 50% probability of being filled with electrons according to Fermi-Dirac statistics. Assuming that the induced absorbance or bleach is directly proportional to the electron occupation, the point at which the Fermi level aligns with the state should be at the midpoint of the intensity increase for the peak in question. Here, the midpoint for each of the observed transitions is approximately -0.4 V *vs* Ag/AgCl, and the point at which the absorbance plateaus, corresponding to full occupation of the $1S_e$ state, is between -0.6 V and -0.65 V (Figure 4.15). Using cyclic voltammetry, we confirmed that the $1S_e$ state contains one electron at approximately -0.4 V *vs* Ag/AgCl and two electrons at approximately -0.65 V (Figure 4.16).

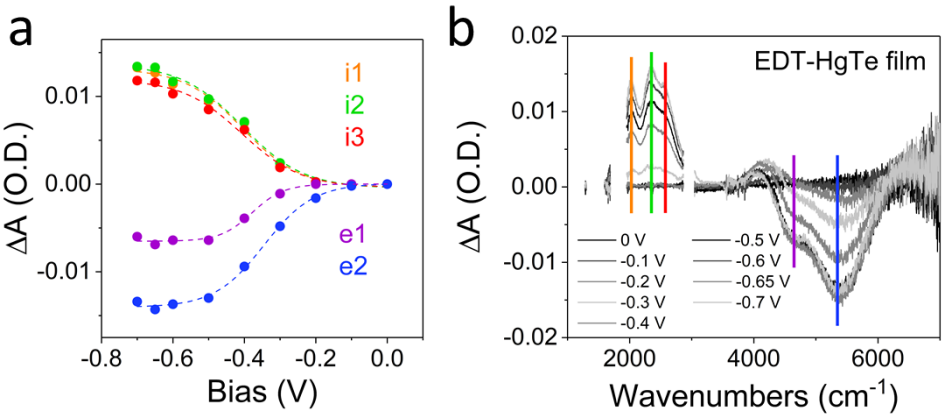

Figure 4.15. HgTe QD spectroelectrochemistry analysis.
(a) The change in absorbance for 3 intraband transitions (i1-i3) and two excitonic bleaches (e1, e2) as a function of applied bias *vs* Ag/AgCl and their sigmoidal fits, with the position of each transition marked in *(b)* with the corresponding color.

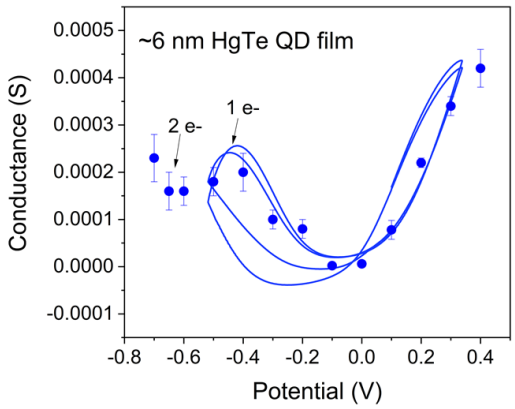

Figure 4.16. HgTe QD cyclic voltammetry.
Cyclic voltammetry of a film of HgTe QDs crosslinked with EDT, where the conductance maximum (minimum) at negative potential indicates one electron (two electrons) in the $1S_e$ state.[49] Potential is given *vs* Ag/AgCl.

4.6. Tight binding calculations for HgTe QDs.

To understand the observed splitting of the $1P_e$ state in HgTe QDs, we modeled the intraband absorbance using a well-established tight-binding model.[13, 38] We found that for highly symmetric particle shapes, *e.g.* spheres (Figure 4.17a), the intraband absorbance is split into two peaks due to spin-orbit coupling. To account for the additional splitting of the higher energy peak observed experimentally, we considered the effect of lower symmetry confinement potentials.

For asymmetric particle shapes, *e.g.* oblate ellipsoids and truncated cubes with unequal truncations, we predict splitting of the intraband absorbance into three peaks that closely mimics experimental results (Figures 4.17b-c). Moreover, the predicted intraband peak positions for many sizes of truncated cubes follow the size trends observed experimentally (Figure 4.17e). Thus, the $1P_e$ level is split primarily by strong spin-orbit coupling and additionally split by asymmetry that breaks the degeneracy of the x, y, and z axes (Figure 4.17d). Based on close examination of high resolution TEM images, our HgTe QDs are reasonably modeled as a low-symmetry near-sphere like a truncated cube (Figure 4.18). Our TEM images also reveal planar defects which could account for the reduction of symmetry in the confinement potential.

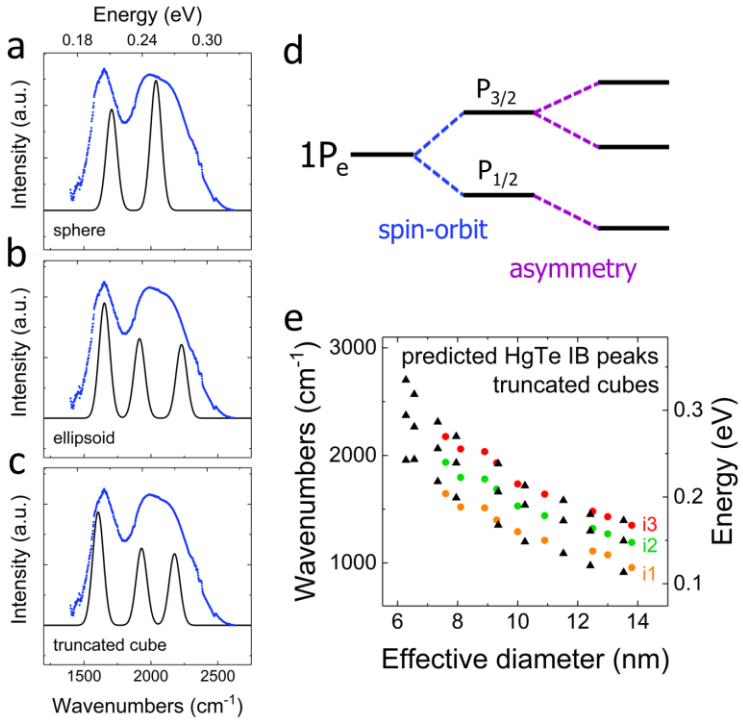

Figure 4.17. Results of HgTe QD tight binding calculations.
(a-c) Predicted intraband absorbance spectra (black lines) for several shapes of HgTe QDs with a volume equal to a sphere with a radius of 4 nm and comparison with experimental data for a solution of 7.6 nm diameter QDs (blue points). *(d)* Schematic demonstrating the splitting of the P_e state by both spin-orbit coupling and structural asymmetry. *(e)* Comparison of predicted intraband peaks (black triangles) for many sizes of truncated cubes and experimental data (colorful circles). The size is given as the effective diameter of a sphere with volume equal to that of the modeled truncated cube.

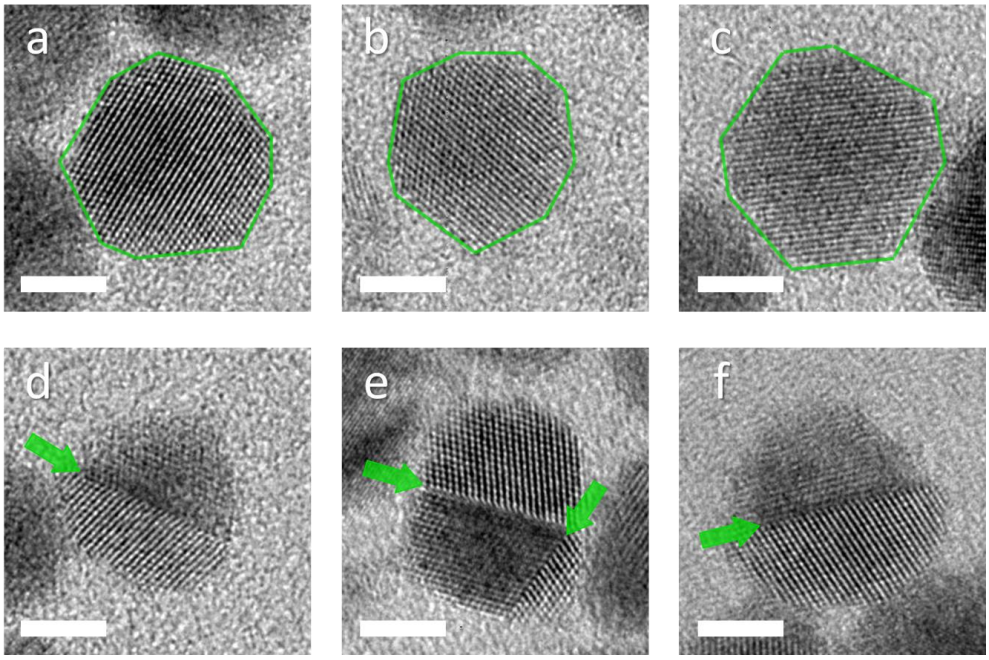

Figure 4.18. High resolution TEM images of HgTe QDs.
High resolution TEM images of HgTe QDs, all scale bars: 5 nm. *(a-c)* Green outline indicates edges, highlighting non-uniform shapes. *(d-e)* Green arrows indicate plane defects.

4.7. Conclusions.

We have demonstrated direct spectroscopic evidence of conduction band fine structure in electron-doped HgTe QDs. Robust splitting of the intraband absorbance into three peaks is observed across many QD samples with different confinement and doping levels. This splitting can only be observed for monodisperse QDs (Figure 4.19), where the absorbance linewidths are narrow and the overlap between peaks is minimized. Furthermore, spectroelectrochemical measurements reveal that the peak spacing and relative oscillator strengths of the three peaks do not change appreciably with doping level. The three peaks seen in the intraband spectra correspond to transitions from the lowest conduction band state, $1S_e$, to a series of three nondegenerate $1P_e$ states. The significant splitting into two well-defined peaks can be rationalized by spin-orbit coupling, which is much more pronounced for heavy metal tellurides

than for the analogous selenides or sulfides. Thus, split intraband peaks were not observed in previous studies of n-doped HgS or HgSe.[30, 32, 34] The intraband spectra can be well-modeled by a sum of three Gaussian peaks, suggesting that there is additional splitting of the $1P_e$ state. This may be rationalized by structural asymmetry of the particles which breaks the degeneracy of x, y, and z.

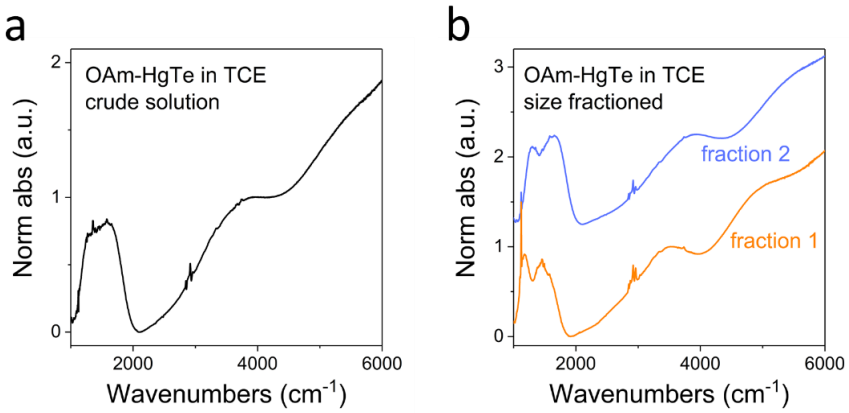

Figure 4.19. Role of HgTe QD polydispersity in intraband peak splitting.
(a) The intraband feature appears as a single peak in a polydisperse sample of HgTe QDs, *(b)* but upon size fractionation of this sample two intraband peaks can be clearly resolved in the absorbance spectra of the fractions with improved size uniformity.

4.8. Materials and methods.

Materials. $HgCl_2$ (≥ 98%), iodine (99.99 %), 1,2-ethanedithiol (≥98.0% (GC)), HCl (ACS reagent, 37%), isopropanol (≥99.7%, FG), tetrabutylammonium perchlorate (for electrochemical analysis, ≥99.0%) and anhydrous solvents (tetrachloroethylene, hexane, toluene, propylene carbonate, and methanol) were purchased from Sigma Aldrich and used as received. Oleylamine (technical grade, 70 %) was purchased from Sigma Aldrich and purified before use by freezing, thawing, and then centrifuging to remove any insoluble solids. The purified oleylamine was dried under dynamic vacuum at 120 °C for two to three hours and stored in a nitrogen glove box.

Bis(trimethylsilyl)telluride (98 %) was purchased from Acros and stored frozen in a nitrogen glove box.

HgTe synthesis. HgTe QDs were synthesized based on a previously reported method.[33] A portion of 135 mg $HgCl_2$ (0.5 mmol, stored under N_2) and 16 mL oleylamine (OAm) were heated to 120 °C under nitrogen and briefly degassed. The solution was then put under nitrogen and cooled to the desired temperature for nanocrystal growth (70 – 120 °C, larger nanocrystals obtained at higher temperature). Meanwhile, a solution of 68 mg bis(trimethylsilyl)telluride (TMS_2Te, 0.25 mmol) in 5 mL OAm was prepared in a N_2 glove box. The TMS_2Te solution was injected into the $HgCl_2$ solution and heated at the injection temperature for 4-6 minutes. The reaction was quickly cooled by injection of 20 mL of anhydrous tetrachloroethylene (TCE) and cooled to room temperature either under ambient conditions or in a water bath. This reaction can be easily scaled up to 1 mmol HgTe by using 543 mg $HgCl_2$ (2 mmol), 50 mL OAm, 274 mg TMS_2Te (1 mmol) in 10 mL OAm, and 40 mL TCE. To synthesize HgTe QDs larger than 11 nm, the $HgCl_2$ to TMS_2Te molar ratio was increased to 4:1. Up to 13 nm, the other reaction conditions were maintained, but for larger QDs, additional TMS_2Te (half an equivalent) was diluted in OAm and added dropwise after the initial growth. The temperature was maintained for two minutes after the TMS_2Te addition, and then the reaction was quenched with TCE. *[Note: Some elemental mercury is produced during this reaction. Prolonged evacuation at elevated temperature or heating above 120 °C produces more elemental mercury.]*

Purification and storage of the HgTe QDs were performed in a nitrogen glove box. The QDs were isolated by addition of methanol nonsolvent and centrifugation. The QDs were further washed twice by dissolution into toluene plus 5 vol% OAm and precipitation with methanol and

centrifugation. Improved monodispersity could be achieved by size-selective precipitation, where methanol or ethanol nonsolvent was gradually added and particles with smaller diameter were successively removed by centrifugation. The resulting QDs were dispersed in TCE for optical measurements.

*Optical absorption***.** UV-vis-NIR spectra were collected with a Cary 5000 spectrophotometer. Infrared spectra were collected with a Thermo Nexus 670 FTIR in transmission mode using a sandwich cell with CaF_2 windows and a 0.5 mm pathlength. Spectra for oxidized NCs were obtained by adding ~20 µL of 0.05 M I_2 solution in TCE to a concentrated NC solution (~10 mg/mL) and measuring either immediately or within a few hours. Longer wait times after iodine addition led to less oxidized samples and/or etching of the NCs.

Transmission electron microscopy (TEM). TEM images were obtained on an FEI Technai F30 microscope at 300 kV. Superlattices were prepared by the tilted evaporation method, where a NC solution in TCE is slowly evaporated over a tilted carbon-coated copper TEM grid.[50]

Small-angle x-ray scattering (SAXS). SAXS measurements were conducted at the XSD-CMS 12-ID-B beamline at the Advanced Photon Source, Argonne National Laboratory. The beamline energy was fixed at 13.3 keV. SAXS measurements were also collected on a SAXSLab Ganesha in-house instrument using Cu Kα radiation. The SAXS curves were analyzed by fitting a quantitative model in Igor Pro using the Irena package (available at http://usaxs.xray.aps.anl.gov/staff/ilavsky/irena.html).[51] The scattering curves were fit in the particle size distribution module using the model-free Maximum Entropy approach. Based on

TEM data, the particles' form factor was assumed to be that of a sphere with an aspect ratio of 1. The extracted size distributions were further fit with symmetric Gaussians.

Spectroelectrochemistry. HgTe QD solutions in TCE were dropcast on Au interdigitated electrodes (IDE), crosslinked with a 1:1:50 solution of ethanedithiol (EDT) / HCl / isopropanol (IPA), and rinsed with IPA. The IDE is on glass with spacing d = 20μm and finger width d_0 = 10 μm. The spectroelectrochemical cell was assembled and filled with 0.1M tetrabutylammonium perchlorate (TBAP) / propylene carbonate (PC) in air. The sample electrode was pressed lightly against the KBr window of the cell to minimize the infrared absorption from the electrolyte. Then the cell was put in the Fourier transform infrared spectrometer (Nicolet Magna IR 550). After flushing with N_2 for several hours, infrared spectra were measured in reflectance. We first characterized the cyclic voltammetry and the film conductance with a bi-potentiostat. Then, we set the potential at the minimum conductance position where the QDs are undoped. The undoped spectrum was taken as the background. Spectra at other potentials were taken with respect to the undoped spectrum. All preparation and measurements were done at room temperature.

Theory methods. We have performed atomistic tight-binding electronic structure calculations following the methodology described in Ref. 38.[38] The single-particle tight-binding Hamiltonian matrix is written in a basis of $sp^3d^5s^*$ orbitals (for the two spin orientations) on each Hg or Te atom. We employ the tight-binding parameters that describe HgTe at 300K. The surfaces of the QDs are saturated by pseudo-hydrogen atoms in order to avoid surface states. Due to the large size of the QDs, only the eigenstates in the vicinity of the bandgap region are calculated.[52] QD shapes were defined as follows:

"sphere" – sphere with radius R = 4 nm

"oblate ellipsoid" – $\frac{x^2}{a^2}+\frac{y^2}{b^2}+\frac{z^2}{c^2}=1$, $a = 0.9 * R, b = c = R/\sqrt{0.9}$, and R = 4 nm

"truncated cube" – Along each of the 8 diagonals of the cube of length D = 7.4 nm, we truncate the apex at a height $\alpha_i * D$ (i is the direction = (111), $(\bar{1}11)$...). $\alpha_i = 1$: no truncation

$$\alpha_{111} = 0.5 \qquad \alpha_{\bar{1}\bar{1}1} = 0.6$$
$$\alpha_{\bar{1}11} = 0.6 \qquad \alpha_{\bar{1}1\bar{1}} = 0.5$$
$$\alpha_{1\bar{1}1} = 0.5 \qquad \alpha_{1\bar{1}\bar{1}} = 0.6$$
$$\alpha_{11\bar{1}} = 0.6 \qquad \alpha_{\bar{1}\bar{1}1} = 0.5$$

We considered two situations where the QDs contain either one or two additional electrons. In the case of QDs charged with one electron, single-particle states can be used directly to calculate the oscillator strengths for the intraband optical transitions. For the sake of comparison with experiments, each optical transition line is broadened using a Lorentzian function L(ω)=η/((ω^2+η^2)) where η is a parameter (5 meV).

In the case of QDs containing two electrons, we calculate the two-particle states using a configuration-interaction (CI) method.[53-54] In the first step, we calculate the self-energy corrections to the single-particle energies induced by the dielectric polarization of the QD following the injection of the separate electrons. In the second step, the screened Coulomb electron-electron interaction is introduced into the two-particle Hamiltonian which is written in the basis of Slater determinants built from the tight-binding single-particle states. In the present case, it is found that the transition energies calculated using single-particle or two-particle states are very close. Correlation effects are weak because of the combination of strong quantum confinement and high dielectric screening in HgTe QDs.

4.9. Chapter 4 bibliography.

1. Hudson, M. H.; Chen, M.; Kamysbayev, V.; Janke, E. M.; Lan, X.; Allan, G.; Delerue, C.; Lee, B.; Guyot-Sionnest, P.; Talapin, D. V., Conduction Band Fine Structure in Colloidal HgTe Quantum Dots. *ACS Nano* **2018,** *12*, 9397-9404.

2. Oh, N.; Kim, B. H.; Cho, S.-Y.; Nam, S.; Rogers, S. P.; Jiang, Y.; Flanagan, J. C.; Zhai, Y.; Kim, J.-H.; Lee, J.; Yu, Y.; Cho, Y. K.; Hur, G.; Zhang, J.; Trefonas, P.; Rogers, J. A.; Shim, M., Double-Heterojunction Nanorod Light-Responsive LEDs for Display Applications. *Science* **2017,** *355*, 616-619.

3. Zhang, H.; Chen, S.; Sun, X. W., Efficient Red/Green/Blue Tandem Quantum-Dot Light-Emitting Diodes with External Quantum Efficiency Exceeding 21%. *ACS Nano* **2018,** *12*, 697-704.

4. Mashford, B. S.; Stevenson, M.; Popovic, Z.; Hamilton, C.; Zhou, Z.; Breen, C.; Steckel, J.; Bulovic, V.; Bawendi, M.; Coe-Sullivan, S.; Kazlas, P. T., High-Efficiency Quantum-Dot Light-Emitting Devices with Enhanced Charge Injection. *Nat. Photonics* **2013,** *7*, 407.

5. Semonin, O. E.; Luther, J. M.; Choi, S.; Chen, H.-Y.; Gao, J.; Nozik, A. J.; Beard, M. C., Peak External Photocurrent Quantum Efficiency Exceeding 100% *via* MEG in a Quantum Dot Solar Cell. *Science* **2011,** *334*, 1530-1533.

6. Lan, X.; Voznyy, O.; García de Arquer, F. P.; Liu, M.; Xu, J.; Proppe, A. H.; Walters, G.; Fan, F.; Tan, H.; Liu, M.; Yang, Z.; Hoogland, S.; Sargent, E. H., 10.6% Certified Colloidal Quantum Dot Solar Cells *via* Solvent-Polarity-Engineered Halide Passivation. *Nano Lett.* **2016,** *16*, 4630-4634.

7. Du, J.; Du, Z.; Hu, J.-S.; Pan, Z.; Shen, Q.; Sun, J.; Long, D.; Dong, H.; Sun, L.; Zhong, X.; Wan, L.-J., Zn–Cu–In–Se Quantum Dot Solar Cells with a Certified Power Conversion Efficiency of 11.6%. *J. Am. Chem. Soc.* **2016,** *138*, 4201-4209.

8. Wu, K.; Li, H.; Klimov, V. I., Tandem Luminescent Solar Concentrators Based on Engineered Quantum Dots. *Nat. Photonics* **2018,** *12*, 105-110.

9. Coropceanu, I.; Bawendi, M. G., Core/Shell Quantum Dot Based Luminescent Solar Concentrators with Reduced Reabsorption and Enhanced Efficiency. *Nano Lett.* **2014,** *14*, 4097-4101.

10. Liu, W.; Chang, A. Y.; Schaller, R. D.; Talapin, D. V., Colloidal InSb Nanocrystals. *J. Am. Chem. Soc.* **2012,** *134*, 20258-20261.

11. Murray, C. B.; Sun, S.; Gaschler, W.; Doyle, H.; Betley, T. A.; Kagan, C. R., Colloidal Synthesis of Nanocrystals and Nanocrystal Superlattices. *Ibm J Res Dev* **2001,** *45*, 47-56.

12. Deng, Z.; Jeong, K. S.; Guyot-Sionnest, P., Colloidal Quantum Dots Intraband Photodetectors. *ACS Nano* **2014,** *8*, 11707-11714.

13. Keuleyan, S. E.; Guyot-Sionnest, P.; Delerue, C.; Allan, G., Mercury Telluride Colloidal Quantum Dots: Electronic Structure, Size-Dependent Spectra, and Photocurrent Detection up to 12 μm. *ACS Nano* **2014,** *8*, 8676-8682.

14. Keuleyan, S.; Lhuillier, E.; Guyot-Sionnest, P., Synthesis of Colloidal HgTe Quantum Dots for Narrow Mid-IR Emission and Detection. *J. Am. Chem. Soc.* **2011,** *133*, 16422-16424.

15. Srivastava, V.; Janke, E. M.; Diroll, B. T.; Schaller, R. D.; Talapin, D. V., Facile, Economic and Size-Tunable Synthesis of Metal Arsenide Nanocrystals. *Chemistry of Materials* **2016,** *28*, 6797-6802.

16. Harris, D. K.; Allen, P. M.; Han, H.-S.; Walker, B. J.; Lee, J.; Bawendi, M. G., Synthesis of Cadmium Arsenide Quantum Dots Luminescent in the Infrared. *J. Am. Chem. Soc.* **2011,** *133*, 4676-4679.

17. Piepenbrock, M.-O. M.; Stirner, T.; Kelly, S. M.; O'Neill, M., A Low-Temperature Synthesis for Organically Soluble HgTe Nanocrystals Exhibiting Near-Infrared Photoluminescence and Quantum Confinement. *J. Am. Chem. Soc.* **2006,** *128*, 7087-7090.

18. Kovalenko, M. V.; Kaufmann, E.; Pachinger, D.; Roither, J.; Huber, M.; Stangl, J.; Hesser, G.; Schäffler, F.; Heiss, W., Colloidal HgTe Nanocrystals with Widely Tunable Narrow Band Gap Energies: From Telecommunications to Molecular Vibrations. *J. Am. Chem. Soc.* **2006,** *128*, 3516-3517.

19. Rogach, A.; Kershaw, S. V.; Burt, M.; Harrison, M. T.; Kornowski, A.; Eychmüller, A.; Weller, H., Colloidally Prepared HgTe Nanocrystals with Strong Room-Temperature Infrared Luminescence. *Advanced Materials* **1999,** *11*, 552-555.

20. Keuleyan, S.; Lhuillier, E.; Brajuskovic, V.; Guyot-Sionnest, P., Mid-Infrared HgTe Colloidal Quantum Dot Photodetectors. *Nat. Photonics* **2011,** *5*, 489.

21. Guyot-Sionnest, P.; Roberts, J. A., Background Limited Mid-Infrared Photodetection with Photovoltaic HgTe Colloidal Quantum Dots. *Appl. Phys. Lett.* **2015,** *107*, 253104.

22. Ackerman, M. M.; Tang, X.; Guyot-Sionnest, P., Fast and Sensitive Colloidal Quantum Dot Mid-Wave Infrared Photodetectors. *ACS Nano* **2018,** *12*, 7264-7271.

23. Tang, X.; Ackerman, M. M.; Guyot-Sionnest, P., Thermal Imaging with Plasmon Resonance Enhanced HgTe Colloidal Quantum Dot Photovoltaic Devices. *ACS Nano* **2018,** *12*, 7362-7370.

24. Wehrenberg, B. L.; Guyot-Sionnest, P., Electron and Hole Injection in PbSe Quantum Dot Films. *J. Am. Chem. Soc.* **2003,** *125*, 7806-7807.

25. Yu, D.; Wang, C.; Guyot-Sionnest, P., n-Type Conducting CdSe Nanocrystal Solids. *Science* **2003,** *300*, 1277.

26. Wang, C.; Shim, M.; Guyot-Sionnest, P., Electrochromic Nanocrystal Quantum Dots. *Science* **2001,** *291*, 2390-2392.

27. Shim, M.; Guyot-Sionnest, P., n-type Colloidal Semiconductor Nanocrystals. *Nature* **2000,** *407*, 981.

28. Rinehart, J. D.; Schimpf, A. M.; Weaver, A. L.; Cohn, A. W.; Gamelin, D. R., Photochemical Electronic Doping of Colloidal CdSe Nanocrystals. *J. Am. Chem. Soc.* **2013,** *135*, 18782-18785.

29. Schimpf, A. M.; Ochsenbein, S. T.; Buonsanti, R.; Milliron, D. J.; Gamelin, D. R., Comparison of Extra Electrons in Colloidal n-Type Al3+-Doped and Photochemically Reduced ZnO Nanocrystals. *Chem. Commun.* **2012,** *48*, 9352-9354.

30. Jeong, K. S.; Deng, Z.; Keuleyan, S.; Liu, H.; Guyot-Sionnest, P., Air-Stable n-Doped Colloidal HgS Quantum Dots. *J. Phys. Chem. Lett.* **2014,** *5*, 1139-1143.

31. Robin, A.; Livache, C.; Ithurria, S.; Lacaze, E.; Dubertret, B.; Lhuillier, E., Surface Control of Doping in Self-Doped Nanocrystals. *ACS Appl. Mater. Interfaces* **2016,** *8*, 27122-27128.

32. Deng, Z.; Guyot-Sionnest, P., Intraband Luminescence from HgSe/CdS Core/Shell Quantum Dots. *ACS Nano* **2016,** *10*, 2121-2127.

33. Shen, G.; Chen, M.; Guyot-Sionnest, P., Synthesis of Nonaggregating HgTe Colloidal Quantum Dots and the Emergence of Air-Stable n-Doping. *J. Phys. Chem. Lett.* **2017**, 2224-2228.

34. Shen, G.; Guyot-Sionnest, P., HgS and HgS/CdS Colloidal Quantum Dots with Infrared Intraband Transitions and Emergence of a Surface Plasmon. *J. Phys. Chem. C* **2016,** *120*, 11744-11753.

35. Keuleyan, S.; Kohler, J.; Guyot-Sionnest, P., Photoluminescence of Mid-Infrared HgTe Colloidal Quantum Dots. *J. Phys. Chem. C* **2014,** *118*, 2749-2753.

36. Grahn, H. T., *Introduction to Semiconductor Physics*. World Scientific: 1999.

37. Goubet, N.; Jagtap, A.; Livache, C.; Martinez, B.; Portalès, H.; Xu, X. Z.; Lobo, R. P. S. M.; Dubertret, B.; Lhuillier, E., Terahertz HgTe Nanocrystals: Beyond Confinement. *J. Am. Chem. Soc.* **2018,** *140*, 5033-5036.

38. Allan, G.; Delerue, C., Tight-Binding Calculations of the Optical Properties of HgTe Nanocrystals. *Phys. Rev. B* **2012,** *86*, 165437.

39. Murray, C. B.; Norris, D. J.; Bawendi, M. G., Synthesis and Characterization of Nearly Monodisperse CdE (E = Sulfur, Selenium, Tellurium) Semiconductor Nanocrystallites. *Journal of the American Chemical Society* **1993,** *115*, 8706-8715.

40. Li, T.; Senesi, A. J.; Lee, B., Small Angle X-ray Scattering for Nanoparticle Research. *Chem. Rev.* **2016,** *116*, 11128-11180.

41. Mattoussi, H.; Cumming, A. W.; Murray, C. B.; Bawendi, M. G.; Ober, R., Characterization of CdSe Nanocrystallite Dispersions by Small Angle X-ray Scattering. *J. Chem. Phys.* **1996,** *105*, 9890-9896.

42. Wu, L.; Lian, H.; Willis, J. J.; Goodman, E. D.; McKay, I. S.; Qin, J.; Tassone, C. J.; Cargnello, M., Tuning Precursor Reactivity toward Nanometer-Size Control in Palladium Nanoparticles Studied by *in Situ* Small Angle X-ray Scattering. *Chem. Mater.* **2018,** *30*, 1127-1135.

43. Boles, M. A.; Engel, M.; Talapin, D. V., Self-Assembly of Colloidal Nanocrystals: From Intricate Structures to Functional Materials. *Chem. Rev.* **2016,** *116*, 11220-11289.

44. Liu, H.; Keuleyan, S.; Guyot-Sionnest, P., n- and p-Type HgTe Quantum Dot Films. *J. Phys. Chem. C* **2012,** *116*, 1344-1349.

45. Allan, G.; Delerue, C., Confinement Effects in PbSe Quantum Wells and Nanocrystals. *Phys. Rev. B* **2004,** *70*, 245321.

46. de Mello Donegá, C.; Koole, R., Size Dependence of the Spontaneous Emission Rate and Absorption Cross Section of CdSe and CdTe Quantum Dots. *J. Phys. Chem. C* **2009,** *113*, 6511-6520.

47. Shim, M.; Guyot-Sionnest, P., Intraband Hole Burning of Colloidal Quantum Dots. *Phys. Rev. B* **2001,** *64*, 245342.

48. Spittel, D.; Poppe, J.; Meerbach, C.; Ziegler, C.; Hickey, S. G.; Eychmüller, A., Absolute Energy Level Positions in CdSe Nanostructures from Potential-Modulated Absorption Spectroscopy (EMAS). *ACS Nano* **2017,** *11*, 12174-12184.

49. Chen, M.; Guyot-Sionnest, P., Reversible Electrochemistry of Mercury Chalcogenide Colloidal Quantum Dot Films. *ACS Nano* **2017,** *11*, 4165-4173.

50. Bodnarchuk, M. I.; Kovalenko, M. V.; Heiss, W.; Talapin, D. V., Energetic and Entropic Contributions to Self-Assembly of Binary Nanocrystal Superlattices: Temperature as the Structure-Directing Factor. *J. Am. Chem. Soc.* **2010,** *132*, 11967-11977.

51. Jan, I.; R., J. P., Irena: Tool Suite for Modeling and Analysis of Small-Angle Scattering. *Journal of Applied Crystallography* **2009,** *42*, 347-353.

52. Niquet, Y. M.; Delerue, C.; Allan, G.; Lannoo, M., Method for Tight-Binding Parametrization: Application to Silicon Nanostructures. *Phys. Rev. B* **2000,** *62*, 5109-5116.

53. Delerue, C.; Lannoo, M., *Nanostructures: Theory and Modelling*. Springer: 2004.

54. Martin, E.; Delerue, C.; Allan, G.; Lannoo, M., Theory of Excitonic Exchange Splitting and Optical Stokes Shift in Silicon Nanocrystallites: Application to Porous Silicon. *Phys. Rev. B* **1994,** *50,* 18258-18267.

5. Progress in the molten salt synthesis of $In_{1-x}Ga_xP$ quantum dots.

5.1. Introduction to InP QDs and molten salt chemistry.

Much effort has been devoted to the development of colloidal quantum dots (QDs) as tunable emitters with narrow emission linewidths for applications as phosphors or emissive layers in display technologies.[1-2] The field has been dominated by the optimization of CdSe QDs, whose high brightness (up to ~100% quantum yield (QY)) and narrow linewidths (~20 nm) outperform the competition.[3-4] However, concerns about the toxicity of heavy metals and their use in consumer electronics have inspired the development of nontoxic alternatives to CdSe QDs.[5-6] Heavy-metal-free InP QDs have emerged as a strong competitor to CdSe QDs for applications in tunable visible light emission.[2, 7-8] InP QDs have achieved high brightness (> 90% QY) and narrow linewidths (~35 nm),[9-10] but their performance lags behind that of CdSe QDs due to several synthetic and structural problems. The covalent character of the InP lattice and the high reactivity of its synthetic precursors make the optimization of synthetic protocols difficult.[11-12] Moreover, the InP phase is highly susceptible to oxidation, which is ubiquitous in highly emissive InP QDs.[13-14] Despite these challenges, high performance InP emitters have been developed through advanced core synthesis followed by the growth of successive ZnSe and ZnS shells to yield bright, stable materials.[9-10, 15-16] Yet recent work has shown that unintentional zinc-doping of the InP core creates emissive in-gap states which broaden the ensemble photoluminescence.[17] In epitaxial materials, heterovalent doping of III-V emitters is avoided by using lattice-matched, alloyed III-V materials as wide band gap passivating layers.[18] The synthesis of sophisticated III-V core/shell materials has yet to be achieved with colloidal synthetic methods; however, there has been some initial success in the colloidal synthesis of InP/GaP/ZnS[7, 19] and InZnP/InGaP/ZnSeS[20] heterostructures with high quantum yields (> 70%).

We introduced molten salt processing as a method to overcome several persistent problems in III-V QD materials synthesis.[21-22] Molten inorganic salts are robust, high temperature solvents with a wide electrochemical window, making them an inert matrix for a variety of synthetic transformations. Recent work has shown that nanocrystals (NCs) can be dispersed in a variety of molten salts.[23-24] Specific chemical interactions between the NC surface and the salt matrix induce structuring of the molten salt ions around the NCs which prevents direct contact of the NC surfaces. Thus, NCs can be dispersed throughout the salt matrix and protected from sintering. In addition, alkali halide melts are rigorously oxygen free and have recently been used to synthesize a variety of oxidation prone ceramic materials directly in air.[25] These conditions are ideal for synthetic transformations of III-V QDs.

Recently, a method has been developed for the synthesis of III-V alloy QDs in an alkali halide molten salt matrix.[22] InP or InAs QDs synthesized by traditional colloidal techniques can be dispersed in a molten inorganic salt and transformed to $In_{1-x}Ga_xP$ or $In_{1-x}Ga_xAs$ alloyed QDs by annealing in the presence of Ga^{3+} at 380-450 °C. This cation exchange produces colloidal QDs with a higher band gap and reduced lattice constant while maintaining the size and size distribution of the initial QDs. The InP to $In_{1-x}Ga_xP$ cation exchange brings about several new properties which may be advantageous for technological applications: higher extinction coefficient, better lattice match with wide band gap ZnS shells, and improved high temperature photoluminescence.

The molten salt synthesis of $In_{1-x}Ga_xP$ QDs may be optimized to further improve the optical properties. Surface chemistry dictates the interaction between the QD surface and the molten salt matrix; thus, the choice of surface passivation may impact the stable dispersion of the QDs within the salt,[23-24] the thermodynamic favorability of cation exchange at the QD surface,[26]

and the stability of the nanocrystalline III-V phase.[27-29] Designing synthetic conditions that stabilize the QD lattice should prevent the formation of crystalline defects and impede broadening of the size distribution through ripening, improving the emission quantum yield and linewidth, respectively. Additionally, tuning the cation exchange to achieve a breadth of alloy compositions ($In_{1-x}Ga_xP$, x = 0-1) with control over cation distribution within the QD lattice would allow us to achieve novel nanostructures which mimic well-developed epitaxial structures. For instance, the creation of all III-V core shells may improve the emission quantum yield without the inclusion of heterovalent ions. To attain control over the cation exchange reaction, we seek to understand its mechanism through variation in the temperature and time of reaction as well as changes in the initial InP QD size and shape. Here, we explore the influences of surface chemistry, reaction conditions, and nanocrystal morphology on the molten salt indium-to-gallium cation exchange to develop a more thorough understanding of the cation exchange process and inform the design of optimized synthetic procedures.

5.2. Ligand exchange and molten salt dispersal of InP QDs.

Solution-processed NCs can be uniformly dispersed in a variety of molten salt media.[23-24] To form a stable dispersion, the NC surface chemistry and salt composition must be complementary to allow for chemical interactions at the surface that induce ion templating in the salt matrix. These ion correlations extend beyond the Debye length and prevent close contact of NC surfaces in the salt matrix.[24] To achieve the required surface interaction, as-synthesized NCs capped with long-chain organic ligands must undergo either ligand stripping, creating a bare nanocrystal surface,[30] or inorganic ligand exchange, passivating the surface with small inorganic

moieties.[31-34] These NCs can then be uniformly dispersed in Lewis basic molten salts, such as alkali halides and thiocyanates (Figure 5.1).[23]

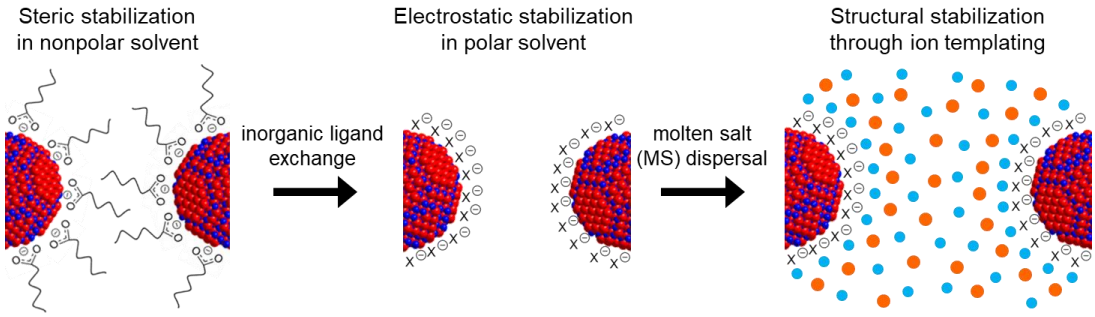

Figure 5.1. Stabilization mechanisms for QDs in various media.
Schematic illustrating the role of surface ligands in the dispersal of QDs in nonpolar solvents, polar solvents, and molten salts. Long-chain organic ligands provide stabilization in nonpolar solvents through steric repulsion, charged inorganic surface ligands provide stabilization in polar solvents through electrostatic repulsion, and chemical interactions between the NC surface and coordinating molten salts provide stabilization through ion correlations (blue: cation, orange: anion).

It has been shown that the dispersal of III-V QDs in a molten salt matrix can allow access to chemical transformations that are impossible in traditional organic media.[21-22] Molten salt annealing in the presence of excess Ga^{3+} improves the GaAs QD lattice structure by healing gallium vacancies[21] and induces indium-to-gallium cation exchange in InP and InAs QDs.[22] Previous molten salt studies were conducted primarily on III-V NCs passivated with didodecyldimethylammonium sulfide ($(DDA)_2S$). It was postulated that at the high temperature of molten salt processing (≥ 300 °C) the DDA^+ cations decompose and the salt interfaces with a sulfide-capped QD surface.[22] Here, we seek to understand the role that different surface chemistry can play in the dispersal, phase stabilization, and reactions of III-V QDs in a molten bromide matrix, focusing on InP QDs and indium-to-gallium cation exchange.

To fully understand the role of surface chemistry in the molten salt dispersal and indium-to-gallium cation exchange of InP QDs, we characterized the changes in the QD properties at

multiple stages of the synthetic process. Using a consistent batch of 3.8 nm InP QDs (small InP QDs, see Materials and Methods), we explored molten salt dispersal at 300 °C and elevated temperature annealing at 400 °C, with or without excess Ga^{3+}, for the following surface chemistries: $(DDA)_2S$, $(NH_4)_2S$, Li_2Se, $GaCl_3$, and $InCl_3$. Sulfide and selenide were chosen due to the previous success with dispersal of sulfide-capped QDs in molten salts,[21-22, 24] the ubiquity of surface chalcogenide treatments for III-V semiconductors,[35] and the established precedent for shelling InP QDs with ZnSe and ZnS.[15, 36] Sulfur is known to have relatively high diffusivity in InP at elevated temperatures[29, 37] and could impact the optical and electronic properties of InP and $In_{1-x}Ga_xP$ QDs if it diffuses into the bulk of the QD lattice.[38] To explore similar surface chemistry with a lower probability of diffusion, we studied selenide surface ligands, which should have a lower diffusion coefficient in the InP lattice due to their larger ionic radius.[39] Additionally, $GaCl_3$ and $InCl_3$ surface passivations were chosen because they will not introduce heterovalent impurities into the system.

The native organic ligands which passivate the as-synthesized InP QDs were replaced with small inorganic ligands through two-phase solution ligand exchange following reported procedures.[33-34] In brief, a dilute solution of InP QDs dispersed in nonpolar solvent (hexane or toluene) is mixed with an immiscible solution of the desired inorganic ligand in polar solvent (N,N-dimethylformamide (DMF) or formamide). The inorganic ligands replace the native ligands at the NC surface, and the NCs phase transfer into the polar solvent. Colloidal solutions of $(NH_4)_2S$ and Li_2Se-capped InP QDs in formamide and $GaCl_3$ and $InCl_3$-capped InP QDs in DMF have absorbance spectra which are nearly identical to that of the as-synthesized InP QDs, confirming that we have maintained the QD size and monodispersity (Figure 5.2). The $(NH_4)_2S$-capped InP QDs can be transferred back into toluene or hexane using

didodecyldimethylammonium bromide (DDAB) as a phase transfer agent to yield $(DDA)_2S$-capped InP QDs. Toluene and hexane serve as inert, low boiling point solvents for ease of further processing steps, and the DDA^+ should decompose through Hoffman elimination at the high temperatures of molten salt treatment (≥ 300 °C) to yield a sulfide-capped QD surface.[40]

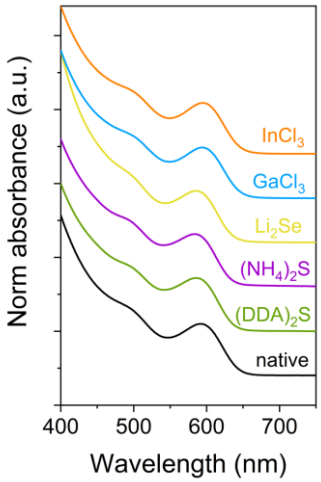

Figure 5.2. Absorbance spectra for ligand-exchanged InP QDs.
Solution absorbance spectra of as-synthesized (native) and ligand-exchanged InP QDs show near identical features for particles with different surface passivation.

The inorganic-capped InP QDs can be well-dispersed in a molten bromide eutectic composed of CsBr, LiBr, and KBr in a 25:56.1:18.9 molar ratio (melting point 236 °C). The $(NH_4)_2S$, Li_2Se, $GaCl_3$, and $InCl_3$-capped InP QDs were thoroughly dried and then combined with the bromide eutectic powder by grinding in a mortar and pestle. In contrast, the $(DDA)_2S$-capped InP QDs could be added to the bromide salt as a toluene or hexane solution followed by solvent evaporation to yield a uniform distribution of the QDs throughout the bromide salt powder. The QD/salt mixtures were heated well above the melting point of the bromide eutectic (300 °C) and stirred vigorously for 3 hours to achieve a uniform dispersion. For all of the surface ligands studied, the InP QDs distributed uniformly throughout the salt matrix (Figure 5.3).

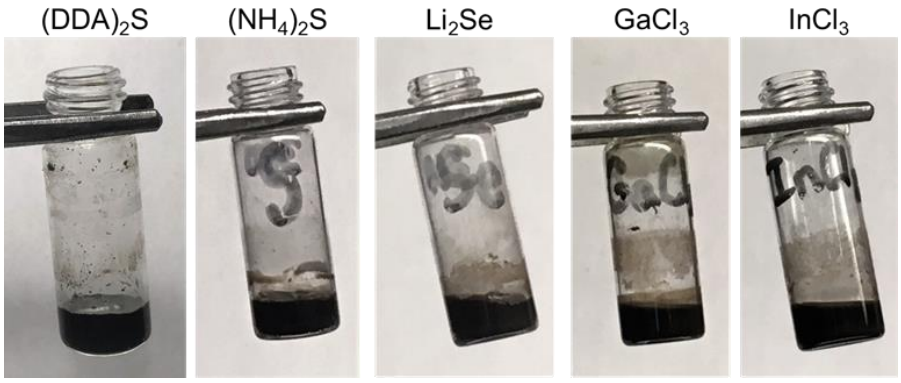

Figure 5.3. Photographs of InP QDs dispersed in molten bromide eutectic.
Photographs of uniform dispersions of InP QDs in molten bromide eutectic at 300 °C, with different surface passivations indicated.

After molten salt dispersal, the InP QDs can be recovered as a colloidal solution in nonpolar solvent. Upon cooling to room temperature, the NCs are well-dispersed in a solid bromide salt matrix. The bromide salt can be dissolved in formamide, and the QDs are isolated as a powder by centrifugation. Colloidal stability of these QDs can be regained by two different methods. In previous works, NCs have been recovered through repassivation with $(DDA)_2S$, as described above.[21-22] To avoid the surface restructuring that takes place upon sulfide exchange,[29, 38] here we instead use a combination of oleic acid and oleylamine (OA/OAm) ligands to recover colloidal stability. The salt-treated QDs regain colloidal stability when stirred in a toluene solution of OA/OAm at 50 °C for 45 minutes. The resulting QD solution can be washed with EtOH to remove excess organic ligands, and the washed particles retain colloidal stability indefinitely. For each of the QD surface passivations mentioned above, the QDs were recovered with OA/OAm after molten salt treatment; thus, the QD surface passivation mentioned in further discussion refers to the QD surface before molten salt dispersal.

Dispersal of the InP QDs in molten bromide eutectic at 300 °C induces minor changes in the QD properties which are largely independent of initial surface passivation. After molten salt

dispersal and recovery with OA/OAm, the InP QDs initially passivated with $(DDA)_2S$, $(NH_4)_2S$, $GaCl_3$, and $InCl_3$ can be quantitatively recovered as a colloidal solution in hexane or toluene. The QDs capped with Li_2Se, in contrast, have only limited colloidal stability when recovered with OA/OAm, and must be repassivated with $(DDA)_2S$ to achieve quantitative colloidal stability. We attribute this difference in dispersibility to redox reactions at the surface of the selenide-passivated QDs, for instance oxidation to produce diselenide surface species.[41] For all surface passivations studied, there is mild ripening of the InP QDs during molten salt treatment at 300 °C. This increase in particle size distribution broadens the absorbance spectra (Figure 5.4), decreasing the prominence of the excitonic features and increasing the half-width at half maximum (HWHM) of the first excitonic peak. This peak broadening is qualitatively similar for all of the studied surface chemistries. Additionally, the position of the first excitonic peak shifts after molten salt annealing at 300 °C, with redshifts observed for chalcogenide passivated InP QDs and blue shifts observed for $GaCl_3$ and $InCl_3$ passivated QDs. This can be explained either by changes in average particle size or by changes in surface chemistry which can impact the positions of the band-edge states.[42] These subtle changes in the QD size distribution and surface passivation following molten salt annealing at 300 °C are not observed in powder x-ray diffraction (XRD) patterns. For all of the studied surface passivations, the XRD patterns for the recovered InP QDs show peaks nearly identical to the initial QDs with no appreciable change in peak breadth or appearance of impurity phases (Figure 5.5).

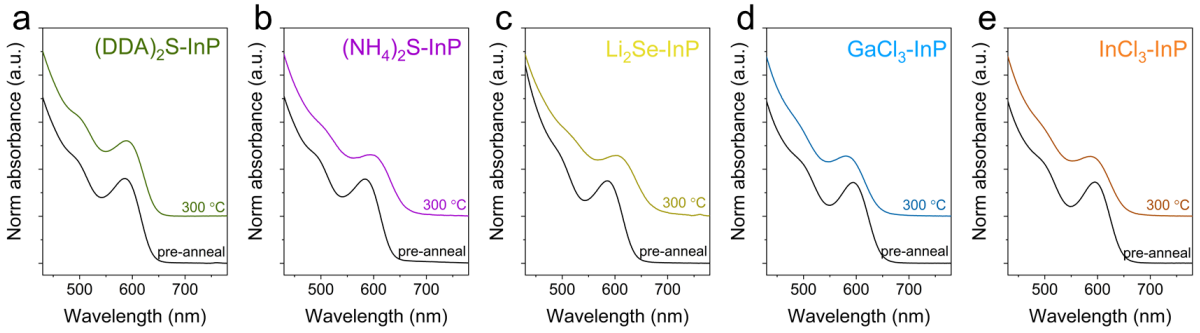

Figure 5.4. Absorbance spectra for InP QDs recovered after 300 °C molten salt (MS) anneal. Absorbance spectra for solutions of InP QDs with different initial surface passivation following molten salt dispersal at 300 °C show slightly broadened and shifted features.

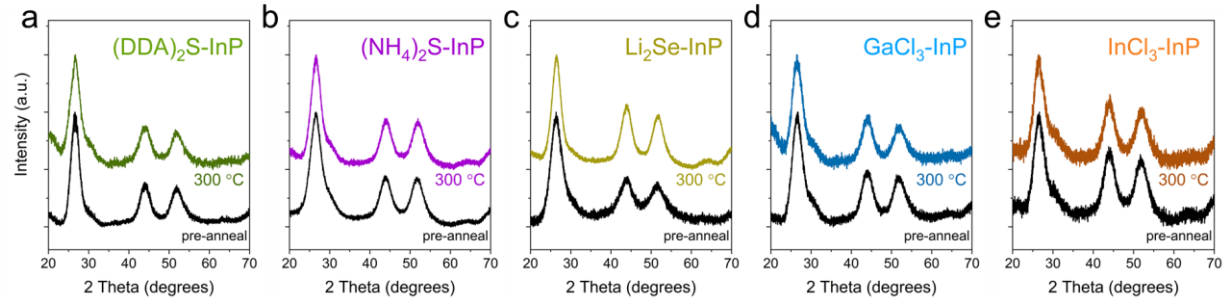

Figure 5.5. XRD patterns for InP QDs before and after 300 °C MS anneal.
Powder x-ray diffraction (XRD) patterns for InP QDs with different surface passivation before and after molten salt dispersal at 300 °C show similar peak positions and peak breadths, suggesting that the crystalline structure has not changed.

5.3. Impact of the InP QD surface chemistry during 400 °C molten salt annealing.

More pronounced changes in the InP QD structure and properties can be observed after molten salt annealing at higher temperatures. Although III-V QDs have been regarded as more robust than many other NC systems due to their resistance to ripening and grain growth at high temperatures,[43-44] the InP phase has relatively poor thermal stability due to the high vapor pressure of phosphorus above InP at elevated temperature.[45] The decomposition of bulk InP is observed around 500 °C,[46] though it can be mediated by saturating the atmosphere with phosphorus or modifying the InP surface.[28, 47-48] We can expect that the thermal decomposition

of InP will occur at lower temperatures in nanocrystalline materials due to the high surface to volume ratio.

Changes occur in the structure and properties of InP QDs annealed in molten bromide eutecitc at 400 °C, which show an interesting ligand dependence and suggest that surface ligands can tune the QD reactivity in molten salts. After dispersing the inorganic-capped InP QDs in molten bromide salt at 300 °C, the salt mixture was then annealed at 400 °C for one hour. Then the salt was dissolved and the QD powder was treated with OA/OAm as described above. For each of the surface passivations tested, only a small amount (< 5%) of the InP QDs could be recovered as a colloidal solution in toluene after molten salt annealing at 400 °C. The solution absorbance spectra were measured for the colloidal material (Figure 5.6), and the residual powders were analyzed by XRD (Figure 5.7). The XRD patterns show that the $(DDA)_2S$ and Li_2Se passivated InP QDs remain stable at high temperature, with major peaks corresponding only to nanocrytalline InP, while the $(NH_4)_2S$, $GaCl_3$, and $InCl_3$ passivated samples have peaks corresponding to both nanocrystalline InP and decomposition products (indium and In_2S_3) due to the loss of phosphorus under these conditions.

$$4\ InP \longrightarrow 4\ In^0 + P_4\uparrow$$

$$2\ InP + 3\ (NH_4)_2S \longrightarrow In_2S_3 + 2\ PH_3\uparrow + 6\ NH_3\uparrow$$

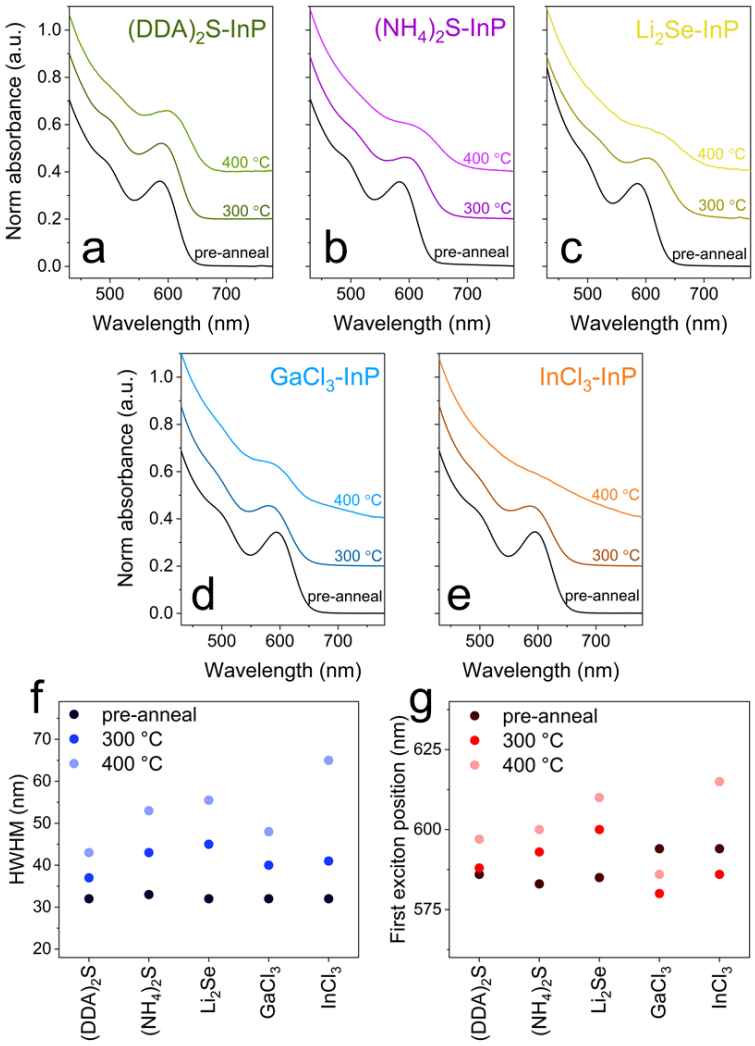

Figure 5.6. Comparison of InP QD absorbance after MS annealing at 300 and 400 °C. *(a-e)* Solution absorbance spectra for InP QDs with different initial surface chemistry before annealing in molten salt and after annealing in molten salt at 300 °C and 400 °C. Plots of the *(f)* half-width at half-maximum (HWHM) and *(g)* first excitonic peak position show similar trends in peak broadening but different trends in peak position for different surface chemistries.

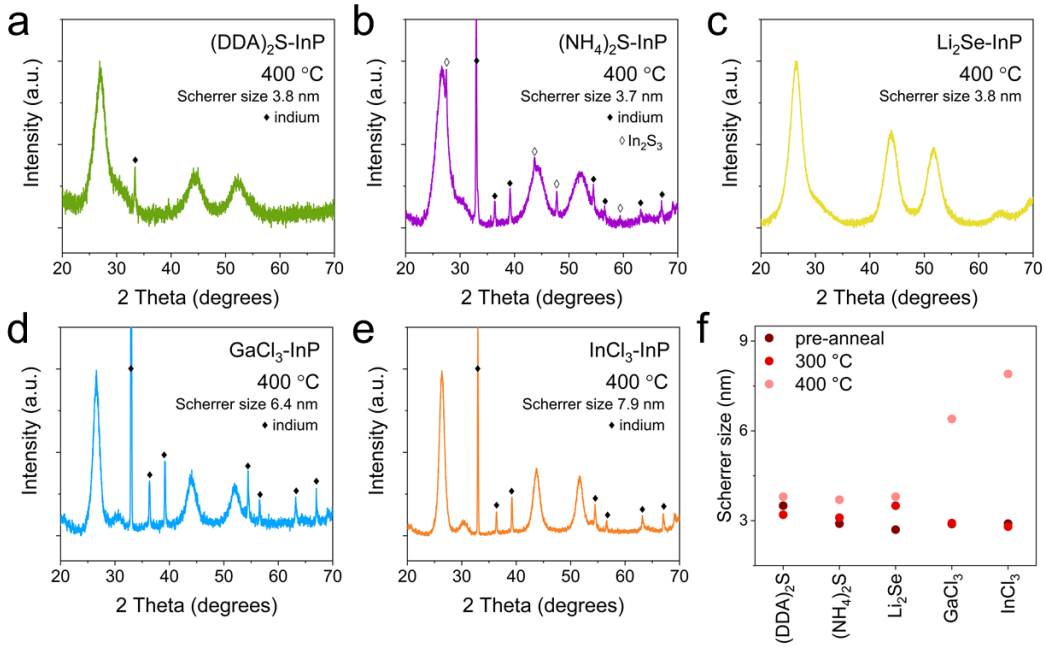

Figure 5.7. Powder XRD patterns for InP QDs after 400 °C MS anneal.
(a-e) Powder XRD patterns for InP QDs after heating at 400 °C in molten bromide eutectic. QDs passivated with *(a)* $(DDA)_2S$ and *(c)* Li_2Se show little evidence of decomposition and minimal grain growth. QDs passivated with *(b)* $(NH_4)_2S$, *(d)* $GaCl_3$, and *(e)* $InCl_3$ have impurity peaks corresponding to particle decomposition. *(f)* Scherrer sizes calculated from the XRD patterns for InP QDs following ligand exchange and molten bromide annealing at 300 °C and 400 °C. QDs passivated with $GaCl_3$ and $InCl_3$ show significant grain growth at 400 °C.

Additionally, the XRD patterns show a difference in the crystallite size for chalcogenide and metal halide passivated InP QDs following 400 °C molten bromide annealing. The InP peaks are much sharper in the patterns for the $GaCl_3$ and $InCl_3$ passivated samples following the high temperature anneal (Figure 5.7d,e); analysis of the Scherrer size for these materials suggests that they have sintered to form larger InP nanocrystallites, increasing from ~3 nm to over 6 nm in average crystallite size (Figure 5.7f). The XRD peaks for the annealed InP QDs passivated with chalcogenide ligands show a small decrease in the peak breadth, corresponding to a slight increase in the Scherrer size of these particles (~3 nm to ~3.8 nm). Absorbance spectra for the colloidal fraction of the 400 °C annealed QDs show broadening and redshifts indicative of particle ripening (Figure 5.6). This broadening is most pronounced for the QDs passivated with

$InCl_3$ and most subtle for the QDs passivated with $(DDA)_2S$, in agreement with the change in particle size predicted by XRD. Interestingly, the absorbance spectrum for the 400 °C annealed QDs passivated by $GaCl_3$ shows both a broad, red shifted onset indicative of particle ripening and a blue shifted first excitonic peak. This suggests that a portion of the $GaCl_3$ passivated particles ripened, as seen with the $InCl_3$ passivated particles, while the other particles underwent gallium cation exchange, leading to an absorbance blue shift and improved particle stability (see discussion below). The observed differences in decomposition and particle growth for the chalcogenide and metal halide capped InP QDs indicate that the initial surface ligands can play a significant role in not only the dispersibility of the QDs in the molten salt matrix but also the phase stability under harsh processing conditions.

The increased stability of chalcogenide passivated InP QDs under molten bromide annealing at 400 °C provides evidence that we can design NC surface ligands to act as surfactants at the NC/salt interface. Here, we use the IUPAC definition of surfactant to mean: *A substance which lowers the surface tension of the medium in which it is dissolved, and/or the interfacial tension with other phases, and, accordingly, is positively adsorbed at the liquid/vapor and/or at other interfaces*.[49] Based on elemental analysis of the particles recovered after 400 °C molten bromide annealing (Table 5.1), the particles initially passivated with chalcogenides retain a chalcogen-rich surface through the molten salt processing and recovery. The resulting surface shell of metal chalcogenide (In_2S_3 or In_2Se_3) has better thermal stability than InP and thus acts as a protective layer which prevents QD ripening and decomposition (Figure 5.8). The high temperature stabilization of InP surfaces with $(NH_4)_2S$ by the formation of a thin In_2S_3 layer is well documented in bulk literature,[27-29] and we expect that selenide will perform a similar function. Moreover, any physical barrier to phosphorus outgassing has been shown to improve

the temperature stability of bulk InP,[48] so this stabilization phenomenon can likely be extended to other ligand classes.

Table 5.1. Elemental chalcogen content of InP QDs after MS anneal.
Chalcogen content of the InP QDs after annealing in molten bromide eutectic and recovery with OA/OAm, as determined by inductively-coupled plasma optical emission spectroscopy (ICP-OES). The initial surface chemistry and the temperature of the MS anneal are indicated.

	S/Se mol% (ICP-OES)
$(DDA)_2S$, 300 °C	18% S
$(DDA)_2S$, 400 °C	22% S
$(NH_4)_2S$, 300 °C	22% S
$(NH_4)_2S$, 400 °C	24% S
Li_2Se, 300 °C	25% Se
Li_2Se, 400 °C	27% Se

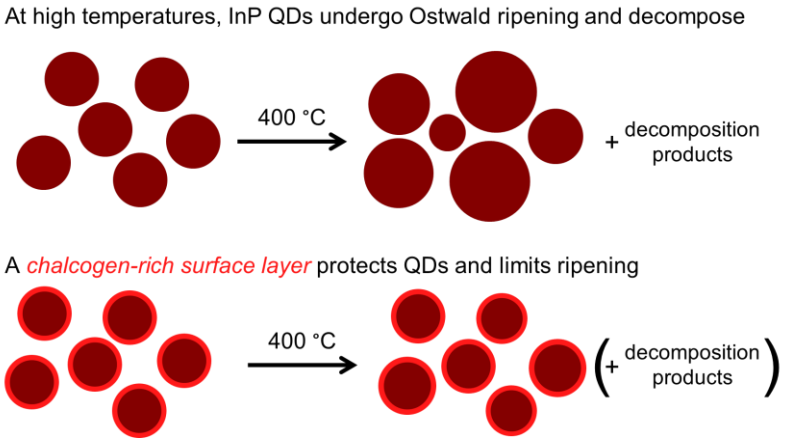

Figure 5.8. Illustration of the improved temperature stability of chalcogenide-capped InP QDs.
Schematic illustrating how chalcogenide ligands form a protective surface layer on InP QDs, which limits decomposition and grain growth at high temperatures.

The presence of indium and In_2S_3 impurity peaks in the XRD pattern for the $(NH_4)_2S$ passivated InP QDs after 400 °C annealing perhaps speaks against the claim that InP QDs are

protected by sulfide passivation. We suggest that this decomposition results from the presence of residual polysulfide species ($(NH_4)_2S_n$, $n > 1$) in the salt melt, which are known to form in the aqueous $(NH_4)_2S$ solution used for ligand exchange[50] and can be highly oxidizing.

$$2\ InP + (NH_4)_2S_n \longrightarrow In_2S_3 + (NH_4)_2S_{n-3} + 1/2\ P_4\uparrow$$

Similar decomposition is not observed for $(DDA)_2S$ passivated InP because the excess polysulfide is likely removed in further phase transfer and washing steps, while the Li_2Se passivated InP QDs are treated with high purity Li_2Se that does not contain polychalcogenides. As a control experiment, we show that InP QDs passivated with high purity Li_2S and annealed in molten bromide at 400 °C have no In_2S_3 peaks in the XRD pattern and a smaller contribution from metallic indium (Figure 5.9). Thus, the decomposition of sulfide passivated InP QDs at elevated temperature may be controlled by using Li_2S or more thorough washing of the $(NH_4)_2S$ passivated particles. We nonetheless show that the $(NH_4)_2S$ passivated particles largely maintain their particle size upon 400 °C molten bromide annealing based on the negligible change in the breadth of their InP XRD peaks.

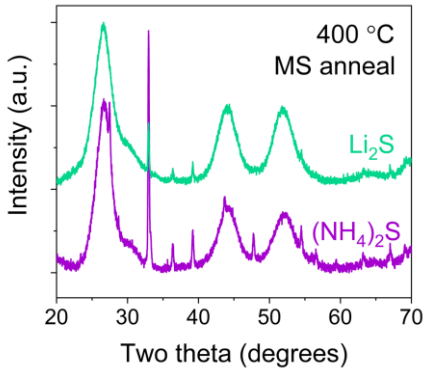

Figure 5.9. Comparison of the temperature stability of $(NH_4)_2S$ and Li_2S passivated InP QDs. Powder XRD patterns for $(NH_4)_2S$ and Li_2S passivated InP QDs after molten salt annealing at 400 °C. The $(NH_4)_2S$ passivated InP QDs decompose to form indium and In_2S_3 while the Li_2S passivated InP QDs form no In_2S_3 and less indium.

5.4. Impact of the InP QD surface chemistry on indium-to-gallium cation exchange: composition and structure.

The above studies illustrate the role that surface ligands play in the dispersion of InP QDs in molten bromide eutectic and how these surface ligands impact the high temperature stability of nanocrystalline InP. We seek to use these observations to inform the design of synthetic transformations of InP QDs in molten salt media, specifically indium-to-gallium cation exchange. A previous work has shown that $(DDA)_2S$ passivated InP QDs dispersed in molten salt undergo cation exchange to produce $In_{1-x}Ga_xP$ QDs when heated above 380 °C in the presence of excess Ga^{3+} (Figure 5.10a).[22] The extent of cation exchange controls both the lattice constant and the band gap of the resulting alloy (Figure 5.10b).[51] Thus, by controlling the QD size and alloy composition, the absorbance and emission energies as well as the lattice match with wide band gap shelling materials may be tuned. We seek to understand if changes in the surface chemistry of the initial InP QDs impact the properties of the resulting $In_{1-x}Ga_xP$ alloy QDs. For instance, the surface chemistry may influence the extent of QD ripening in the molten salt or the formation of surface trap states, thus changing the QD $In_{1-x}Ga_xP$ emission linewidth and quantum yield, respectively.

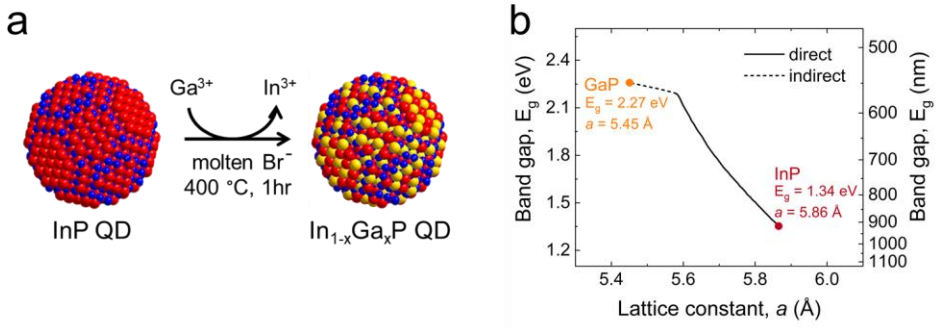

Figure 5.10. Overview of indium-to-gallium cation exchange.
(a) Schematic illustrating the indium-to-gallium cation exchange reaction in molten bromide salt. *(b)* A plot of the relationship between the band gap and lattice constant for $In_{1-x}Ga_xP$ alloys, adapted from Ref. 51.[51]

When GaI_3 is added to the molten bromide eutectic, high temperature annealing of the InP QD mixture results in indium-to-gallium cation exchange for all surface passivations tested. The $(DDA)_2S$, $(NH_4)_2S$, Li_2Se, $GaCl_3$, and $InCl_3$ passivated InP QDs were dispersed in molten bromide eutectic at 300 °C as described above. Then a stoichiometric excess of GaI_3 (~5:1 Ga:In) was added, and the salt mixture was stirred for an additional hour at 300 °C. After thorough incorporation of Ga^{3+} into the salt mixture, the QD dispersion was annealed at 400 °C for one hour. Using the OA/OAm recovery method, the QDs initially passivated with $(DDA)_2S$, $(NH_4)_2S$, or $GaCl_3$ could be quantitatively redispersed as a colloidal solution in toluene or hexane which remained stable indefinitely. The QDs initially passivated with $InCl_3$ and Li_2Se showed poorer colloidal stability following OA/OAm recovery. Powder XRD patterns for the products collected after 400 °C annealing in the presence of Ga^{3+} show broad peaks corresponding to a nanocrystalline phase with peak positions between those of InP and GaP standards, suggesting that an $In_{1-x}Ga_xP$ alloy has formed for all samples (Figure 5.11a). Successful indium-to-gallium cation exchange can also be observed by the pronounced blue shift in the absorbance onset for each of the surface passivations studied (Figure 5.11b).

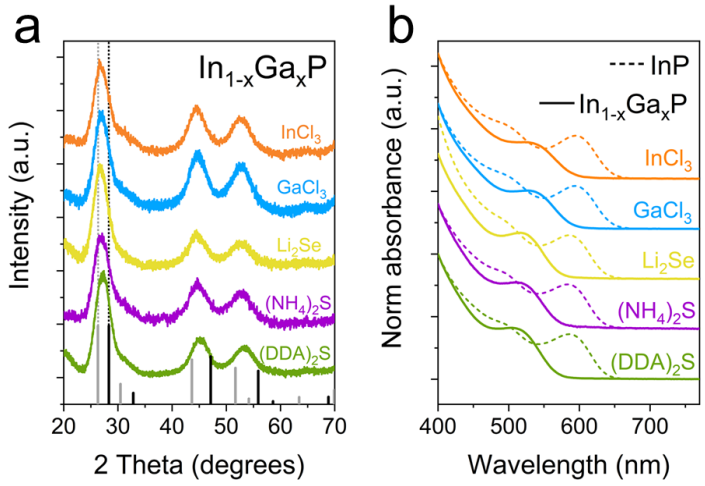

Figure 5.11. $In_{1-x}Ga_xP$ characterization for QDs with different initial surface passivation. *(a)* Powder XRD patterns for gallium-exchanged $In_{1-x}Ga_xP$ QDs with different initial surface chemistry. Standard patterns are given for InP (grey) and GaP (black). *(b)* Solution absorbance spectra for InP and $In_{1-x}Ga_xP$ QDs with different initial surface chemistries show an expected blue shift upon cation exchange.

Though differences in surface passivation show marked effects on the phase stability of InP QDs when annealed at 400 °C without Ga^{3+}, the cation exchange products resulting from different initial surface chemistries are quite similar. Powder XRD patterns for the Ga^{3+} treated material show negligible peak broadening and no impurity peaks for each of the surface passivations studied (Figures 5.11a, 5.12). Moreover, the products were much more successfully recovered as a colloid following cation exchange as compared to the poor recovery (< 5%) following the control 400 °C molten salt anneal. This indicates that the cation exchange conditions impart additional stability to the InP phase and nanocrystalline morphology. The indium-to-gallium cation exchange produces a phase with improved temperature stability; at a given temperature, the partial pressure of phosphorus above InP is higher than that above GaP.[45] In addition, surface coordination of Ga^{3+} may create stronger interactions between the QD surface and the salt matrix, causing better dispersion of the QDs in the matrix and thus preserving the QD size by preventing direct QD surface contact and sintering.[24]

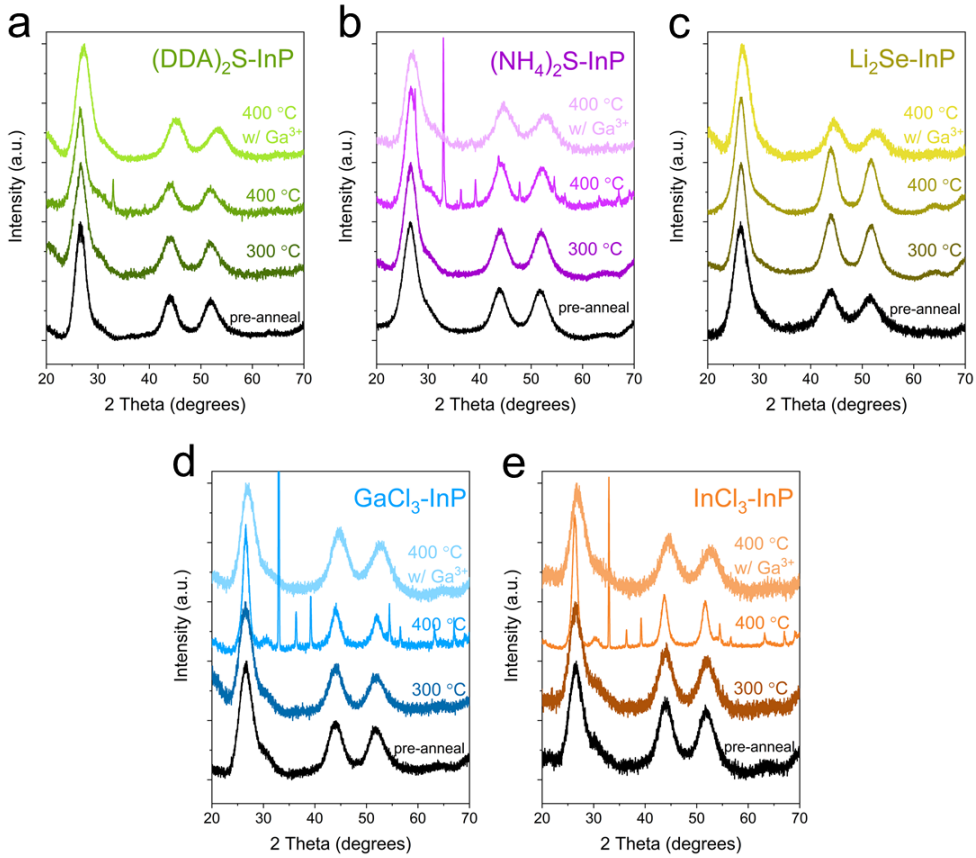

Figure 5.12. Comparison of XRD patterns for InP QDs with different surface passivations after various MS treatments.
Powder XRD patterns at various stages of ligand exchange and molten salt processing for the following surface chemistries: *(a)* $(DDA)_2S$, *(b)* $(NH_4)_2S$, *(c)* Li_2Se, *(d)* $GaCl_3$, and *(e)* $InCl_3$. Patterns are given for InP QDs following ligand exchange (pre-anneal) and after MS dispersal and recovery under the following conditions: 300 °C MS anneal, 400 °C MS anneal, and 400 °C MS anneal in the presence of excess Ga^{3+} (cation exchange conditions).

The QD morphology following cation exchange was examined using transmission electron microscopy (TEM) and small angle x-ray scattering (SAXS). TEM images of the InP QDs before cation exchange and a representative $In_{1-x}Ga_xP$ QD sample show that the particles have maintained their size and shape (Figure 5.13). We can use SAXS of the colloidal QD solutions to further quantify the particle size and size distribution before and after cation exchange.[52] Fits of the solution SAXS patterns indicate that the initial InP QDs have a diameter of 3.8 ± 0.5 nm (Figure 5.14), while the $In_{1-x}Ga_xP$ QD diameters decrease to 3.3-3.5 nm with a

slight increase in polydispersity (Figure 5.15, Table 5.2). Since GaP (a = 5.4505 Å) has a smaller lattice constant than InP (a = 5.8687 Å), we expect the particle volume to decrease due to lattice contraction upon cation exchange. Based on SAXS data, we do not observe a significant difference in $In_{1-x}Ga_xP$ QD size or polydispersity as a function of the initial surface ligand.

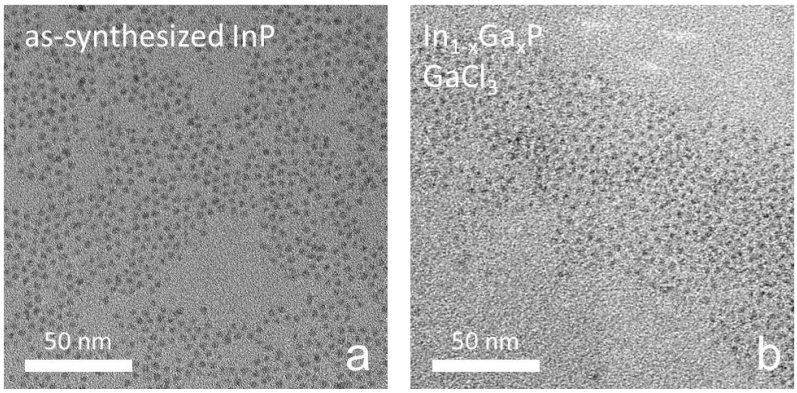

Figure 5.13. TEM images of small InP and $In_{1-x}Ga_xP$ QDs.
Representative TEM images of *(a)* as-synthesized small InP QDs and *(b)* $In_{1-x}Ga_xP$ QDs following molten salt cation exchange, initially passivated with $GaCl_3$.

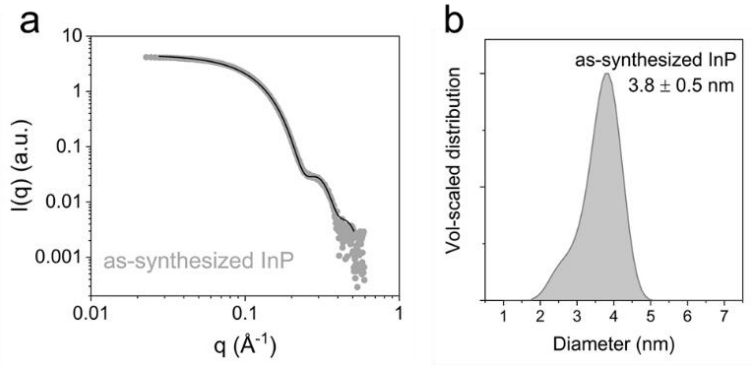

Figure 5.14. Small-angle x-ray scattering (SAXS) data for small InP QDs.
(a) Small-angle x-ray scattering (SAXS) data (grey dots) and a maximum-entropy fit (black line) for a solution of as-synthesized InP QDs. *(b)* Volume-scaled size distribution of InP QDs obtained from a maximum-entropy fit to the SAXS data.

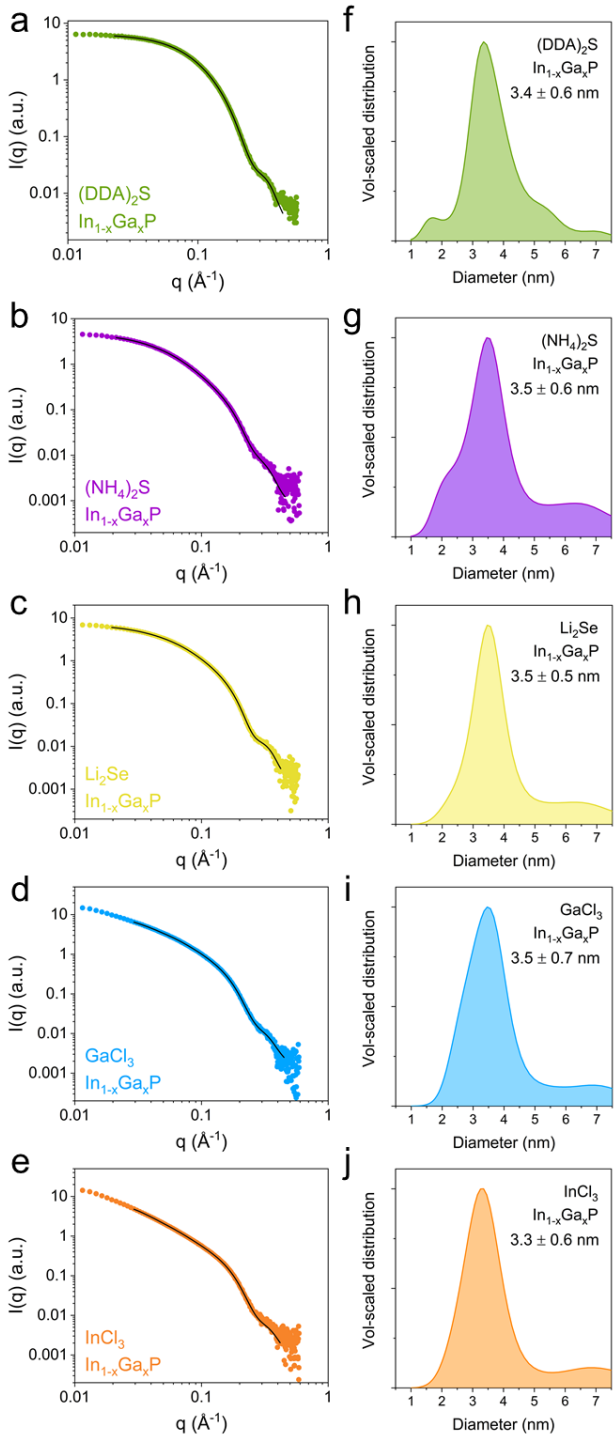

Figure 5.15. SAXS data for $In_{1-x}Ga_xP$ QDs with different surface passivations.
Small-angle x-ray scattering (SAXS) data (colored dots) and maximum-entropy fits (black lines) for solutions of recovered $In_{1-x}Ga_xP$ QDs with the following initial surface chemistries: *(a)* $(DDA)_2S$, *(b)* $(NH_4)_2S$, *(c)* Li_2Se, *(d)* $GaCl_3$, and *(e)* $InCl_3$. *(f-j)* Volume-scaled size distributions for $In_{1-x}Ga_xP$ QDs obtained from a maximum-entropy fit to the SAXS data. Size distributions given correspond to a Gaussian fit to the most intense peak.

Table 5.2. $In_{1-x}Ga_xP$ QD diameters for samples with different surface passivations.
$In_{1-x}Ga_xP$ QD diameters and standard deviations calculated from fits to small angle x-ray scattering (SAXS) patterns. The initial surface chemistry of the particles is indicated.

	$In_{1-x}Ga_xP$ QD diameter (nm)
$(DDA)_2S$	3.4 ± 0.6
$(NH_4)_2S$	3.5 ± 0.6
Li_2Se	3.5 ± 0.5
$GaCl_3$	3.5 ± 0.7
$InCl_3$	3.3 ± 0.6

The extent of indium-to-gallium cation exchange for each of the surface ligands can be estimated based on shifts in powder XRD, absorbance, and emission peaks as well as elemental analysis. For an alloy QD with the composition $In_{1-x}Ga_xP$, the XRD peak positions shift to higher angles and the absorbance and emission peaks shift to higher energies with increasing gallium content, *x* (Figure 5.10b). We can estimate the composition of an $In_{1-x}Ga_xP$ sample using Vegard's Law, where the change in lattice constant as a function of changing composition is assumed to be linear (see Materials and Methods). Based on the measured lattice constant, the composition of the $In_{1-x}Ga_xP$ QDs varies significantly with changes in the initial surface ligand, x = 0.27-0.48 (Figures 5.11a, 5.16). In contrast, the elemental analysis obtained using ICP-OES suggests both a closer similarity in composition for $In_{1-x}Ga_xP$ samples with different surface ligands and also a higher extent of cation exchange, x = 0.58-0.63 (Figure 5.16, Table 5.3). Moreover, the differences in the absorbance onset energy as a function of surface passivation do not correlate to the changes in composition as measured by XRD (Figures 5.11b, 5.22a; see further discussion below). Therefore, we suggest that under our experimental conditions the $In_{1-x}Ga_xP$ QD composition is more accurately predicted by elemental analysis than XRD. Based on

elemental analysis, there are only slight differences in the gallium incorporation for $In_{1-x}Ga_xP$ QDs with different surface passivation. The differences in alloy composition can be attributed to small variations in experimental conditions (*e.g.*, heating and cooling rates) and do not clearly indicate systematic differences in the extent of cation exchange with different surface ligands.

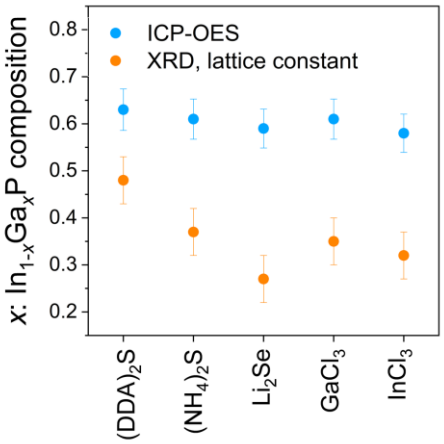

Figure 5.16. Comparison of the $In_{1-x}Ga_xP$ QD compositions estimated by XRD and elemental analysis.
Compositions for $In_{1-x}Ga_xP$ QDs with different initial surface chemistries, calculated from elemental analysis (ICP-OES) and the measured lattice constant from XRD.

Table 5.3. Elemental analysis for $In_{1-x}Ga_xP$ QDs with different surface passivations.
$In_{1-x}Ga_xP$ QD compositions as determined by inductively-coupled plasma optical emission spectroscopy (ICP-OES). The initial surface chemistry of the particles is noted.

	$In_{1-x}Ga_xP$ composition, *x*
$(DDA)_2S$	0.63
$(NH_4)_2S$	0.61
Li_2Se	0.59
$GaCl_3$	0.61
$InCl_3$	0.58

The discrepancies between the $In_{1-x}Ga_xP$ QD alloy compositions estimated by XRD and those measured by elemental analysis can be explained by the impact of surface chemistry on the nanocrystalline lattice and by heterogeneous cation exchange. Changes in the surface coordination of small NCs can induce lattice strain[53-55] which impacts the position and breadth of XRD peaks. Here, we observe small changes in the XRD peak positions of ligand exchanged InP QDs before molten salt dispersal due to differences in the QD surface passivation (Table 5.4). Thus, the measured XRD peak positions of the $In_{1-x}Ga_xP$ QDs are a convolution of surface passivation and lattice composition, which may cause the wide variation in composition predicted by XRD in contrast to the narrow range of compositions measured by elemental analysis. The much higher gallium incorporation indicated by elemental analysis that is not reflected in the measured lattice constant suggests the formation of a heterogeneous alloy structure rather than a solid solution. The 3.5 nm diameter QDs used in this study have approximately 30% of their atoms at the surface. Thus, one can imagine that changes in the surface chemistry may dramatically change the QD composition with only a minor impact on the lattice constant. For example, if a monolayer of metal-rich InP exchanges to GaP, the elemental composition could be up to 30% gallium, while the XRD pattern would show only minor changes resulting primarily from surface strain rather than bulk lattice reorganization. Previous studies of ion exchange in semiconductors suggest that ion exchange at the surface occurs quickly while diffusion limits the rate of ion exchange in the bulk.[26] Self-diffusion of metal ions in InP and GaP is known to be very slow at the temperature of our cation exchange reaction,[37, 56] and though we can expect faster diffusion in a nanocrystalline material,[57-58] we still expect that diffusion into the bulk is the slowest step in indium-to-gallium cation exchange. Therefore, the discrepancy in the $In_{1-x}Ga_xP$ compositions determined by elemental analysis and XRD indicate

that under our reaction conditions we have not formed an equilibrium solid solution but have rather formed a kinetically trapped heterogeneous alloy. Given that $In_{1-x}Ga_xP$ forms a solid solution in all compositions,[59] we expect that experimental conditions can be modified to achieve homogenous $In_{1-x}Ga_xP$ QDs.

Table 5.4. XRD peak analysis for InP and $In_{1-x}Ga_xP$ QDs with different surface passivations. Peak positions for the (111) peak in powder XRD patterns for the ligand-exchanged InP QDs and the $In_{1-x}Ga_xP$ QDs following cation exchange. The change in the position of the (111) peak with cation exchange is given as "Peak shift." The initial surface chemistry of the InP QDs is noted.

	InP (111) (degrees 2θ)	$In_{1-x}Ga_xP$ (111) (degrees 2θ)	Peak shift (degrees 2θ)
$(DDA)_2S$	26.65°	27.25°	0.6
$(NH_4)_2S$	26.55°	27°	0.45
Li_2Se	26.4°	26.8°	0.4
$GaCl_3$	26.6°	27°	0.4
$InCl_3$	26.55°	26.9°	0.35

5.5. Impact of the InP QD surface chemistry on indium-to-gallium cation exchange: optical properties.

In addition to the influence of surface passivation on the phase stability and extent of cation exchange, we sought to understand its impact on the optical properties of the resulting $In_{1-x}Ga_xP$ QDs. The absorbance spectra for the $In_{1-x}Ga_xP$ QDs with different surface passivations look broadly similar. Each cation exchanged sample shows a significant blue shift of the absorbance onset due to the increased band gap of the alloy and a decrease in the excitonic peak prominence (Figures 5.11b). The poor resolution of the excitonic features can be partially attributed to an increase in particle polydispersity. Additional broadening likely results from heterogeneity of the $In_{1-x}Ga_xP$ alloy composition across individual particles of the ensemble.

The photoluminescence (PL) spectra for $In_{1-x}Ga_xP$ QDs also show a pronounced blue shift upon cation exchange, confirming the increased band gap with gallium incorporation (Figure 5.17). After recovery with OA/OAm, the $In_{1-x}Ga_xP$ QDs have weak PL (< 1% quantum yield) with a band-edge peak at 560-580 nm and a very broad red peak, which can be attributed to surface trap emission.[60] The PL efficiency is higher for $In_{1-x}Ga_xP$ QDs recovered with $(DDA)_2S$; however, we sought to avoid surface restructuring by $(NH_4)_2S_n$ in our recovery process.[29, 38] Instead, we increased the quantum yield of the OA/OAm recovered $In_{1-x}Ga_xP$ QDs using airfree treatment with dilute HF and visible light (Figure 5.18).

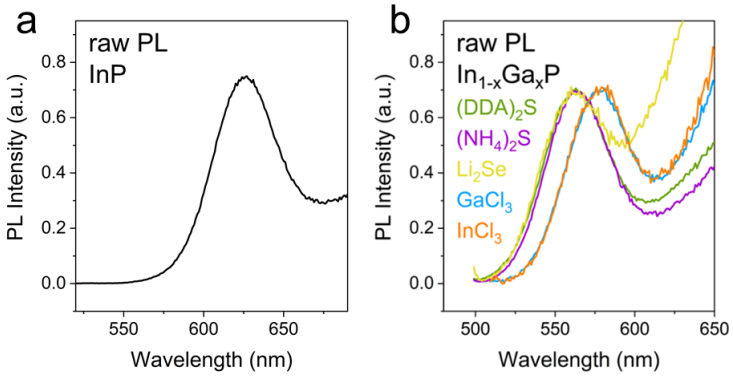

Figure 5.17. Raw photoluminescence (PL) data for small InP QDs and $In_{1-x}Ga_xP$ QDs with different surface passivation.
Photoluminescence spectra for solutions of *(a)* as-synthesized small InP and *(b)* OA/OAm recovered $In_{1-x}Ga_xP$ QDs with different initial surface passivations. All samples show weak PL and a broad red peak attributed to trap emission.

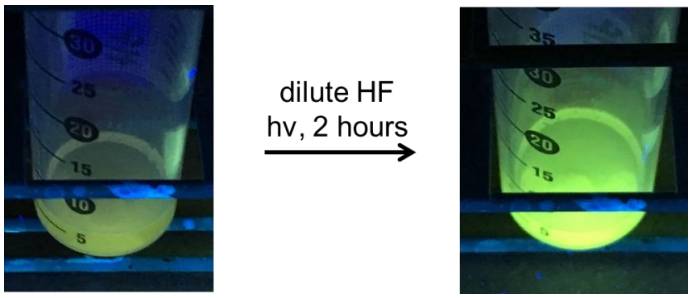

Figure 5.18. $In_{1-x}Ga_xP$ QD PL improves with HF treatment.
Treatment of $In_{1-x}Ga_xP$ QDs with dilute HF and visible light increases the PL efficiency.

Treatment of InP QDs with dilute HF accompanied by light or heat is a well-established practice for improving the PL quantum yield (QY) through surface trap passivation.[17, 42, 60-61] We chose conditions for HF treatment that increased the PL efficiency (up to ~5% QY) without significantly broadening or shifting the absorbance or emission features of the $In_{1-x}Ga_xP$ QDs (Figure 5.19, see Materials and Methods). Harsher treatment with more concentrated HF and/or oxygen exposure increased the quantum yield further (up to 20 % QY) but was accompanied by broadening and blue shifting of the absorbance and emission features, which have previously been attributed to QD oxidation and etching (Figure 5.20).[17, 61] Notably, the PL for Li_2Se passivated $In_{1-x}Ga_xP$ QDs was not improved by treatment with HF or $(DDA)_2S$. We attribute the poor PL efficiency of Li_2Se passivated $In_{1-x}Ga_xP$ QDs to persistent surface traps, which are well known for selenide-rich NC surfaces.[62-63]

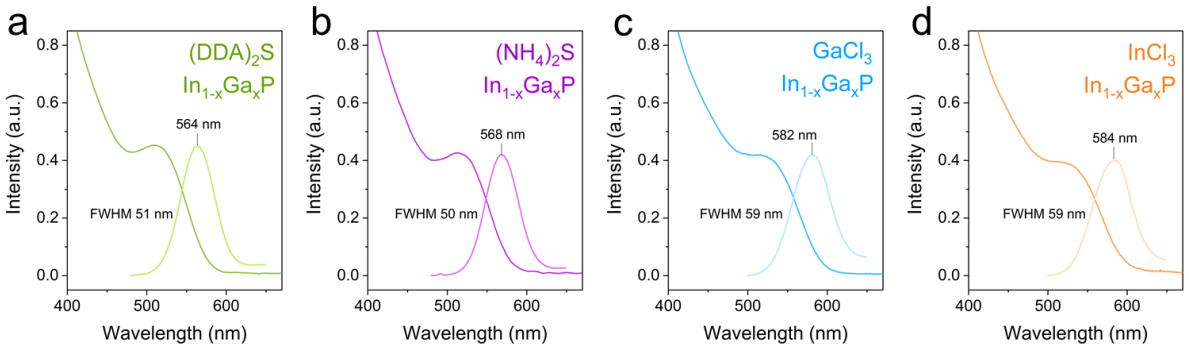

Figure 5.19. Optical characterization of $In_{1-x}Ga_xP$ QDs treated with mild HF. Absorbance and PL spectra for solutions of OA/OAm recovered $In_{1-x}Ga_xP$ QDs treated with dilute HF and visible light. The initial surface chemistries for these QDs are as follows: *(a)* $(DDA)_2S$, *(b)* $(NH_4)_2S$, *(c)* $GaCl_3$, and *(d)* $InCl_3$. $In_{1-x}Ga_xP$ QDs initially passivated by Li_2Se did not recover PL upon treatment with HF.

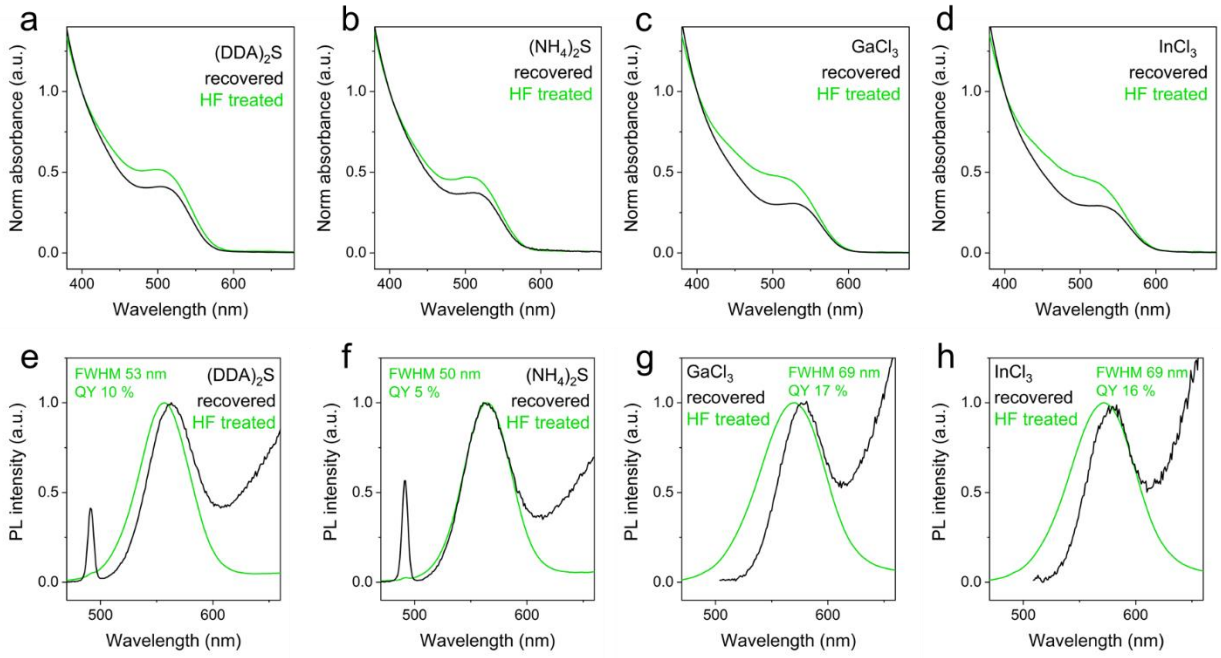

Figure 5.20. Optical characterization of $In_{1-x}Ga_xP$ QDs following harsh HF treatment. *(a-d)* Absorbance and *(e-h)* PL spectra for solutions of $In_{1-x}Ga_xP$ QDs recovered with OA/OAm before (recovered) and after treatment with 10x more concentrated HF than used in Figure 5.19. The initial surface chemistries for these QDs are as follows: *(a,e)* $(DDA)_2S$, *(b,f)* $(NH_4)_2S$, *(c.g)* $GaCl_3$, and *(d,h)* $InCl_3$. More concentrated HF improves the PL QY but also broadens and blue shifts the PL, particularly for *(g)* $GaCl_3$ and *(h)* $InCl_3$ initial surface treatments.

After cation exchange and dilute HF treatment, the PL spectra for the $In_{1-x}Ga_xP$ QDs are 40-60 meV broader than that of the initial InP QDs. The PL full-width at half maximum (FWHM) for the as-synthesized InP QDs is 155 meV and increases to 195 meV for the chalcogenide passivated $In_{1-x}Ga_xP$ QDs and 215 meV for the metal halide passivated $In_{1-x}Ga_xP$ QDs. We attribute the PL broadening to a combination of increased QD polydispersity and inhomogeneity of $In_{1-x}Ga_xP$ composition across individual QDs in the ensemble. Using photoluminescence excitation spectroscopy (PLE), we can probe the absorbance of a homogenous subset of $In_{1-x}Ga_xP$ QD emitters. For each of the ligand passivations studied, PLE spectra reveal that narrow emission bands correspond to discrete $In_{1-x}Ga_xP$ QD populations with well-defined excitonic features in their absorbance spectra (Figure 5.21). This suggests that by

optimizing synthetic conditions to achieve better control over the particle polydispersity and homogeneity of cation exchange, we may expect to achieve narrow absorbance and emission features in an ensemble of $In_{1-x}Ga_xP$ QDs.

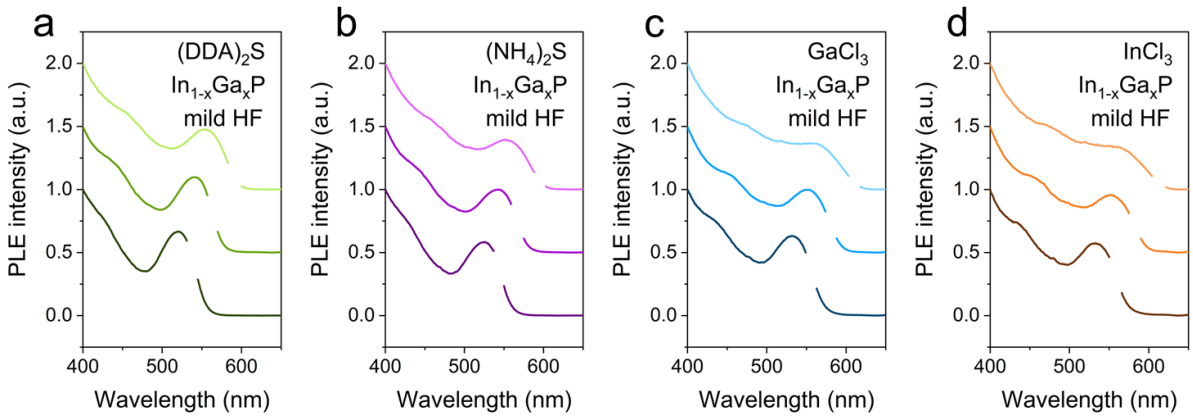

Figure 5.21. Photoluminescence excitation (PLE) spectra for $In_{1-x}Ga_xP$ QDs with different surface passivation.
Photoluminescence excitation (PLE) spectra monitored at the PL maximum, 100 meV above the PL maximum, and 100 meV below the PL maximum for solutions of $In_{1-x}Ga_xP$ QDs treated with dilute HF and visible light. The initial surface chemistries for these QDs are as follows: *(a)* $(DDA)_2S$, *(b)* $(NH_4)_2S$, *(c)* $GaCl_3$, and *(d)* $InCl_3$.

Following molten salt cation exchange, the chalcogenide and metal halide passivated QDs show a systematic difference in their band gaps which cannot be explained by gallium content or particle size. The absorbance and emission peaks for the $(DDA)_2S$, $(NH_4)_2S$, and Li_2Se passivated $In_{1-x}Ga_xP$ QDs are shifted 70-80 meV higher in energy than the peaks for $GaCl_3$ and $InCl_3$ passivated $In_{1-x}Ga_xP$ QDs (Figure 5.22). This blue shift could be rationalized by either smaller size of the chalcogenide passivated $In_{1-x}Ga_xP$ QDs, which would increase the quantum confinement, or more complete gallium incorporation for the chalcogenide passivated $In_{1-x}Ga_xP$ QDs, which would increase the band gap. However, fits to the SAXS curves for the colloidal $In_{1-x}Ga_xP$ QDs show that the chalcogenide passivated particles are equivalent in diameter to the metal halide passivated particles (Table 5.2, Figure 5.15), and elemental analysis does not

indicate a systematic difference in the extent of gallium incorporation for chalcogenide and metal halide passivated $In_{1-x}Ga_xP$ QDs (Figure 5.16, Table 5.3). We suggest that the observed difference in band gap for the chalcogenide and metal halide passivated particles can be attributed to the formation of a thin metal chalcogenide shell on the surface of the chalcogenide passivated $In_{1-x}Ga_xP$ QDs, which effectively increases the quantum confinement of these QDs without changing the size as measured by SAXS. Elemental analysis confirms that the chalcogenide passivated $In_{1-x}Ga_xP$ QDs retain ~10 mol% chalcogen throughout the molten salt cation exchange process. Thus, it is reasonable to consider the chalcogen as a shelling material rather than a ligand since it is not displaced through molten salt dispersal, gallium cation exchange, and repassivation with OA/OAm.

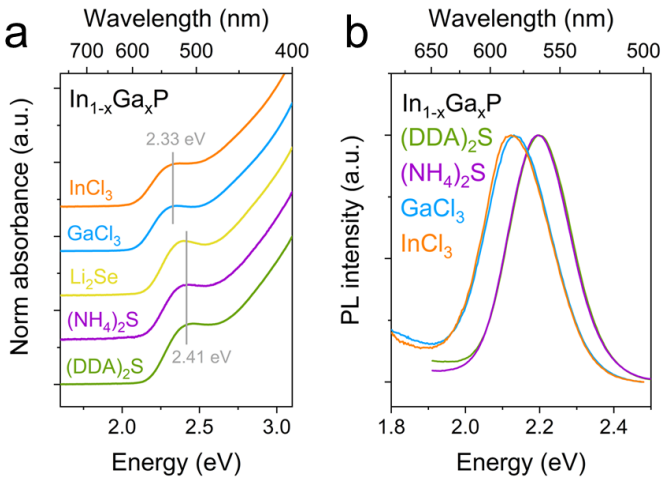

Figure 5.22. Comparison of absorbance and emission for chalcogenide and metal halide passivated $In_{1-x}Ga_xP$ QDs.
(a) Solution absorbance spectra for $In_{1-x}Ga_xP$ QDs show a difference in the first exciton position with changes in initial surface passivation. QDs initially passivated by chalcogenides shown a more pronounced blue shift upon cation exchange. *(b)* A similar difference in the peak position based on the initial surface chemistry is seen in the PL spectra of $In_{1-x}Ga_xP$ QDs treated with mild HF.

Table 5.5. Elemental analysis of the chalcogen content for $In_{1-x}Ga_xP$ QDs.
Chalcogen content of OA/OAm recovered $In_{1-x}Ga_xP$ QDs after molten salt cation exchange based on ICP-OES, with initial surface chemistry indicated.

	S/Se mol% (ICP-OES)
$(DDA)_2S$, $In_{1-x}Ga_xP$	9% S
$(NH_4)_2S$, $In_{1-x}Ga_xP$	10% S
Li_2Se, $In_{1-x}Ga_xP$	12% Se

We have shown that surface ligands play a role in the molten salt dispersal of InP QDs and impact further chemical reactions in this molten salt matrix. InP QDs can be well dispersed in molten bromide eutectic with chalcogenide or metal halide ligands. The surface chemistry for molten salt dispersal can likely be extended to other ligand classes including halides and pseudohalides,[32] pnictides,[64] and chalcogenidometallates[31] as well as ligand-stripped particles.[30] We demonstrated that chalcogenide capping ligands form a persistent chalcogen-rich shell which protects the InP QD phase at elevated temperature. Moreover, we showed that indium-to-gallium cation exchange proceeds similarly for InP QDs capped with chalcogenides and metal halides, though the chalcogen-rich shell impacts the optical properties of the $In_{1-x}Ga_xP$ QDs. Future work will explore the optimization of surface ligands to achieve enhanced particle stability and improved fluorescence.

5.6. Effects of time and temperature on indium-to-gallium cation exchange.

Additional control over the indium-to-gallium cation exchange reaction may be achieved through modulation of the reaction conditions. To design optimal synthetic conditions for this molten salt cation exchange, we must first develop a more thorough understanding of the reaction mechanism. The indium-to-gallium cation exchange proceeds through three distinct

steps (Figure 5.23). Step 1 is the diffusion of Ga^{3+} from the salt matrix to the InP QD surface. Here, we control this step by flooding the reaction with an excess of Ga^{3+} (~5:1 Ga:In molar ratio) to ensure that the QD is surrounded by a high concentration of Ga^{3+}. Step 2 is the surface exchange of In^{3+} to Ga^{3+}, governed by the thermodynamics of the following reaction:[26, 65]

$$InP + GaBr_3 \rightleftharpoons GaP + InBr_3$$

For the indium-to-gallium cation exchange, the reaction favors the creation of a GaP phase due to the higher thermodynamic stability of GaP[66] and the more favorable solvation of In^{3+} than Ga^{3+} by the soft anions in the salt matrix. Step 3 is the diffusion of Ga^{3+} into the lattice and corresponding out-diffusion of In^{3+}. The self-diffusion of In^{3+} in InP and Ga^{3+} in GaP are very slow at 400 °C, on the order of 10^{-8} nm^2/hour[56] and 10^{-14} nm^2/hour,[37] respectively, when extrapolated from high temperature data. Diffusion should be greatly accelerated in nanocrystalline materials due to their high surface to volume ratio.[57-58] Nonetheless, we expect that the cation diffusion throughout the QD is the slowest step of the cation exchange.

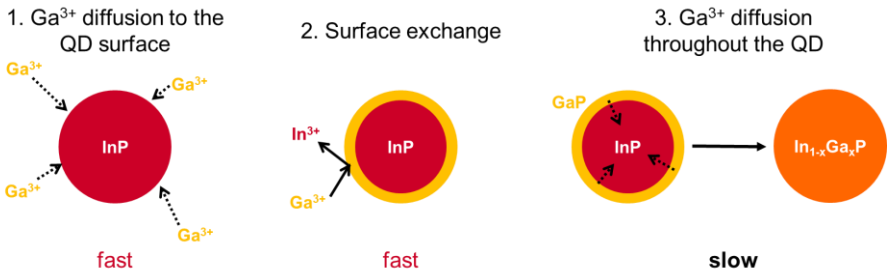

Figure 5.23. Steps of indium-to-gallium cation exchange.
Scheme depicting the steps of an InP to $In_{1-x}Ga_xP$ cation exchange reaction.

In our previous work on molten salt cation exchange of III-V QDs, we controlled the extent of cation exchange by modulation of the reaction temperature.[22] For each synthesis, a set amount of InP QDs and GaI_3 were dispersed in molten bromide eutectic and heated at elevated temperature (380-425 °C) for one hour. Higher temperatures led to more complete cation

exchange as evidenced by a more pronounced blue shift in the absorbance and emission spectra and a decrease in the lattice constant. The highest gallium incorporation ($In_{0.22}Ga_{0.78}P$) was achieved at 425 °C; however, these reaction conditions also led to QD decomposition and the $In_{1-x}Ga_xP$ QD yield was poor. Here, we seek to understand if under our reaction conditions the cation exchange reaction is thermodynamically controlled, where reaction temperature dictates an equilibrium $In_{1-x}Ga_xP$ composition, or kinetically controlled, where reaction temperature controls the cation diffusion rate and the resulting composition is a result of both reaction temperature and reaction time. Understanding and controlling these conditions may allow us to extend our repertoire of cation exchange products, *e.g.* to higher gallium incorporation or controlled heterostructures, while avoiding QD decomposition.

The dual roles of time and temperature in the indium-to-gallium cation exchange were explored by conducting cation exchange on a consistent set of InP QDs (small InP, see Materials and Methods) at two temperatures for a series of time points. The as-synthesized InP QDs were ligand exchanged to $(DDA)_2S$ and dispersed in molten bromide eutectic as described above. This surface passivation was chosen for its ease of processing. A 5x molar excess of GaI_3 was added to the salt mixture, and cation exchange was conducted at a given temperature (380 °C or 400 °C) for a set amount of time (1, 4, or 16 hours). Following cation exchange, the molten salt matrix was dissolved in warm formamide, and the QDs were redispersed as a colloidal solution in hexane or toluene with $(DDA)_2S$. For the reactions conducted at 380 °C, the products were quantitatively recovered as a colloidal solution in nonpolar solvent. However, the harsher reaction conditions at 400 °C led to some QD decomposition and formation of a non-colloidal product, which was negligible after 1 hour of reaction but whose formation increased with increasing reaction time.

Under these reaction conditions, the extent of indium-to-gallium cation exchange increases as a function of both reaction temperature and time. The absorbance and emission spectra for $In_{1-x}Ga_xP$ QDs show an increasing blue shift with longer reaction times (Figures 5.24, 5.25). The blue shift with increasing time is more pronounced for the products obtained at higher temperatures, suggesting that the cation exchange reaction is accelerated at elevated temperature. This blue shift is accompanied by successive broadening of the absorbance features, though the PL peak remains narrow for all of the $In_{1-x}Ga_xP$ QD samples (48-50 nm FWHM). The PLE spectra monitored at the PL maximum for each of the $In_{1-x}Ga_xP$ QD samples show sharp excitonic features (Figure 5.26). This indicates that the absorbance of individual emitters has not broadened significantly and the ensemble absorbance broadening observed for the $In_{1-x}Ga_xP$ QDs corresponds to size polydispersity and inhomogeneity of the alloy composition across individual $In_{1-x}Ga_xP$ QDs in the ensemble.

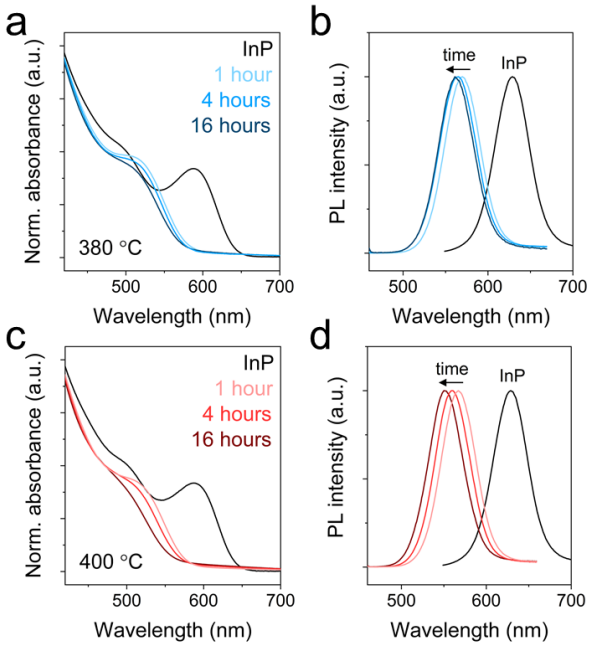

Figure 5.24. Progression of the band gap change with cation exchange reaction time. The progress of indium-to-gallium cation exchange reactions depends on both time and temperature. *(a,c)* Absorbance and *(b,d)* PL spectra for cation exchange reactions conducted at *(a,b)* 380 °C and *(c,d)* 400 °C exhibit increasing blue shifts with increasing reaction time and temperature, indicating increased gallium incorporation.

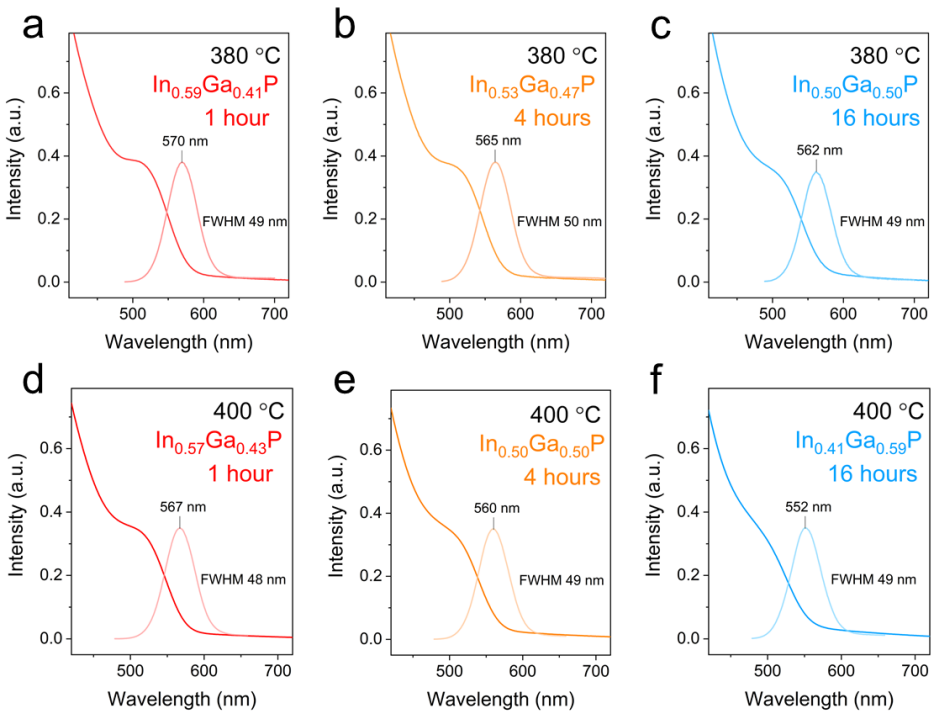

Figure 5.25. Optical characterization of small $In_{1-x}Ga_xP$ QDs under different reaction conditions.

Absorbance and PL spectra for solutions of $In_{1-x}Ga_xP$ QDs after gallium cation exchange at 380 °C for *(a)* 1 hour, *(b)* 4 hours, and *(c)* 16 hours and at 400 °C for *(d)* 1 hour, *(e)* 4 hours, and *(f)* 16 hours.

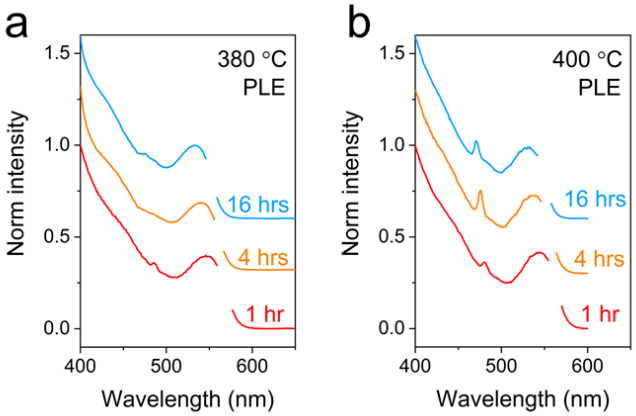

Figure 5.26. PLE spectra for small $In_{1-x}Ga_xP$ QDs under different reaction conditions.

PLE spectra monitored at the PL maximum for the 1 hour, 4 hour, and 16 hour $In_{1-x}Ga_xP$ QD samples heated at *(a)* 380 °C and *(b)* 400 °C.

The observed blue shift with increasing reaction time could be attributed either to an increased band gap due to a higher extent of indium-to-gallium cation exchange or to increased quantum confinement due to QD etching in the molten bromide matrix. To quantify the change in NC size, we measured SAXS curves for solutions of the recovered $In_{1-x}Ga_xP$ QDs. Fits to these SAXS curves reveal that the size and size distribution of the $In_{1-x}Ga_xP$ QDs are equivalent for each of the samples after cation exchange under different reaction conditions (Table 5.6; Figures 5.27, 5.28), confirming that the observed blue shift correlates to increased gallium exchange. The $In_{1-x}Ga_xP$ QDs obtained using the harshest reaction conditions (400 °C, 16 hours) show a slight decrease in the size and broadening of the size distribution; these results in concert with the observed non-colloidal product obtained in this synthesis suggest that the QD phase becomes unstable under extreme conditions.

Table 5.6. Sizes of small $In_{1-x}Ga_xP$ QDs prepared under different reaction conditions.
$In_{1-x}Ga_xP$ QD diameters and standard deviations calculated from maximum-entropy fits to the small angle x-ray scattering (SAXS) data (Figures 5.27-5.28). The temperature and reaction time for the cation exchange are noted.

	$In_{1-x}Ga_xP$ QD diameter (nm)
380 °C, 1 hour	3.2 ± 0.5
380 °C, 4 hours	3.3 ± 0.5
380 °C, 16 hours	3.2 ± 0.5
400 °C, 1 hour	3.2 ± 0.5
400 °C, 4 hours	3.2 ± 0.5
400 °C, 16 hours	3.1 ± 0.6

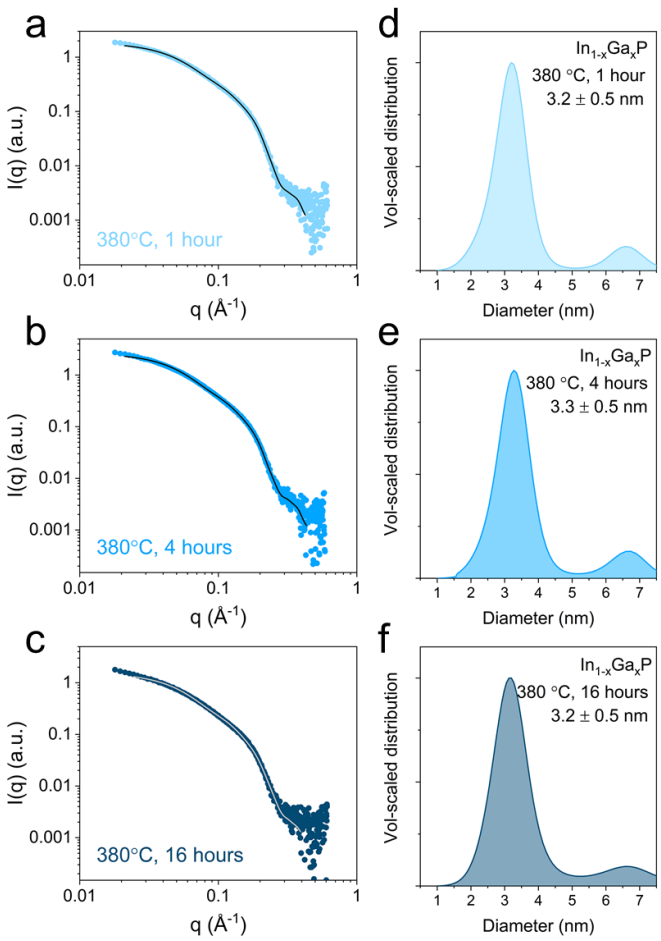

Figure 5.27. SAXS data and corresponding size distributions for $In_{1-x}Ga_xP$ QDs following 380 °C cation exchange.

Small-angle x-ray scattering (SAXS) data (colored dots) and maximum-entropy fits (black lines) for solutions of recovered $In_{1-x}Ga_xP$ QDs after cation exchange at 380 °C for *(a)* 1 hour, *(b)* 4 hours, and *(c)* 16 hours. *(d-f)* Volume-scaled size distributions of $In_{1-x}Ga_xP$ QDs obtained from a maximum-entropy fit to the SAXS data. Size distributions given correspond to a Gaussian fit to the most intense peak.

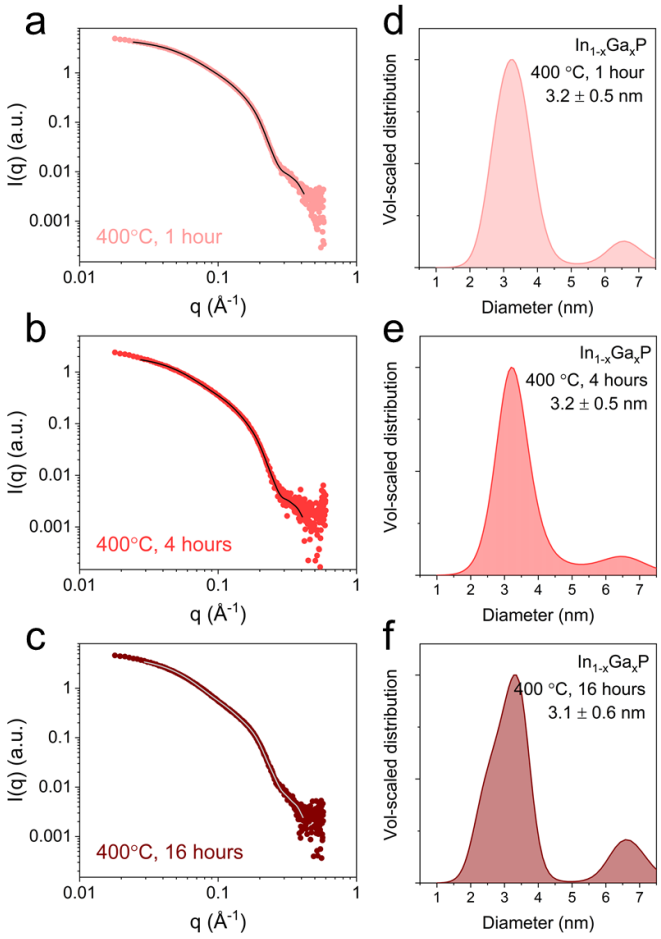

Figure 5.28. SAXS data and corresponding size distributions for $In_{1-x}Ga_xP$ QDs following 400 °C cation exchange.
Small-angle x-ray scattering (SAXS) data (colored dots) and maximum-entropy fits (black lines) for solutions of recovered $In_{1-x}Ga_xP$ QDs after cation exchange at 400 °C for *(a)* 1 hour, *(b)* 4 hours, and *(c)* 16 hours. *(d-f)* Volume-scaled size distributions of $In_{1-x}Ga_xP$ QDs obtained from a maximum-entropy fit to the SAXS data. Size distributions given correspond to a Gaussian fit to the most intense peak.

The extent of cation exchange following molten salt annealing at 380 °C and 400 °C was quantified with powder XRD and elemental analysis. The XRD pattern for each of the $In_{1-x}Ga_xP$ samples shows broad peaks indicative of a nanocrystalline zinc blende phase which shift to higher angles with increasing reaction time (Figure 5.29a). As described above, we use Vegard's law to estimate the $In_{1-x}Ga_xP$ QD composition based on the XRD peak positions. In accord with the observed optical blue shift, the $In_{1-x}Ga_xP$ QD composition becomes more gallium-rich with

increasing reaction time and temperature (Figure 5.29). Elemental analysis by ICP-OES shows a similar trend in increasing gallium incorporation with time and temperature; however, elemental analysis suggests a higher extent of cation exchange. As discussed above, we ascribe this discrepancy between the lattice constant and the elemental composition to the formation of a heterogeneous $In_{1-x}Ga_xP$ alloy with a gallium-rich surface.

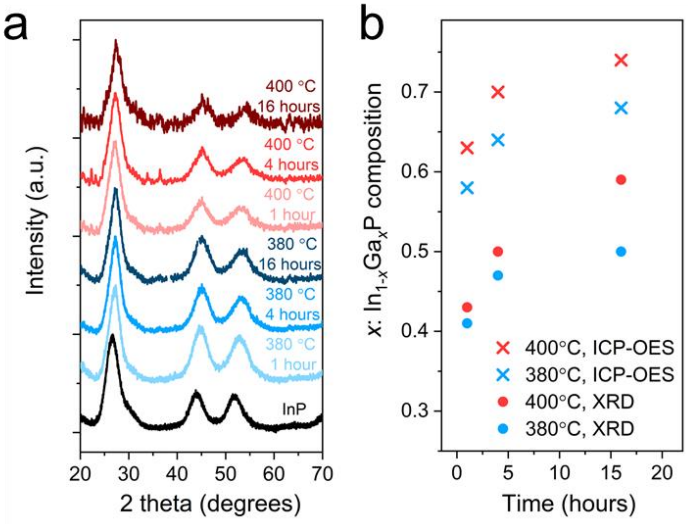

Figure 5.29. Time and temperature dependence of $In_{1-x}Ga_xP$ QD composition.
(a) Powder XRD patterns for small InP QDs before and after indium-to-gallium cation exchange at various temperatures and reaction times. *(b)* Estimated $In_{1-x}Ga_xP$ composition from the lattice constant (XRD) and elemental analysis (ICP-OES) as a function of reaction time at 380 °C and 400 °C.

The trends in gallium incorporation as a function of both time and temperature provide insight into the indium-to-gallium cation exchange reaction. At both 380 °C and 400 °C, the gallium content dramatically increases at the 1 hour and 4 hour time points and then increases at a slower rate for the 16 hour time point (Figure 5.29b). These results suggest that the indium-to-gallium cation exchange is under kinetic control at early times, and the gallium content of the recovered $In_{1-x}Ga_xP$ QDs is limited by ion diffusion throughout the lattice. The seeming composition plateau reached at later times suggests that an equilibrium composition can be

achieved for long cation exchange reactions. The more complete cation exchange observed for the higher temperature reactions at each time point indicates both faster cation exchange and an equilibrium composition with more complete gallium exchange at higher temperature. These findings show that by controlling the indium-to-gallium cation exchange temperature we can tune the equilibrium composition and by modifying the reaction time we can control the reaction progress towards this equilibrium composition. These results should prove valuable in designing reaction conditions to yield higher gallium incorporation without decomposition, precise tuning of alloy composition, and controlled formation of heterogeneous alloy QDs with a graded composition.

The diffusion limited kinetics of indium-to-gallium cation exchange observed for 3.8 nm InP QDs in a molten bromide matrix have been observed for other QD sizes and molten salt compositions. Cation exchange reactions conducted on large spherical and tetrahedral InP QDs in molten bromide eutectic, described in detail below, demonstrate very similar trends in increasing gallium incorporation as a function of reaction time (Figure 5.30). Additionally, the observed reaction mechanism is not limited to only a molten bromide environment. Cation exchange was conducted on 3.8 nm $(DDA)_2S$ passivated InP QDs dispersed in a molten iodide eutectic (KI:LiI, 37:63 mol%). The extent of cation exchange for these iodide-dispersed QDs is nearly identical to that observed for bromide-dispersed QDs under the same conditions (Figure 5.31). These results suggest that the indium-to-gallium cation exchange proceeds through a similar mechanism for a variety of InP QD morphologies and solvent environments.

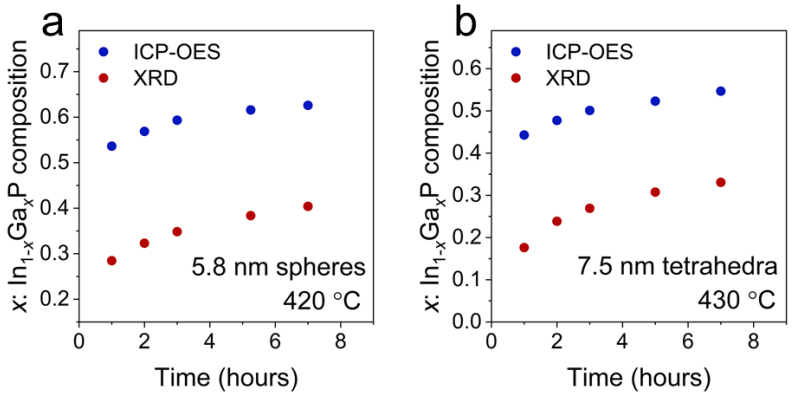

Figure 5.30. Time dependence of cation exchange for large InP QDs.
$In_{1-x}Ga_xP$ QD composition as a function of cation exchange reaction time for two sizes of InP QDs, *(a)* 5.8 nm spheres and *(b)* 7.5 nm tetrahedra. The composition was determined using elemental analysis (ICP-OES) and the lattice constant from powder XRD.

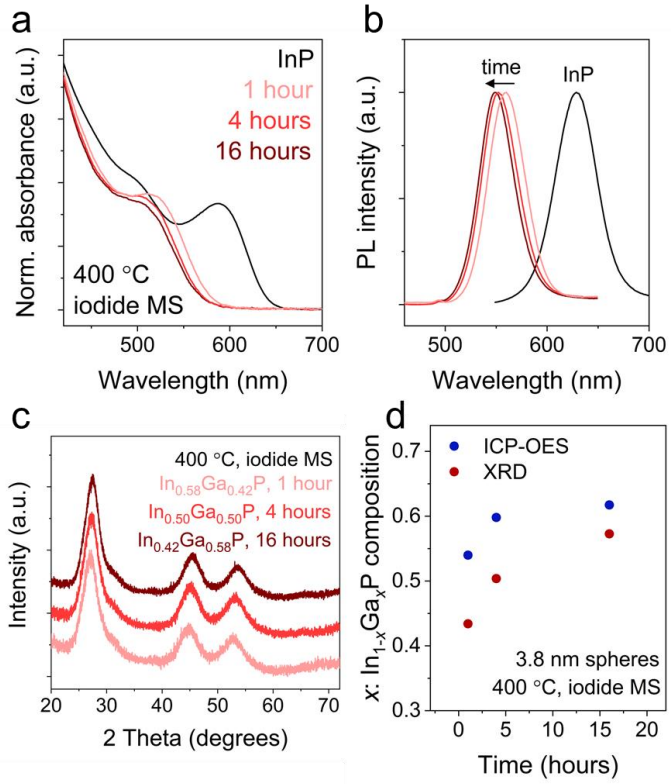

Figure 5.31. Time dependence of cation exchange for small InP QDs in an iodide molten salt.
Results for molten salt cation exchange of 3.8 nm InP QDs in an iodide eutectic at 400 °C. *(a)* Absorbance and *(b)* PL spectra show an increasing blue shift with increasing reaction time. *(c,d)* Powder XRD and *(d)* elemental analysis (ICP-OES) demonstrate an increase in the gallium content with increasing reaction time.

5.7. Extension of cation exchange methods to large InP QDs with different morphologies.

We can gain further understanding of the molten salt indium-to-gallium cation exchange through extension of the methodology to large InP QDs with different shapes and surface passivations. We synthesized large InP QDs using two well-developed synthetic methods. Spherical InP QDs with a diameter of 5.8 nm were synthesized from $InCl_3$ and $(TMS)_3P$ in trioctylphosphine (TOP) and trioctylphosphine oxide (TOPO) using the method developed by Micic *et al.*,[67] and tetrahedral InP QDs with an edge length of 7.5 nm were synthesized from $InCl_3$ and $(NMe_2)_3P$ in oleylamine following the methods developed by Hens and others.[36, 68] The surface chemistry of the InP QDs resulting from these two syntheses is quite different as can be seen from the stabilization of different surface facets resulting in different particle shapes (Figure 5.32).[69] Moreover, the oleylamine and chloride ligands can be quickly (~ 60 seconds) displaced from the surface of the tetrahedral InP QDs during inorganic ligand exchange with $(NH_4)_2S$, while the TOPO/TOP passivated spherical InP QDs undergo ligand exchange with $(NH_4)_2S$ quite slowly (overnight). By testing cation exchange on these diverse systems, we can explore the generality of the molten salt synthetic conditions for indium-to-gallium cation exchange. Additionally, the distinct shape of these two classes of particles allows us to examine the effect of molten salt cation exchange on the particle morphology.

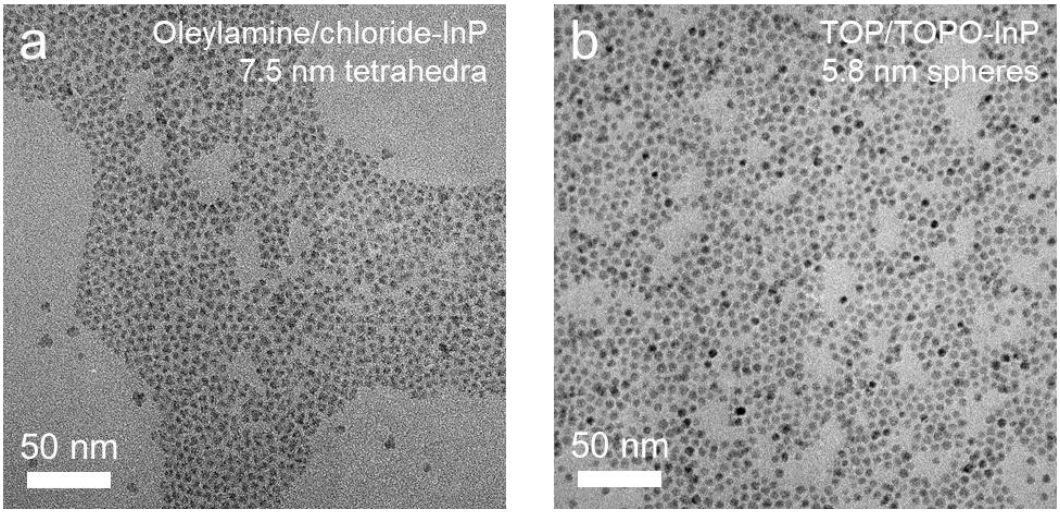

Figure 5.32. TEM images of as-synthesized large InP QDs.
TEM images reveal the distinct morphologies of (a) tetrahedral oleylamine and chloride capped InP QDs and (b) spherical TOP/TOPO capped InP QDs.

Molten salt indium-to-gallium cation exchange was accomplished for large spherical and tetrahedral InP QDs. As described above, the InP QDs were passivated with $(DDA)_2S$ and dispersed in molten bromide eutectic at 300 °C. A 5x molar excess of GaI_3 was incorporated into the salt matrix, and the mixture was annealed at 420 °C for 3 hours for the spherical particles and 7 hours for the tetrahedral particles to induce indium-to-gallium cation exchange. The $In_{1-x}Ga_xP$ QDs were isolated by washing away the salt matrix with warm formamide and were repassivated with $(DDA)_2S$ to form a colloidal solution in toluene or hexane. Successful cation exchange of both InP QD samples to form $In_{1-x}Ga_xP$ QDs is evidenced by the blue shift in the absorbance onset and the shift of the XRD peaks to higher angles indicating a decreased lattice constant (Figure 5.33). Based on the lattice constant measured with XRD, we estimate the cation exchanged QD compositions to be $In_{0.7}Ga_{0.3}P$ for the initially tetrahedral particles and $In_{0.6}Ga_{0.4}P$ for the initially spherical particles.

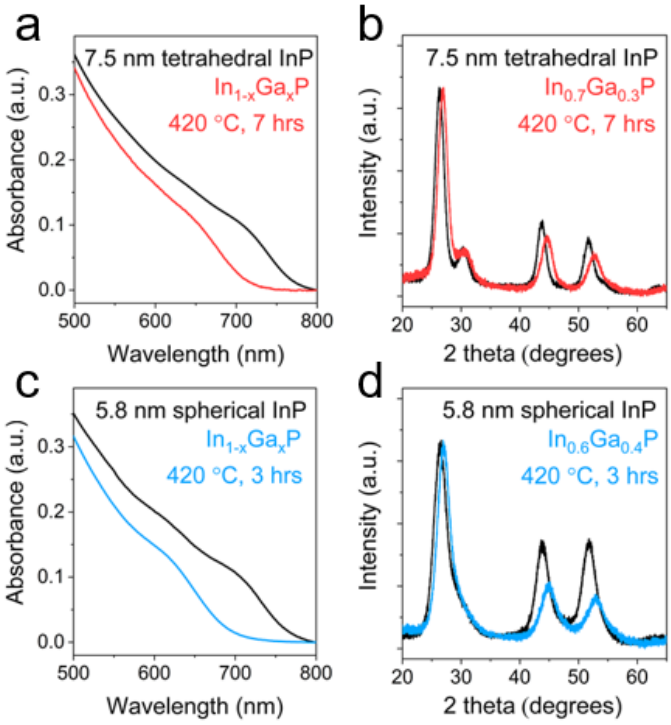

Figure 5.33. Characterization of large InP QDs before and after cation exchange. *(a,c)* Absorbance spectra for solutions of $In_{1-x}Ga_xP$ QDs show a blue shift upon indium-to-gallium cation exchange for *(a)* tetrahedral and *(c)* spherical InP QDs, and *(b,d)* XRD patterns indicate that the lattice constant has decreased upon cation exchange for *(b)* tetrahedral and *(d)* spherical InP QDs.

For the large QDs used in this experiment, higher temperatures and longer times were required to observe significant cation exchange, as compared to the small InP QDs studied above. This agrees with our hypothesis that the cation exchange is diffusion limited, and we must accelerate the diffusion with elevated temperatures to observe significant cation exchange in these QDs with increased volume. Although these conditions were harsher than our standard cation exchange procedure, we observed no evidence of particle decomposition to produce non-colloidal byproducts, which indicates that the thermal stability of $In_{1-x}Ga_xP$ QDs increases with crystallite size.

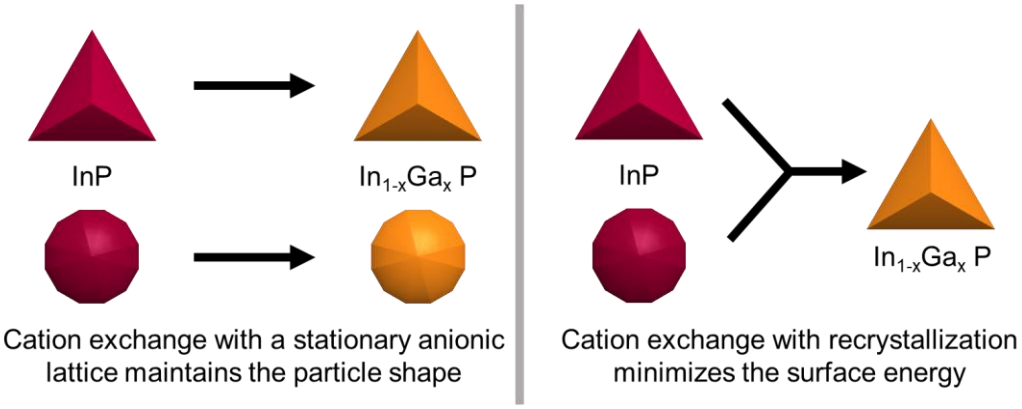

Figure 5.34. Effects of cation exchange on particle shape.
A schematic demonstrates that cation exchange with a stationary anionic lattice leads to maintenance of the nanocrystallite shape, while cation exchange accompanied by surface recrystallization will produce nanocrystallites with the most thermodynamically stable morphology.

The $In_{1-x}Ga_xP$ QD ensembles produced by the indium-to-gallium cation exchange of large tetrahedral and spherical InP QDs are both approximately tetrahedral in morphology. As demonstrated in previous studies, cation exchange in nanocrystallites may proceed without impacting the anionic lattice, maintaining the particle shape, or may disrupt the anionic lattice through recrystallization, resulting in shape change in tandem with cation exchange (Figure 5.34).[70-71] The as-synthesized InP QDs demonstrate distinct morphologies based on the initial synthetic conditions. TEM images of the amine and chloride passivated InP QDs show faceted particles with triangular projections which suggest tetrahedral morphology, while the TOP/TOPO passivated InP QDs show little evidence of particle faceting and near-spherical shapes (Figure 5.32). Following cation exchange, the $In_{1-x}Ga_xP$ QDs produced from both starting materials show faceted, triangular shapes in their TEM images (Figure 5.35). Moreover, the transformation to tetrahedral NCs passivated by (111) surface facets is supported by the prominence of the (111) peak in the XRD patterns following cation exchange (Figure 5.33). These results suggest that under the molten salt cation exchange conditions the QD surface can

recrystallize to form more thermodynamically stable surfaces. The preference for tetrahedral morphology in the molten bromide matrix is supported by calculations which indicate the favorable interactions between halide ions and the InP (111) surface facet.[69] The observed mobility of the phosphide sublattice may explain why we observe cation exchange at relatively low temperatures, where self-diffusion of III^{3+} ions in a III-V lattice should be very slow.[37, 56] Disruption of the phosphide sublattice will dramatically increase the rate of In^{3+} and Ga^{3+} diffusion because the migration of phosphide ions on the NC surface will create lattice defects, which will provide low energy pathways for cation diffusion.

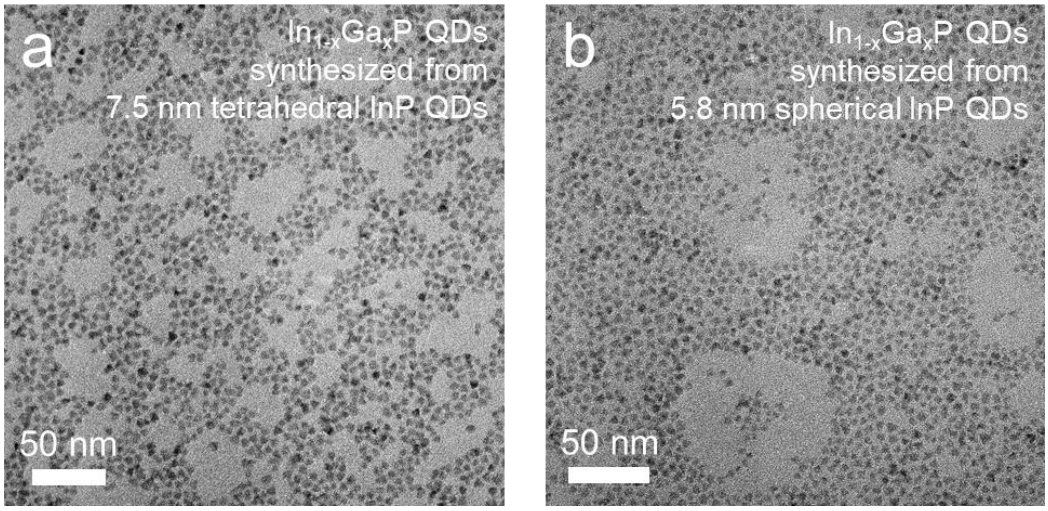

Figure 5.35. TEM images of tetrahedral $In_{1-x}Ga_xP$ QDs from two syntheses.
TEM images show that *(a)* initially tetrahedral InP QDs and *(b)* initially spherical InP QDs have a strongly faceted, near-tetrahedral morphology following indium-to-gallium cation exchange.

5.8. Conclusions.

We have shown that molten salt indium-to-gallium cation exchange is a dynamic system where the reaction can be tuned by changing several variables. The surface chemistry of the initial particles can be optimized to promote strong interactions with the salt matrix, enhancing the colloidal stability, while the chemical composition of the surface can be chosen to stabilize

the NC phase. Time dependent cation exchange experiments have shown that the reactions are kinetically limited under our experimental conditions. Expanding this cation exchange to further extremes of temperature and time may allow for controlled synthesis of new $In_{1-x}Ga_xP$ QD compositions. Cation exchange reactions with large QDs of well-defined shape illustrated the reorganization of the QD surface due to disruption of the anionic lattice. Overall, the InP to $In_{1-x}Ga_xP$ cation exchange results achieved for InP QDs with a variety of initial shapes, sizes, and surface passivations prove the generality of the molten salt indium-to-gallium cation exchange synthetic method. We expect that the insights gained in this work may be used to inform molten salt cation exchange with other III-V QDs (e.g. InAs, InSb), cation exchange with other ions (e.g. Al^{3+}), and new synthetic manipulations of III-V QDs in molten salts (e.g. III-V core-shell synthesis).

5.9. Materials and methods.

All experiments were performed in a nitrogen glovebox with < 2 ppm oxygen and water, unless otherwise noted.

Materials. Hexamethylphosphoramide (HMPA, 99%), trioctylphosphine (TOP, 97%), ammonium sulfide (40-48wt% in water), didodecyldimethylammonium bromide (DDAB, 98%), trioctylphosphine oxide (TOPO, 99%), hydrofluoric acid (HF, 48wt% in water), and anhydrous solvents (hexane, toluene, ethanol (EtOH), isopropanol (IPA), acetonitrile (MeCN), and butanol) were purchased from Sigma Aldrich and used as received. Oleylamine (OAm, technical grade, 70 %) was purchased from Sigma Aldrich and purified before use by freezing, thawing, and then centrifuging to remove any insoluble solids. The resulting purified oleylamine was dried under

vacuum before use. Formamide (FA, 99.5%) and oleic acid (OA, 90%) were purchased from Sigma Aldrich and dried under dynamic vacuum before storage in a nitrogen glove box. Cesium bromide (ultra dry, 99.9%), lithium bromide (ultra dry, 99.9%), potassium bromide (ultra dry, 99.9%), gallium(iii) iodide (ultra dry, 99.999%), gallium(iii) chloride (ultra dry, 99.999%), hexamethylphosphorus triamide ($(NMe_2)_3P$, 97%), and N,N-dimethylformamide (DMF, anhydrous 99.9%) were purchased Alfa Aesar and used as received. Tris(trimethylsilyl) phosphine ($(TMS)_3P$, 98%, stored frozen) and indium(iii) chloride (anhydrous, 99.999%) were purchased from Strem Chemicals and used as received. Lithium selenide was synthesized from lithium triethylborohydride and selenium pellets as described previously.[72-73]

Small InP QDs. Small InP QDs (3.8 nm diameter) were obtained from Nanosys, Inc. as a solution in ODE and were stored in a nitrogen glove box. The QDs were precipitated by addition of EtOH and centrifugation and redispersed in toluene for further processing.

Large, spherical InP QDs. Large, spherical InP QDs were synthesized following the procedure developed by Micic et al.[67] A portion of $InCl_3$ (500 mg, 2.26 mmol) was dissolved in a solution of TOP (7.5 mL) and TOPO (750 mg) at room temperature. This solution was filtered with a 0.2 µm syringe filter to remove undissolved solids and loaded into a 100 mL 3-neck round-bottom flask under nitrogen. A portion of $(TMS)_3P$ (375 mg, 2 mmol) was added to the $InCl_3$ solution, and the reaction was heated at 270 °C for 52 hours. The solution was cooled to room temperature, and the QDs were washed in a nitrogen glove box three times by solvent/nonsolvent (toluene/EtOH) precipitation. As synthesized, these InP QDs are quite polydisperse, but the monodispersity can be significantly improved through size-selective precipitation. Fractions of

successively smaller particles were isolated by slow addition of EtOH and centrifugation. The fraction of the largest particles was used for this work. The QDs were stored as a solution in toluene.

Large, tetrahedral InP QDs. Large, tetrahedral InP QDs were synthesized based on an established procedure.[36, 68] In a 100 mL 3-neck round bottom flask, 442 mg $InCl_3$ (2 mmol) was dissolved in 10 mL oleylamine and degassed at 120 °C for an hour. The solution was heated to 260 °C under nitrogen, and 1.3 mL $(NMe_2)_3P$ (7.1 mmol) was quickly injected. The reaction proceeded at 260 °C for 30 minutes and was then cooled to room temperature naturally. The particles were washed three times by solvent/nonsolvent (toluene/IPA) precipitation. The monodispersity was improved by size-selective precipitation, where EtOH nonsolvent was slowly added to a solution of QDs in toluene and successively smaller particles were isolated by centrifugation. The QDs were stored as a solution in toluene.

$(NH_4)_2S$ ligand exchange. A solution of as-synthesized InP QDs dispersed in toluene (4 mL, 5 mg/mL) was layered atop a solution of 50 µL $(NH_4)_2S$ (40-48wt% aq.) in 2 mL formamide.[33] The mixture was stirred until all QDs transferred to the formamide phase. The toluene phase was removed, and the formamide phase was washed 3 times with 5 mL fresh toluene. The $(NH_4)_2S$-capped QDs were precipitated with MeCN and toluene nonsolvents and centrifugation. The QDs were washed once more with formamide/MeCN/toluene and then the pellet was washed with MeCN/toluene to remove residual formamide. The pellet was allowed to dry overnight under nitrogen at room temperature.

$(DDA)_2S$ ligand exchange. Following the above procedure, a solution of $(NH_4)_2S$-capped InP QDs was prepared in formamide (2 mL, 10 mg/mL). A solution of ~400 mg DDAB in 2 mL toluene was added to the formamide solution and mixed well. The QDs quickly transferred into the toluene phase. The formamide phase was discarded, and the toluene phase was washed with EtOH to remove excess DDAB. The $(DDA)_2S$-capped InP QDs could be redispersed in toluene or hexane.

Li_2Se ligand exchange. A solution of as-synthesized InP QDs dispersed in toluene (10 mL, 2 mg/mL) was layered atop a solution of Li_2Se in formamide (2 mL, 0.1 M).[33] The mixture was stirred until all QDs transferred to the formamide phase. The toluene phase was removed, and the formamide phase was washed 3 times with 10 mL fresh toluene. The Li_2Se-capped QDs were precipitated with MeCN and centrifugation. The QDs were washed with formamide/MeCN/toluene and then the pellet was washed with MeCN to remove residual formamide. The pellet was allowed to dry overnight under nitrogen.

$GaCl_3$ and $InCl_3$ ligand exchanges. The MCl_3 ligand exchanges were adapted from a procedure reported by Dirin *et al*.[34] A solution of as-synthesized InP in hexane (10 mL, 2 mg/mL) was layered atop a solution of MCl_3 in DMF (2 mL, 0.05 M) and stirred until all particles transferred to the DMF phase. The particles were precipitated by addition of toluene and centrifugation and redispersed with DMF plus 10vol% HMPA. This washing procedure was repeated 3 times. The particles were then redispersed with acetonitrile, washed with a mixture of toluene and hexane, and allowed to dry overnight under nitrogen.

Molten salt dispersal. A bromide eutectic mixture was formed by combining CsBr, LiBr, and KBr in the molar ratio 25 : 56.1 : 18.9 (melting point 236 °C) and mixing well with a mortar and pestle. A portion of 1.5 g of the bromide eutectic mixture was combined with the ligand exchanged QDs. For the $(DDA)_2S$ passivated particles, the QDs were added to the salt as a solution in toluene and the toluene was removed by evaporation at 140 °C before further heating. For the other surface ligands, the NCs were added to the salt as a dry powder and were combined in a mortar and pestle. The salt/QD mixture was loaded into a 4 mL glass vial and heated at 300 °C with vigorous stirring (using a glass-coated stir bar) for 1-3 hours to form a homogenous dispersion.

Molten salt 400 °C anneal. After dispersal of the QDs in molten bromide eutectic at 300 °C, the mixture was cooled to room temperature and transferred into a muffle furnace. The QD/salt dispersion was heated at 400 °C for 1 hour.

Gallium cation exchange. After dispersal of the QDs in molten bromide eutectic at 300 °C, the mixture was cooled to room temperature and 230 mg GaI_3 (0.5 mmol) was added to the salt mixture. The mixture was heated at 300 °C with vigorous stirring for an additional hour to fully incorporate the gallium salt. After cooling to room temperature, the salt mixture was transferred into the muffle furnace and heated at elevated temperature (380-430 °C) for the desired reaction time (1-16 hours). Higher temperatures and longer reaction times led to increased gallium incorporation.

QD recovery following molten salt treatment. The bromide salt matrix was dissolved in 80 °C formamide (~10 mL), and the QDs were recovered as a solid by centrifugation. The QD solid was washed with 4 mL fresh formamide to remove residual salt. The particles could regain colloidal stability in nonpolar solvents through treatment with either oleic acid /oleylamine (OA/OAm) or $(NH_4)_2S$ and DDAB (S/DDA). To recover the particles with OA/OAm, the QD powder was combined with 2 mL toluene, 100 µL oleic acid, and 100 µL oleylamine and stirred at 50 °C for 45 minutes. The resulting QD solution in toluene was washed with ethanol to remove excess ligands and then stored in toluene or hexane. For S/DDA recovery, the QD powder was dispersed in 2 mL formamide using 30 µL $(NH_4)_2S$ solution. A solution of DDAB in toluene was then layered atop the formamide solution, and the QDs transferred to the toluene phase upon mixing. The QD solution in toluene was washed with ethanol to remove excess ligands, and the particles were redispersed in toluene or hexane.

HF treatment of $In_{1-x}Ga_xP$ QDs. A solution of 3 mL hexane, 1 mL butanol, 2 µL 5vol% HF in butanol (2.4×10^{-6} mol HF), 50 µL $In_{1-x}Ga_xP$ QD solution in hexane (10 mg/mL, ~8×10^{-9} mol QDs), and ~400 mg TOPO was prepared in a plastic centrifuge tube and sealed under nitrogen in the glove box. In a fume hood, the solution was illuminated by a halogen lamp with a 515 nm long pass filter for 2 hours. Absorbance, PL, and PLE spectra of the HF-treated solutions were collected in PMMA cuvettes in air. *Note:* Higher emission quantum yield was achieved with 10x more concentrated HF treatment, accompanied by an absorbance blue shift and PL broadening.

Characterization:

*Optical absorption***.** UV-vis spectra were collected on colloidal solutions of QDs with a Cary 5000 spectrophotometer.

Emission. Photoluminescence (PL) and photoluminescence excitation (PLE) spectra for colloidal solutions of QDs were collected using a Horiba Fluoromax-4 fluorimeter. Unless otherwise stated, PL spectra were acquired with a 430 nm excitation. For both the PL and PLE measurements, the monochromator slits were set at 3 nm at both the entrance and exit slits. The PLE spectra have excitation scatter removed for clarity. Quantum yields (QY) were measured by comparison to the reference dye Coumarin-153 (QY 53%).

Powder x-ray diffraction. Wide-angle powder x-ray diffraction (PXRD) data was acquired on a Bruker D8 diffractometer using a 1.54 Å Cu K-α source and a Vantec 2000 array detector. QD samples were prepared as films on glass or silicon. The $In_{1-x}Ga_xP$ composition was estimated from the position of the (111) peak using Vegard's law. The lattice constant, *a,* is related to the (111) peak position as follows, where d_{111} is the d-spacing of the (111) plane, λ is the wavelength of the x-ray source, and θ is the peak position:

$$d_{111} = \frac{\lambda}{2\sin\theta} \quad \text{and} \quad a = d_{111}\sqrt{3}$$

Then, the lattice constants of bulk InP (5.8687 Å) and GaP (5.4505 Å) can be used as follows to calculate the alloy composition, *x*:

$$a(In_{1-x}Ga_xP) = (1-x)a_{In} + xa_{Ga}$$

Small-angle x-ray scattering (SAXS). Colloidal solutions of QDs in toluene or hexane were prepared in sealed Kapton capillaries for small-angle x-ray scattering (SAXS) experiments. SAXS patterns were collected using a SAXSLab Ganesha instrument with Cu Kα radiation (λ = 1.54 Å). The SAXS curves were analyzed by fitting to a quantitative model in Igor Pro using the Irena package (available at http://usaxs.xray.aps.anl.gov/staff/ilavsky/irena.html).[74] The scattering curves were fit in the particle size distribution module using the model-free Maximum Entropy approach. Based on TEM data, the particles' form factor was assumed to be that of a sphere with an aspect ratio of 1. The extracted size distributions were further fit with symmetric Gaussians.

Transmission electron microscopy (TEM). TEM images were obtained on an FEI Technai F30 microscope at an accelerating voltage of 300 kV.

Inductively-coupled plasma optical emission spectroscopy (ICP-OES). QD samples were prepared for ICP-OES measurements by thorough washing with ethanol followed by digestion in 0.5 mL of 4:1 HCl (≥37%, TraceSELECT, Fluka) : HNO_3 (69.0%, TraceSELECT, Aldrich). The samples were diluted with deionized ultra-filtered water to a concentration of 0.5-25 ppm. ICP-OES analysis was performed using an Agilent 700 Series spectrometer.

5.10. Chapter 5 bibliography.

1. Coe-Sullivan, S.; Liu, W.; Allen, P.; S. Steckel, J., Quantum Dots for LED Downconversion in Display Applications. *ECS J. Solid State Sci. Technol.* **2013,** *2*, R3026-R3030.

2. Chen, H.; He, J.; Wu, S., Recent Advances on Quantum-Dot-Enhanced Liquid-Crystal Displays. *IEEE Journal of Selected Topics in Quantum Electronics* **2017,** *23*, 1-11.

3. Zhou, J.; Pu, C.; Jiao, T.; Hou, X.; Peng, X., A Two-Step Synthetic Strategy toward Monodisperse Colloidal CdSe and CdSe/CdS Core/Shell Nanocrystals. *J. Am. Chem. Soc.* **2016,** *138*, 6475-6483.

4. Chen, O.; Zhao, J.; Chauhan, V. P.; Cui, J.; Wong, C.; Harris, D. K.; Wei, H.; Han, H.-S.; Fukumura, D.; Jain, R. K.; Bawendi, M. G., Compact high-quality CdSe–CdS core–shell nanocrystals with narrow emission linewidths and suppressed blinking. *Nat. Mater.* **2013,** *12*, 445.

5. Horn, D. A. In *EU RoHS Recast — New requirements and impacts for the Information and Communications Technology industry*, 2012 IEEE International Symposium on Sustainable Systems and Technology (ISSST), 16-18 May 2012; 2012; pp 1-5.

6. Das, A.; Snee, P. T., Synthetic Developments of Nontoxic Quantum Dots. *ChemPhysChem* **2016,** *17*, 598-617.

7. Park, J. P.; Lee, J.-J.; Kim, S.-W., Highly luminescent InP/GaP/ZnS QDs emitting in the entire color range via a heating up process. *Scientific Reports* **2016,** *6*, 30094.

8. Xie, R.; Battaglia, D.; Peng, X., Colloidal InP Nanocrystals as Efficient Emitters Covering Blue to Near-Infrared. *J. Am. Chem. Soc.* **2007,** *129*, 15432-15433.

9. Li, Y.; Hou, X.; Dai, X.; Yao, Z.; Lv, L.; Jin, Y.; Peng, X., Stoichiometry-Controlled InP-Based Quantum Dots: Synthesis, Photoluminescence, and Electroluminescence. *J. Am. Chem. Soc.* **2019,** *141*, 6448-6452.

10. Kim, Y.; Ham, S.; Jang, H.; Min, J. H.; Chung, H.; Lee, J.; Kim, D.; Jang, E., Bright and Uniform Green Light Emitting InP/ZnSe/ZnS Quantum Dots for Wide Color Gamut Displays. *ACS Applied Nano Materials* **2019,** *2*, 1496-1504.

11. Allen, P. M.; Walker, B. J.; Bawendi, M. G., Mechanistic Insights into the Formation of InP Quantum Dots. *Angew. Chem., Int. Ed.* **2010,** *49*, 760-762.

12. Gary, D. C.; Glassy, B. A.; Cossairt, B. M., Investigation of Indium Phosphide Quantum Dot Nucleation and Growth Utilizing Triarylsilylphosphine Precursors. *Chem. Mater.* **2014,** *26*, 1734-1744.

13. Stein, J. L.; Holden, W. M.; Venkatesh, A.; Mundy, M. E.; Rossini, A. J.; Seidler, G. T.; Cossairt, B. M., Probing Surface Defects of InP Quantum Dots Using Phosphorus Kα and Kβ X-ray Emission Spectroscopy. *Chem. Mater.* **2018,** *30*, 6377-6388.

14. Tessier, M. D.; Baquero, E. A.; Dupont, D.; Grigel, V.; Bladt, E.; Bals, S.; Coppel, Y.; Hens, Z.; Nayral, C.; Delpech, F., Interfacial Oxidation and Photoluminescence of InP-Based Core/Shell Quantum Dots. *Chem. Mater.* **2018,** *30*, 6877-6883.

15. Ramasamy, P.; Kim, N.; Kang, Y.-S.; Ramirez, O.; Lee, J.-S., Tunable, Bright, and Narrow-Band Luminescence from Colloidal Indium Phosphide Quantum Dots. *Chem. Mater.* **2017,** *29*, 6893-6899.

16. Ramasamy, P.; Ko, K.-J.; Kang, J.-W.; Lee, J.-S., Two-Step "Seed-Mediated" Synthetic Approach to Colloidal Indium Phosphide Quantum Dots with High-Purity Photo- and Electroluminescence. *Chem. Mater.* **2018,** *30*, 3643-3647.

17. Janke, E. M.; Williams, N. E.; She, C.; Zherebetskyy, D.; Hudson, M. H.; Wang, L.; Gosztola, D. J.; Schaller, R. D.; Lee, B.; Sun, C.; Engel, G. S.; Talapin, D. V., Origin of Broad Emission Spectra in InP Quantum Dots: Contributions from Structural and Electronic Disorder. *J. Am. Chem. Soc.* **2018,** *140*, 15791-15803.

18. Fox, M.; Ispasoiu, R., Quantum Wells, Superlattices, and Band-Gap Engineering. 2007; pp 1021-1040.

19. Kim, S.; Kim, T.; Kang, M.; Kwak, S. K.; Yoo, T. W.; Park, L. S.; Yang, I.; Hwang, S.; Lee, J. E.; Kim, S. K.; Kim, S.-W., Highly Luminescent InP/GaP/ZnS Nanocrystals and Their Application to White Light-Emitting Diodes. *J. Am. Chem. Soc.* **2012,** *134*, 3804-3809.

20. Pietra, F.; Kirkwood, N.; De Trizio, L.; Hoekstra, A. W.; Kleibergen, L.; Renaud, N.; Koole, R.; Baesjou, P.; Manna, L.; Houtepen, A. J., Ga for Zn Cation Exchange Allows for Highly Luminescent and Photostable InZnP-Based Quantum Dots. *Chem. Mater.* **2017,** *29*, 5192-5199.

21. Srivastava, V.; Liu, W.; Janke, E. M.; Kamysbayev, V.; Filatov, A. S.; Sun, C.-J.; Lee, B.; Rajh, T.; Schaller, R. D.; Talapin, D. V., Understanding and Curing Structural Defects in Colloidal GaAs Nanocrystals. *Nano Lett.* **2017,** *17*, 2094-2101.

22. Srivastava, V.; Kamysbayev, V.; Hong, L.; Dunietz, E.; Klie, R. F.; Talapin, D. V., Colloidal Chemistry in Molten Salts: Synthesis of Luminescent In1–xGaxP and In1–xGaxAs Quantum Dots. *J. Am. Chem. Soc.* **2018,** *140*, 12144-12151.

23. Zhang, H.; Dasbiswas, K.; Ludwig, N. B.; Han, G.; Lee, B.; Vaikuntanathan, S.; Talapin, D. V., Stable colloids in molten inorganic salts. *Nature* **2017,** *542*, 328-331.

24. Kamysbayev, V.; Srivastava, V.; Ludwig, N. B.; Borkiewicz, O. J.; Zhang, H.; Ilavsky, J.; Lee, B.; Chapman, K. W.; Vaikuntanathan, S.; Talapin, D. V., Nanocrystals in Molten Salts and Ionic Liquids: Experimental Observation of Ionic Correlations Extending beyond the Debye Length. *ACS Nano* **2019,** *13*, 5760-5770.

25. Dash, A.; Vaßen, R.; Guillon, O.; Gonzalez-Julian, J., Molten salt shielded synthesis of oxidation prone materials in air. *Nat. Mater.* **2019,** *18*, 465-470.

26. Fedorov, V. A.; Ganshin, V. A.; Korkishko, Y. N., Ion exchange in II–VI crystals: Thermodynamics, kinetics, and technology. *physica status solidi (a)* **1993,** *139*, 9-65.

27. Sundararaman, C. S.; Poulin, S.; Currie, J. F.; Leonelli, R., The sulfur-passivated InP surface. *Canadian Journal of Physics* **1991,** *69*, 329-332.

28. Anderson, G. W.; Hanf, M. C.; Norton, P. R.; Lu, Z. H.; Graham, M. J., Thermal stability of sulfur passivated InP(100)-(1×1). *Appl. Phys. Lett.* **1994,** *65*, 171-173.

29. Gallet, D.; Hollinger, G., Chemical, structural, and electronic properties of sulfur-passivated InP(001) (2×1) surfaces treated with (NH4)2Sx. *Appl. Phys. Lett.* **1993,** *62*, 982-984.

30. Rosen, E. L.; Buonsanti, R.; Llordes, A.; Sawvel, A. M.; Milliron, D. J.; Helms, B. A., Exceptionally Mild Reactive Stripping of Native Ligands from Nanocrystal Surfaces by Using Meerwein's Salt. *Angew. Chem., Int. Ed.* **2012,** *51*, 684-689.

31. Kovalenko, M. V.; Scheele, M.; Talapin, D. V., Colloidal Nanocrystals with Molecular Metal Chalcogenide Surface Ligands. *Science* **2009,** *324*, 1417-1420.

32. Zhang, H.; Jang, J.; Liu, W.; Talapin, D. V., Colloidal Nanocrystals with Inorganic Halide, Pseudohalide, and Halometallate Ligands. *ACS Nano* **2014,** *8*, 7359-7369.

33. Nag, A.; Kovalenko, M. V.; Lee, J.-S.; Liu, W.; Spokoyny, B.; Talapin, D. V., Metal-free Inorganic Ligands for Colloidal Nanocrystals: S2–, HS–, Se2–, HSe–, Te2–, HTe–, TeS32–, OH–, and NH2– as Surface Ligands. *J. Am. Chem. Soc.* **2011,** *133*, 10612-10620.

34. Dirin, D. N.; Dreyfuss, S.; Bodnarchuk, M. I.; Nedelcu, G.; Papagiorgis, P.; Itskos, G.; Kovalenko, M. V., Lead Halide Perovskites and Other Metal Halide Complexes As Inorganic Capping Ligands for Colloidal Nanocrystals. *J. Am. Chem. Soc.* **2014,** *136*, 6550-6553.

35. V. N. Bessolov, M. V. L., Chalcogenide passivation of III–V semiconductor surfaces. *Semiconductors+* **1998,** *32*, 1141-1156.

36. Tessier, M. D.; Dupont, D.; De Nolf, K.; De Roo, J.; Hens, Z., Economic and Size-Tunable Synthesis of InP/ZnE (E = S, Se) Colloidal Quantum Dots. *Chem. Mater.* **2015,** *27*, 4893-4898.

37. Fisher, D. J., *Diffusion in Semiconductors, Other Than Silicon: Compilation*. Trans Tech: 2010.

38. Scalise, E.; Srivastava, V.; Janke, E.; Talapin, D.; Galli, G.; Wippermann, S., Surface chemistry and buried interfaces in all-inorganic nanocrystalline solids. *Nat. Nanotech.* **2018,** *13*, 841-848.

39. Orman, J. A. V.; Grove, T. L.; Shimizu, N., Rare earth element diffusion in diopside: influence of temperature, pressure, and ionic radius, and an elastic model for diffusion in silicates. *Contributions to Mineralogy and Petrology* **2001,** *141*, 687-703.

40. Kovalenko, M. V.; Bodnarchuk, M. I.; Talapin, D. V., Nanocrystal Superlattices with Thermally Degradable Hybrid Inorganic−Organic Capping Ligands. *J. Am. Chem. Soc.* **2010,** *132*, 15124-15126.

41. Tsui, E. Y.; Hartstein, K. H.; Gamelin, D. R., Selenium Redox Reactivity on Colloidal CdSe Quantum Dot Surfaces. *J. Am. Chem. Soc.* **2016,** *138*, 11105-11108.

42. Kim, T.-G.; Zherebetskyy, D.; Bekenstein, Y.; Oh, M. H.; Wang, L.-W.; Jang, E.; Alivisatos, A. P., Trap Passivation in Indium-Based Quantum Dots through Surface Fluorination: Mechanism and Applications. *ACS Nano* **2018,** *12*, 11529-11540.

43. Liu, W.; Lee, J.-S.; Talapin, D. V., III–V Nanocrystals Capped with Molecular Metal Chalcogenide Ligands: High Electron Mobility and Ambipolar Photoresponse. *J. Am. Chem. Soc.* **2013,** *135*, 1349-1357.

44. Jang, J.; Liu, W.; Son, J. S.; Talapin, D. V., Temperature-Dependent Hall and Field-Effect Mobility in Strongly Coupled All-Inorganic Nanocrystal Arrays. *Nano Lett.* **2014,** *14*, 653-662.

45. Tmar, M.; Gabriel, A.; Chatillon, C.; Ansara, I., Critical analysis and optimization of the thermodynamic properties and phase diagrams in the III-V compounds: The In-P and Ga-P systems. *Journal of Crystal Growth* **1984,** *68*, 557-580.

46. Riesz, F.; Dobos, L.; Vignali, C.; Pelosi, C., Thermal decomposition of InP surfaces: volatile component loss, morphological changes, and pattern formation. *Materials Science and Engineering: B* **2001,** *80*, 54-59.

47. Tsang, W. T., *Semiconductors and Semimetals*. Elsevier Science: 1985.

48. Borisenko, V. E.; Hesketh, P. J., *Rapid Thermal Processing of Semiconductors*. Springer US: 2013.

49. Everett, D. H., Manual of Symbols and Terminology for Physicochemical Quantities and Units, Appendix II: Definitions, Terminology and Symbols in Colloid and Surface Chemistry. In *Pure and Applied Chemistry*, 1972; Vol. 31, p 577.

50. Chen, K. Y.; Morris, J. C., Kinetics of oxidation of aqueous sulfide by oxygen. *Environmental Science & Technology* **1972,** *6*, 529-537.

51. Foyt, A. G., The electro-optic applications of InP. *Journal of Crystal Growth* **1981,** *54*, 1-8.

52. Li, T.; Senesi, A. J.; Lee, B., Small Angle X-ray Scattering for Nanoparticle Research. *Chem. Rev.* **2016,** *116*, 11128-11180.

53. Jana, S.; de Frutos, M.; Davidson, P.; Abécassis, B., Ligand-induced twisting of nanoplatelets and their self-assembly into chiral ribbons. *Science Advances* **2017,** *3*, e1701483.

54. Zhou, Y.; Wang, F.; Buhro, W. E., Large Exciton Energy Shifts by Reversible Surface Exchange in 2D II–VI Nanocrystals. *J. Am. Chem. Soc.* **2015,** *137*, 15198-15208.

55. Meulenberg, R. W.; Jennings, T.; Strouse, G. F., Compressive and tensile stress in colloidal CdSe semiconductor quantum dots. *Phys. Rev. B* **2004,** *70*, 235311.

56. Goldstein, B., Diffusion in Compound Semiconductors. *Phys. Rev.* **1961,** *121*, 1305-1311.

57. Nelson, A.; Honrao, S.; Hennig, R. G.; Robinson, R. D., Nanocrystal Symmetry Breaking and Accelerated Solid-State Diffusion in the Lead–Cadmium Sulfide Cation Exchange system. *Chem. Mater.* **2019,** *31*, 991-1005.

58. Ovid'ko, I. A., Deformation and Diffusion Modes in Nanocrystalline Materials. *International Materials Reviews* **2005,** *50*, 65-82.

59. Bublik, V. T.; Leikin, V. N., Calculation of the pseudobinary alloy semiconductor phase diagrams. *physica status solidi (a)* **1978,** *46*, 365-372.

60. Mićić, O. I.; Sprague, J.; Lu, Z.; Nozik, A. J., Highly efficient band-edge emission from InP quantum dots. *Appl. Phys. Lett.* **1996,** *68*, 3150-3152.

61. Talapin, D. V.; Gaponik, N.; Borchert, H.; Rogach, A. L.; Haase, M.; Weller, H., Etching of Colloidal InP Nanocrystals with Fluorides: Photochemical Nature of the Process Resulting in High Photoluminescence Efficiency. *J. Phys. Chem. B* **2002,** *106*, 12659-12663.

62. Houtepen, A. J.; Hens, Z.; Owen, J. S.; Infante, I., On the Origin of Surface Traps in Colloidal II–VI Semiconductor Nanocrystals. *Chem. Mater.* **2017,** *29*, 752-761.

63. Busby, E.; Anderson, N. C.; Owen, J. S.; Sfeir, M. Y., Effect of Surface Stoichiometry on Blinking and Hole Trapping Dynamics in CdSe Nanocrystals. *J. Phys. Chem. C* **2015,** *119*, 27797-27803.

64. Ban, H. W.; Oh, J. G.; Jo, S.; Jeong, H.; Gu, D. H.; Baek, S.; Lee, S. Y.; Park, Y. I.; Jang, J.; Son, J. S., Polyphosphide Precursor for Low-Temperature Solution-Processed Fibrous Phosphorus Thin Films. *Chem. Mater.* **2019,** *31*, 5909-5918.

65. Clearfield, A., Role of ion exchange in solid-state chemistry. *Chem. Rev.* **1988,** *88*, 125-148.

66. Schlesinger, M. E., The Thermodynamic Properties of Phosphorus and Solid Binary Phosphides. *Chem. Rev.* **2002,** *102*, 4267-4302.

67. Micic, O. I.; Curtis, C. J.; Jones, K. M.; Sprague, J. R.; Nozik, A. J., Synthesis and Characterization of InP Quantum Dots. *J. Phys. Chem.* **1994,** *98*, 4966-4969.

68. Song, W.-S.; Lee, H.-S.; Chul Lee, J.; Seon Jang, D.; Choi, Y.; Choi, M.; Yang, H., Amine-derived synthetic approach to color-tunable InP/ZnS quantum dots with high fluorescent qualities. *Journal of Nanoparticle Research* **2013,** *15*, 1750.

69. Kim, K.; Yoo, D.; Choi, H.; Tamang, S.; Ko, J.-H.; Kim, S.; Kim, Y.-H.; Jeong, S., Halide–Amine Co-Passivated Indium Phosphide Colloidal Quantum Dots in Tetrahedral Shape. *Angew. Chem., Int. Ed.* **2016,** *55*, 3714-3718.

70. Beberwyck, B. J.; Surendranath, Y.; Alivisatos, A. P., Cation Exchange: A Versatile Tool for Nanomaterials Synthesis. *J. Phys. Chem. C* **2013,** *117*, 19759-19770.

71. Son, D. H.; Hughes, S. M.; Yin, Y.; Paul Alivisatos, A., Cation Exchange Reactions in Ionic Nanocrystals. *Science* **2004,** *306*, 1009.

72. Beecher, A. N.; Yang, X.; Palmer, J. H.; LaGrassa, A. L.; Juhas, P.; Billinge, S. J. L.; Owen, J. S., Atomic Structures and Gram Scale Synthesis of Three Tetrahedral Quantum Dots. *J. Am. Chem. Soc.* **2014,** *136*, 10645-10653.

73. Hazarika, A.; Fedin, I.; Hong, L.; Guo, J.; Srivastava, V.; Cho, W.; Coropceanu, I.; Portner, J.; Diroll, B. T.; Philbin, J. P.; Rabani, E.; Klie, R.; Talapin, D. V., Colloidal Atomic Layer Deposition with Stationary Reactant Phases Enables Precise Synthesis of "Digital" II–VI Nano-heterostructures with Exquisite Control of Confinement and Strain. *J. Am. Chem. Soc.* **2019,** *141*, 13487-13496.

74. Ilavsky, J.; Jemian, P. R., Irena: tool suite for modeling and analysis of small-angle scattering. *Journal of Applied Crystallography* **2009,** *42*, 347-353.